Synthesis of Hybrid $(III\text{-}V)_y(IV)_{5\text{-}2y}$ Semiconductors: A New Approach to Extending the Optoelectronic Capabilities of Si and Ge Technologies

by

Patrick Edward Sims

A Dissertation Presented in Partial Fulfillment
of the Requirements for the Degree
Doctor of Philosophy

Approved April 2017 by the
Graduate Supervisory Committee:

John Kouvetakis, Chair
Andrew Chizmeshya
José Menéndez

ARIZONA STATE UNIVERSITY

May 2017

ABSTRACT

Modern semiconductor technologies have been dominated by group-IV materials and III-V analogues. The development of hybrid derivatives combining appropriate members of these systems has been of interest for the purpose of extending the optoelectronic capabilities of the state-of-the-art. Early work on pseudo-binary (III-V)-IV alloys, described with the general formula $(\text{III-V})_{1\text{-x}}(\text{IV}_2)_\text{x}$, showed limited progress due to phase segregation, auto-doping and compositional inhomogeneities. Recently, new techniques were introduced for synthesizing new classes of (III-V)-IV hybrid materials using reactions of $\text{V(IVH}_3)_3$ molecules [V = N, P, As and IV = Si, Ge] with group-III elements (B, Al, Ga, In). The reactions produce (III-V)-IV_3 building blocks that interlink to form diamond-like frameworks in which the III-V pairs incorporate as isolated units within the group-IV lattice. This approach not only precludes phase segregation, but also provides access to structures and compositions unattainable by conventional means. Entire new families of crystalline (III-V)-IV_3 and $(\text{III-V})_\text{y}(\text{IV})_{5\text{-y}}$ alloys with tunable IV-rich compositions, different from conventional $(\text{III-V})_{1\text{-x}}(\text{IV}_2)_\text{x}$ systems, have been grown on Si(100) and GaP(100) wafers as well as $\text{Si}_{1\text{-x}}\text{Ge}_\text{x}$ and Ge buffer layers which, in most cases, provide lattice matched templates for Si integration.

In this work, materials in the In-P-Ge, Ga-As-Ge and Ga-P-Si systems that would exhibit direct-gap behavior were targeted. A series of $(\text{InP})_\text{y}\text{Ge}_{5\text{-2y}}$ alloys with tunable Ge contents above 60% were synthesized by reactions of $\text{P(GeH}_3)_3$ and indium atoms and were studied for bonding, structure, and optical response. $(\text{GaAs})_\text{y}\text{Ge}_{5\text{-2y}}$ analogues were also grown and exhibited strong photoluminescence for applications in mid-IR photonics. The GaPSi_3 alloy and Si-rich derivatives were produced via reactions of $\text{P(SiH}_3)_3$ and $[\text{H}_2\text{GaNMe}_2]_2$ and exhibit enhanced absorption in the visible range. Quaternary analogues in the $Al_{1-x}B_xPSi_3$ system were grown on Si via reactions of $Al(BH_4)_3$ and $P(SiH_3)_3$ leading to the formation crystalline materials with extended absorption relative to Si. This makes them imminently suitable for applications in Si-based photovoltaics. The work emphasized use of quantum-chemical simulations to elucidate structural, thermodynamic, and mechanical properties of the synthesized systems. The theory also included simulations of new synthetic targets such as BNC_3, $BNSi_3$, BPC_3, and $BPSi_3$ with interesting mechanical properties and strong covalent bonding.

To my family: Mom, Dad, Tío, Tía, everyone.

TABLE OF CONTENTS

LIST OF TABLES

LIST OF FIGURES

Figure Page

Chapter 1

INTRODUCTION, BACKGROUND, AND MOTIVATION FOR THE PURSUIT OF HYBRID (III-V)-$(IV)_3$ SEMICONDUCTOR ALLOYS

1.1 Introduction

Semiconductors are some of the most technologically important materials in our world. We lead technocentric lives where we are constantly vying to have the latest and greatest gadgets. All of these devices are teeming with semiconducting materials, our computers, televisions, iPhones, tablets, and the infrastructure supporting the internet just to name a few. As we become more reliant on the technology available to us, the semiconductor industry has been driven by our desire to have electronics that are faster, smaller, and more efficient. All of these advances, in terms of anthropogenic development of materials, have happened in the blink of an eye; for reference the transition from using copper to bronze tools took nearly 1000 years. The first semiconducting device, a transistor, was demonstrated in 1947, a mere 70 years ago. In addition to the integrated circuits, microprocessors, and light emitting diodes that are commonly considered, semiconductors are also emerging as a viable renewable energy source. Photovoltaics are semiconductor devices capable of converting sunlight into electricity, providing a clean and increasingly efficient alternative to traditional fuel sources.

However, our fascination with newer and better electronics has grown exponentially and we are now at a point where this desire out-paces researchers' ability to keep up. The majority of current technology is primarily based on a small subset of materials:

Si, Ge, SiGe alloys, and compound semiconductors such as III-V materials and their alloys. As we near the limits of what can be done with the current suite of materials a paradigm shift is needed to continue advancing both technologically and academically; this can come in the form of a new class of materials which can be easily integrated into current infrastructure, but offer optoelectronic capabilities that extend beyond what is currently available. Semiconductors are a broad class of materials that have very interesting properties; the prospects are seemingly infinite.

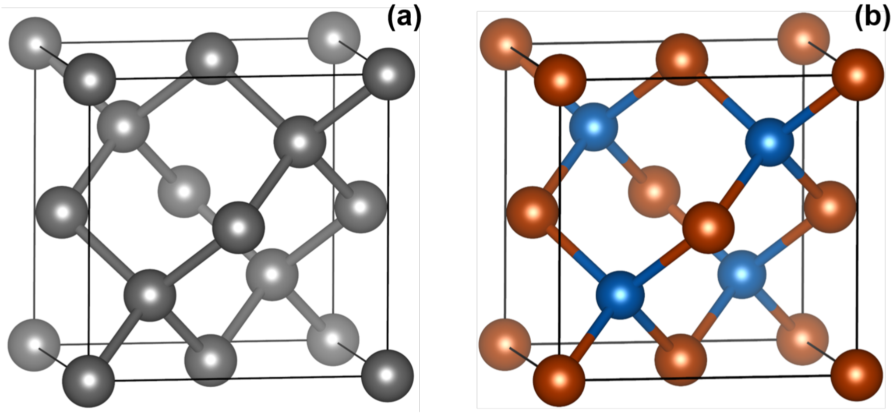

Figure 1: (a) The conventional 8-atom unit cell of a diamond-like material. (b) The conventional unit cell of a zincblende like structure showing the packing arrangement of the two distinct atom types.

This dissertation will explore on one such class of materials, alloys between group-IV and III-V compound semiconductors. As shown in Figure 1 both group-IV and III-V compound semiconductors have tetrahedral structures; in each case every atom is surrounded by four others forming a regular tetrahedron. Group-IV semiconductors crystallize in the diamond-type structure where all atoms are the same. In the case of III-V semiconductors the nearest neighbor atoms forming the regular tetrahedron are unlike the central atom, this arrangement is the zincblende structure type.

The studies presented herein will focus on the growth and characterization of this enigmatic group of materials. These materials offer an extension of the optoelectronic capabilities of the parent types, group-IV and III-V materials, and can be easily integrated on existing platforms, such as Si and Ge-buffered Si substrates. Within this class of materials the ones that are comprised of end-members having similar lattice parameters are particularly interesting and important, the group-IV diamond-like and III-V zincblende materials have distinct electronic properties, effectively decoupling bandgap and lattice dimension. This subclass contains alloys which allow for the tuning of the bandgap at a fixed lattice parameter.

This dissertation contains six chapters which describe, in detail, the synthesis, characterization, and materials properties of new alloys and compounds in the In-P-Ge, Al-B-P-Si, Ga-P-Si, and Ga-As-Ge systems. The synthesis of these alloy systems was achieved through directed chemical reactions. These reactions promote the formation of III-V-IV$_3$ building-blocks. The building-blocks are tetrahedral, mimicking the common motif found in both group-IV and III-V compound semiconductors. Through interlinking of the tetrahedral units an extended solid with a diamond-like structure is formed. The first chapter of this dissertation will provide the impetus for the exploration of hybrid semiconductor alloys and provide context for the explorations described in the subsequent chapters.

1.2 Elemental Semiconductors: The Rise of Germanium and Silicon

Semiconductors are a class of materials which have electrical resistivities that are between that of metals and insulators, in addition to having a negative temperature coefficient of resistivity. These two properties are more closely intertwined than it would seem at first glance, but are the basis for why semiconductors behave the way they do. To understand these ideas we must take a look at the electronic structure of a semiconducting material. This is deeply rooted in the work of Bloch who described the properties of electrons in a periodic potential; a tangible example of such a potential are the nuclei in a crystalline solid. The solutions to the Schrödinger equation found by Bloch show the eigenvalues are continuous and dependent on the reciprocal lattice wave vector, or k-vector, thus creating energy bands.[1] This idea of electronic band structure has allowed us to understand the nature of semiconductor behavior. In the band structure of a semiconductor there exists an energy regime between the occupied (valence) bands and the empty (conduction) bands at zero temperature, this region devoid of states is the so-called bandgap. The size of this bandgap, in part, determines the difference between a semiconductor and an insulator, whereas a conductor has no gap. At zero temperature there are no electrons in the conduction band to facilitate propagation, meaning the material is a perfect insulator; however, at finite temperatures thermal energy is capable of exciting electrons from the valence bands into conduction bands, resulting in a decrease in electrical resistivity. We are also able to control the resistivity of a semiconducting material through the use of impurity atoms, a process called doping. There are two types of doping: n-type, or negative and p-type, or positive doping; the former is done through the introduction of an impurity which donates electrons to the parent material leading to additional electrons in the conduction band, the latter introduces electron deficiencies which create holes, or vacancies, in the valence band. Our ability to tune the electrical resistivity makes semiconductors one of the most tunable and versatile classes of materials known.

The group-IV elemental semiconductors Si and Ge were among the first considered due to their relative simplicity. Germanium was far from being the first semiconductor studied, but it might be the most important.[2] When germanium was first discovered it was described as a weakly conducting metal, and progress from that point was slow.[3] Germanium, and semiconductors in general, were hard to purify to a sufficient level for meaningful progress in the field. Early purification techniques typically involved melting the material to remove impurities and in the end it was the lower melting point of Ge, compared to Si, that helped it become the material of choice for early adopters. The first major milestone was reached in the early 1940s when pure enough Ge was obtained at Purdue. This was the tipping point for the modern semiconducting era. The lab at Purdue provided a sample of the high-purity Ge to Bell labs; Bardeen and Brattain used this sample to produce the first solid state transistor in 1947.[4]

The invention of the Ge transistor marked the beginning of its short-lived heyday as the king of semiconductors. As the required technologies were developed to pursue Ge devices, the arms race that developed between materials science laboratories, both academic and industrial, resolved many of the issues hindering the development of Si devices. As processing techniques matured and protocols were developed to manufacture high purity single crystal Ge, the Si analogues were ported and the technology gap between the two materials began to close. Just as Ge was gaining traction as the material of choice for semiconducting devices, Tanenbaum, a researcher at Bell Labs, created the first working Si transistor in 1954.[5] The race had officially begun: in 1958, Kilby at Texas Instruments demonstrated the first integrated circuit using Ge technology, and not even six months later, Noyce, at Fairchild Semiconductor, demonstrated an improved design based on Si.[6,7]

Silicon with its higher bandgap, and extremely stable oxide, SiO_2, contributed greatly to its rise to power as the preferred semiconductor. The more agreeable properties of Si made it a perfect candidate for a manufacturing method known as planar processing, leading to the development of planar integrated circuits at Fairchild Semiconductor. Little did the world know, this was the first data point in the now infamous Moore's law, which projected that the number of components per integrated circuit would double every twelve months. We have followed this trend very closely, and 70 years later are fast approaching the physical limits of Si technologies: current state-of-the-art microprocessors contain in excess of one billion transistors as small as 10 nm, and consumer processors are not far behind at 14 nm.

1.3 III-V Compound Semiconductors

The covalent semiconductors, Ge and Si, are not the only semiconductors that have significant hold on our world. Compound semiconductors, namely the III-V compounds and their alloys are exceedingly important to our society. After the realization of semiconducting devices based on Ge, there was a rush to research other semiconducting materials in the 1950s, this included the III-V compound materials. This class of semiconductors is inherently more polar than the group-IV materials; they are made up of, as the name suggests, one atom from group-III and one from group-V. From this increased polarity, or ionicity, there is a propensity for this class of materials to be more direct in nature, meaning the lowest point of the conduction band and the highest point of the valence band have the same k-vector. In comparison, both Ge and Si are indirect, meaning that electronic transitions generally require the assistance of a lattice vibration, a phonon, significantly decreasing the likelihood of an electronic transition. The increased direct nature of these materials also makes them better at light absorption and emission, both very important properties required for optoelectronic applications. A second consequence of the polar bonding arrangement is that the bandgap increases compared to the group-IV semiconductor from the same period.

It is these properties of III-V compounds that have led to their extensive use in technologies such as diodes for light emission and lasing, transistors, and integrated circuits. In particular it is the optoelectronic applications of III-V materials that make them so attractive. There are twelve commonly accepted III-V binary compounds, those containing one group-III atom from: Al, Ga, or In, and one group-V atom from: N, P, As, or Sb. These binaries all have distinct bandgaps and lattice parameters. The parameters of our binary alloys sets the boundaries for what is available, but we are not limited to only these values; there is nothing that keeps us from alloying these systems to create ternary, quaternary, or even more complex alloys.

This level of tunabilty has made the III-V compounds and their alloy systems ineluctable for optoelectronic applications. These ideas formed the basis to engineer the materials Holonyak and Bevacqua used to demonstrate the first light emitting diode able to emit in the visible region in 1962, effectively starting the field of optoelectronics.[8] Since this report researchers have been able to demonstrate other semiconductor lasers, transistors, integrated circuits, and even photonic integrated circuits at the commercial level using III-V materials.[9–11]

1.4 The Pursuit of Hybrid III-V-IV Alloys

The ubiquity of the preceding technologies has sparked a lot of interest in hybrid semiconductor alloys for quite some time. Beginning as early as 1974 researchers have striven to understand what happens when two seemingly disparate systems are combined. Additionally, research into these materials has been driven by the practical desire to have properties intermediate to both group-IV and III-V materials at hand. The extent to which group-IV and III-V semiconductors have been studied, and the maturity of their technological integration, has poised these hybrids as a candidate for next generation semiconducting materials. Alloys within this class can be thought of as pseudobinary systems with a general formula $(\text{III-V})_{1\text{-x}}(\text{IV}_2)_\text{x}$. These hybrid alloys are comprised of a polar, III-V, component and a non-polar, group-IV, component. These hybrids blend optical and electronic properties from both of these extensively studied end-members enabling their use in a wide range of optoelectronic applications. Industrially, one subclass of $(\text{III-V})_{1\text{-x}}(\text{IV}_2)_\text{x}$ alloys, are extremely interesting, those comprised of elements all from the same period, or row, of the periodic table; this particular subset of materials contains alloys in which the III-V and group-IV end-members have nearly identical lattice parameters but distinct electronic properties. This property allows for the decoupling of bandgap and lattice parameter, this is extremely important for applications such as photovoltaics where there is a strong desire to have materials with identical lattice parameters to prevent defect formation, but different bandgaps to increase efficiency. This subclass can be further extended due to the similar lattice parameters of Al/Ga systems, allowing for the use of AlAs or GaP in the place of GaAs or AlP respectively. In addition to being of technological value, these materials are an ideal system to study the physics arising from the interplay of diamond-like symmetry and the lower symmetry zincblende structure types, interactions of which have already been shown to possess intriguing properties from a fundamental perspective.[12–17]

Even though these materials have been captivating researchers since the 1970s, the field has progressed slowly for myriad reasons. The earliest reports of materials within this class were for the $(\text{GaAs})_{1\text{-x}}\text{Si}_\text{x}$ system and quickly followed by $(\text{GaSb})_{1\text{-x}}\text{Ge}_\text{x}$,

$(GaAs)_{1-x}Ge_x$, and even a superhard material $(BN)C_2$.[12–15,18–24] Systematic research of this class of materials has been hindered primarily by various phase segregation issues associated with the growth of these hybrid alloys. The extreme difficulty associated with the realization of hybrid (III-V)-(IV) materials has lead to diminished research efforts, so to fully explore these systems an innovative approach needs to be taken to circumvent synthetic issues.

Recently a new approach to the synthesis of hybrid alloys with compositions $(III\text{-}V)\text{-}(IV)_3$ was developed at Arizona State University, and this approach avoids the issues of phase segregation, auto-doping, and compositional fluctuations due to the end-members being chemically dissimilar. The strategy was to incorporate III-V pairs embedded within a group-IV matrix, disallowing compositional inhomogeneities including phase segregation with a limiting stoichiometry of $(III\text{-}V)\text{-}(IV)_3$. The first material realized using this synthetic method was $AlPSi_3$ in 2011, and was followed by the report of silicon rich analogues with a general formula $(AlP)_x(Si)_{5-2x}$, showing that the new methodology was indeed viable and robust.[25,26]

The exploration of these materials is made possible through the combination of carefully selected molecular precursors such as $P(SiH_3)_3$ and other hydrides with a general formula $V(IV\text{-}H_3)_3$ which contain preformed V-IV bonds, providing a significant shift from the metal-organic chemical vapor deposition (MOCVD) and molecular beam epitaxy (MBE) approaches which deliver each component separately. These specifically chosen molecules can then be combined with group-III atoms from an effusion cell to form intermediates containing all of the desired bonds which then desorb hydrogen as H_2 to form molecular building-blocks with a fixed stoichiometry. By combining $P(SiH_3)_3$ with Al atoms homogeneous monocrystalline layers with thicknesses approaching 1 μm, and bulk $AlPSi_3$ stoichiometry were grown directly on

Si(100) substrates.[25] The molecular intermediates formed are tetrahedral in nature and can interlink to produce a diamond-like lattice in which Al-P (III-V) pairs are embedded in a Si (group-IV) matrix as isolated donor-acceptor units. This arrangement ensures that the group-V atoms occupy a unique sublattice on which they are third nearest neighbors.[27] Thorough characterization indicates the tetrahedral units do in fact provide isolated donor-acceptor pairs, the tetrahedral building-blocks interlink to form an extended diamond-like lattice grown pseudomorphically on Si(100) with minimal defects and no obvious signs of phase segregation. This synthetic strategy though limited on one end to the (III-V)-IV_3 stoichiometry, 60% group-IV content, can be extended to higher group-IV concentrations while maintaining the integrity of the isolated III-V pair ideology. The Al-P-Si system was extended to include alloys with general compositions of $(AlP)_x(Si)_{5-2x}$ ($x = 0.3$-1.0), or Si content from 40-90%.[26]

This approach to the systematic development of hybrid (III-V)-$(IV)_3$ alloys has been extended beyond the Al-P-Si system. By changing the molecular precursor to $As(SiH_3)_3$, single phase, monocrystalline $AlAsSi_3$ was grown directly on Si(100), and mixtures of the $P(SiH_3)_3$ and $As(SiH_3)_3$ precursors generated $Al(As_{1-x}P_x)Si_3$ ($0 < x < 1$) alloys with As/P ratios that mirror those in the precursor mixtures.[27] AlP and AlAs both have a lattice parameters larger than Si, one possibly synthetic strategy to achieve full lattice matching for these alloy systems is through the incorporation of a smaller group-V atom. With judicious addition of $N(SiH_3)_3$ to the gas source precursors, $P(SiH_3)_3$ and $As(SiH_3)_3$, corresponding alloys of $Al(P_{1-x}N_x)Si_3$ and $Al(As_{1-x}N_x)Si_3$ with minor amounts of N (∼3% for the P, and ∼11% for the As case) can be deposited directly on Si(100).[28] In a similar fashion to the Si-rich $(AlP)_x(Si)_{5-2x}$ phases analogous $(AlAs_{1-y}N_y)_x(Si)_{5-2x}$ alloys have been extensively characterized for their structural and optical properties.[29]

The molecules $N(SiH_3)_3$, $P(SiH_3)_3$, and $As(SiH_3)_3$, that have been used in previous studies are not the only molecules that exist within this group of compounds. In addition to the Sb containing equivalent $Sb(SiH_3)_3$ there are analogous germyl derivatives that are expected to have similar reactivities towards electrophilic attack from the group-III atoms.

The remaining chapters of this dissertation are dedicated to the detailed description of synthesis, characterization, and performance evaluation of the new hybrid semiconductors in the In-P-Ge (Chapter 2), Al-B-P-Si (Chapter 3), Ga-P-Si (Chapter 4), and Ga-As-Ge (Chapter 5) systems. Each of these systems was targeted based on materials properties of the parent alloys, striving to extend the optoelectronic properties of Si and Ge based technologies.

Chapter 2 of this dissertation describes the synthesis of a new alloy system with a general formula $(InP)_yGe_{5-2y}$. The heavy atom analogue to $AlPSi_3$, $InPGe_3$, was targeted in hopes of achieving a direct-gap material, promoting facile light absorption and emission. These alloys were the first materials within this class to show photoluminescence. Ga-As-Ge alloys, discussed in Chapter 5, are comprised of pseudobinary end-members with similar lattice constants, and are an attractive candidate material for direct-gap materials lattice matched to Ge. Previous work, theoretical and experimental, show strong evidence for unprecedented bowing of direct- and indirect-gaps, opening the door to applications in the mid-IR. Materials which show enhanced optical behavior, emission and or absorption, in the mid-IR are extremely topical in civilian and military applications. These materials were only made possible through the availability of highly reactive gallane compounds. In addition to being reactive, it is required that the molecules be sufficiently volatile to be compatible with the deposition process. The molecular approach to the incorporation of Ga facilitated the production of the desired tetrahedral building blocks, in turn delivering the desired structure and composition. The molecular gallane approach originated with the synthesis of $GaPSi_3$ and Si-rich relatives described in Chapter 4. $GaPSi_3$ was a clear synthetic target due to the similarity in lattice parameter of GaP and Si, analogous to $AlPSi_3$. Synchronously, the replacement of Al with Ga was expected to extend the optical response further into the IR than the $AlPSi_3$ prototype. To extend the tunability of the $AlPSi_3$ system in the opposite, higher energy, direction Al was replaced with B in Chapter 3. Additionally, the incorporation of B on the group-III sublattice allowed for the $AlPSi_3$ system which has a lattice parameter slightly larger than Si to lattice match Si with alloy compositions $Al_{1-x}B_xPSi_3$. Combined, the wider bandgap and lattice matching are desired for Si-based tandem-cell photovoltaic (PV) applications. These alloys were realized through the development of gaseous precursors which replaced solid sources, $Al(BH_4)_3$ serves as a source of both Al and B atoms. The application of $Al(BH_4)_3$ was driven by its position as a readily available CVD compatible chemical comprised of earth-abundant atoms, making high-volume high-throughput fabrication of these materials industrially viable. In the final chapter the XXX

Chapter 2

RATIONAL DESIGN OF MONOCRYSTALLINE $(InP)_YGe_{5-2Y}$/Ge/Si(100) SEMICONDUCTORS: SYNTHESIS AND OPTICAL PROPERTIES

Figures and text in this chapter were reprinted with permission from Sims, P. E.; Chizmeshya, A. V. G.; Jiang, L.; Beeler, R. T.; Poweleit, C. D.; Gallagher, J.; Smith, D. J.; Menéndez, J.; Kouvetakis, J. *J. Am. Chem. Soc.* **2013**, 135, 12388-12399. Copyright 2013 American Chemical Society.[30]

Synopsis

This dissertation begins with a chapter on the synthesis of a new class of hybrid alloys described with the general formula $(InP)_yGe_{5-2y}$. These materials were grown on Ge-buffered Si substrates using specifically designed reactions between molecular $P(GeH_3)_3$ and elemental In generated as a gaseous atomic beam from an effusion cell in a gas-source molecular epitaxy reactor. The reaction mechanism likely involves the formation of $In{\cdot}P(GeH_3)_3$ intermediates which eliminate H_2 on the substrate surface to produce In-P-Ge_3 building-blocks with a tetrahedral structure in which the central P atom is surrounded by on In and three Ge terminal atoms. The resultant In-P-Ge_3 tetrahedra interlink to form an extended network solid in which isolated In-P pairs are embedded in a Ge diamond-like matrix. Departures from the ideal $InPGe_3$ stoichiometry are observed in this system due to the unimolecular decomposition of the highly reactive $P(GeH_3)_3$ compound, leading to the formation of Ge-rich analogues with Ge content exceeding the 60% threshold.

The purpose of the work was to search for new types of semiconductors within this class of hybrid alloys. The target solids are designed to approach direct-gap conditions in order to facilitate efficient light absorption and emission. The work in this chapter was successful in demonstrating the use of indium for the first time as the group-III element to generate the III-V sublattice of the hybrid alloy systems, and germanium as the group-IV tetrahedral component of the diamond-like sublattice. The chapter presents a detailed account of the fabrication and properties of these new materials, including the observation of photoluminescence for the first time in this class of semiconductors. First principles calculations are used to elucidate the structural and optical trends, and provide a comprehensive perspective of the present work relative to prior studies involving Al and Si in place of In and Ge components.

2.1 Introduction

The active materials in most electronic devices are either elemental semiconductors from group-IV of the periodic table or compounds based on one element from group-III and one element from group-V. Alloys combining elements from within each class of materials are well-known scientifically and very important in technology. On the other hand, interclass alloys of group-IV and III-V materials are expected to have unique properties and applications, but so far the dearth of general synthetic methodologies for the construction of single phase materials has prevented their widespread use and made the research of their properties very difficult.[12,17,18,20,23,31]

Very recently, we have introduced new synthetic pathways of the above inter-class tetrahedral semiconductors consisting of III-V donor-acceptor dimers incorporated intact within a host Si lattice. Our strategy suppresses phase segregation effects that until now prevented the development of materials in the general class of III-V and group-IV hybrids for optoelectronic applications. The crystal growth was conducted using gas-phase reactions of Al atoms with the $N(SiH_3)_3$, $P(SiH_3)_3$, and $As(SiH_3)_3$ molecules. We proposed that these form corresponding $Al{\cdot}N(SiH_3)_3$, $Al{\cdot}P(SiH_3)_3$, and $Al{\cdot}As(SiH_3)_3$ intermediate complexes which in turn eliminate H_2 to yield preformed $Al{\cdot}NSi_3$, $Al{\cdot}PSi_3$, and $Al{\cdot}AsSi_3$ tetrahedral cores. These are then self-assembled into single-phase monocrystalline epilayers via epitaxy-driven mechanisms in a manner that precludes the formation of thermodynamically unfavorable Al-Al bonds. To date, this approach has been used to grow new compounds such as $AlPSi_3$, $AlAsSi_3$, as well as corresponding alloys $Al(As_{1-x}P_x)Si_3$, $Al(As_{1-x}N_x)Si_3$, and $Al(P_{1-x}N_x)Si_3$. More generally, we have shown that an even broader range of compositions $Al(As, P, N)_ySi_{5-2y}$ is accessible, spanning stoichiometric phases ($y = 1$) which represent the maximum concentration (40%) of isolated (III-V) pairs to highly dilute system approaching the Si limit ($y \to 0$).[25–29] This work has generated growing interest from both theoretical and experimental perspectives because these materials have been predicted to exhibit unique absorption properties in a wavelength range needed for dramatic efficiency gains for the next generation of Si-based photovoltaics.[32,33]

In this chapter, the generality of this building-block approach is demonstrated by using reactions of In atoms and $P(GeH_3)_3$, the Ge molecular analogue of the above precursors, to synthesize $(InP)_yGe_{5-2y}$ tetrahedral semiconductors for the first time. As in the case of the silicon systems above, these materials are composed of isolated InP donor-acceptor dimers substituted within a diamond-cubic Ge parent lattice. In particular, InP was selected because it represents a well-known binary semiconductor widely used in modern photonics. Furthermore, from a synthesis perspective, the $P(GeH_3)_3$ precursor has been shown theoretically to combine favorably with In atoms to form the hypothetical In·P$(GeH_3)_3$ intermediate complexes en route to the desired In·PGe_3 building blocks. It is anticipated that these Ge-based materials may have applications in various fields of optoelectronics, including direct-gap laser materials and semiconductors with widely tunable infrared band gaps. From a fundamental perspective, this alloying strategy represents a viable approach to extending the basic properties and optical capabilities of Ge by controlling the crystalline composition at the nanoscale via substitution of Ge-Ge bonds by In-P pairs. As shown below, the alloying maintains the molar volume close to that of Ge, allowing facile integration on Ge-based platforms. The recent advent of commercial quality Ge-buffered Si wafers introduces intriguing opportunities for this system in the area of heteroepitaxial photonic applications straddling the properties of the ubiquitous InP and Ge end-systems. This work utilizes the above platforms to fabricate a new series of monocrystalline $(InP)_yGe_{5-2y}$ alloys with y = 0.70-0.30 corresponding to molar concentrations between 30 and 10%. Structural characterization shows that materials across the entire concentration range exhibit tunable lattice constants that closely follow Vegard's linear interpolation between the InP and Ge end-members. Initial spectroscopic ellipsometry studies indicate InP-rich alloys approaching the stoichiometric limit exhibit dielectric properties distinct from those of pure InP or Ge while the Ge-rich counterparts possess Ge-like transition energies. Photoluminescence (PL) studies suggest this approach may enable compositional tuning of direct gaps below that of Ge (0.80 eV) in the near-infrared. Raman scattering contradicts the possibility of phase separation but supports the existence of isolated "In-P" dimers within a crystalline Ge host matrix. The latter bonding motif is corroborated by density functional theory simulations at both the molecular and solid-state level which reproduce the observed compositional dependence of the lattice constants and provide direct support for the notion that the $(InP)_yGe_{5-2y}$ materials can be formed via assembly of In-P-Ge_3 building blocks over the full range of compositions explored.

2.2 Experimental

The $(InP)_yGe_{5-2y}$ films were grown on Ge-buffered Si wafers by gas-source molecular beam epitaxy (GS MBE) at 300-450 °C. The Ge-buffers were grown on 4 inch *p*-type Si(100) with 1-10 Ω-cm resistivity via previously developed deposition protocols using a pure tetragermane source. This technique produces highly aligned monocrystalline films with atomically flat surfaces devoid of defects as required for subsequent use as templates. The as-grown Ge/Si(100) wafers were cleaved to 1.0×1.5 cm^2 size substrate segments that fit the dimensions of the sample stage. Each substrate was sonicated in 10% HF/methanol and pure methanol baths for 5 minutes each, dried under a stream of nitrogen, and inserted into the chamber via a load lock at 3.0×10^{-10} Torr. The substrate was then heated at 600 °C under vacuum to remove residual impurities from the surface. Prior to growth, the temperature of the wafer was adjusted to the desired setting using a single-color pyrometer. The crystal nucleation was initiated by first introducing the In atoms generated by a Knudsen cell into the growth chamber. The gaseous $P(GeH_3)_3$ source was then admitted through a nozzle 2-3 cm away from the substrate holder. After a brief period of equilibration in the reaction zone, the sample stage was rotated to expose the growth surface to the combined incoming flux of the reactants and commence the film growth process. The gas flow was subsequently controlled by a needle valve at a steady rate giving a nominal 1:1 molar ratio with the In atoms. The evaporation rate of the latter was regulated by the temperature of the Knudsen cell. The reaction pressure was maintained constant at $\sim8.0\times10^{-6}$ Torr via dynamic pumping using a turbo pump. The typical deposition time frame was 30-60 minutes to produce films with thicknesses in the range of 350-1250 nm at growth rates between 17 and 22 nm/minute depending on temperature.

2.3 Results and Discussion

Previously, it was shown that $P(GeH_3)_3$ reacts readily at temperatures as high as 430 °C via complete elimination of H_2 to produce device quality *n*-type Ge layers doped with P atoms.[34] Under these conditions, the compound delivers the entire PGe_3 molecular core which incorporates intact into the crystal leading to the formation of atomically flat monocrystalline semiconductor layers. This finds that reactions of $P(GeH_3)_3$ and In atoms yield uniform and crystalline $(InP)_yGe_{5-2y}$ layers only within a narrow operating temperature range from 430 to 330 °C, in which the upper limit coincides with the one determined in the doping studies of the $P(GeH_3)_3$ source. Within the optimal window, the concentration of InP varies from 10% at 430 ° C to 30% at 330 °C, never reaching the 40% stoichiometric limit corresponding to $InPGe_3$. Note that this trend follows the one observed in the $(AlP)_ySi_{5-2y}$ systems.[26] However, the stoichiometric $AlPSi_3$ (40% AlP) was attained at the lower temperature range in those experiments. Above the viable 430-330 °C growth window, the highly reactive $P(GeH_3)_3$ rapidly dissociates to form PH_3, precluding the reaction with indium to form the desired gas phase $In{\cdot}P(GeH_3)_3$ entities and ultimately yielding rough samples through segregation of elemental In and Ge precipitates. Attempts to lower the reaction temperature below 330 °C also yielded poor noncrystalline products akin to those found for $T > 430$ °C. In this case, the activation barrier to form and/or dehydrogenate the intermediate $In{\cdot}P(GeH_3)_3$ complex may be too high to allow assembly of crystalline materials based on $InPGe_3$ cores. Accordingly, under the latter growth conditions, the observed film stoichiometries straddle 30% (i.e., $InPGe_{4.5\text{-}3}$) but never reach the 40% limiting value (i.e., $InPGe_3$) as indicated above.

The proposed pathway is consistent with the control experiments of single-source $P(GeH_3)_3$ depositions (in the absence of In) over the same optimal growth window, which yield substantial Ge film growth on the buffer layer surface. Accordingly, the depletion of (In, P) with increasing temperature in the alloys can be explained by the facile decomposition of $P(GeH_3)_3$ as described by a chain of thermally activated side reactions:

$$P(GeH_3)_3 \rightarrow PH(GeH_3)_2 + GeH_2 \rightarrow PH_3 + 3GeH_2 \tag{2.1}$$

In this scenario, volatile byproducts of the $PH_x(GeH_3)_{3\text{-}x}$ (x = 1-3) variety are eliminated. These do not react with In atoms and are thus pumped away, while the highly reactive GeH_2 (germylene) species remain on the surface and incorporate in the crystal as Ge atoms. The net result is a Ge-enriched lattice comprised of tetrahedral $InPGe_3$ units interlinked with Ge atoms.

On the basis of the above synthesis strategy, a series of alloys were grown and characterized. The film morphology was examined by Nomarski imaging, revealing a typically smooth surface with no cracks or other imperfections visible throughout the wafer surface. This was corroborated by AFM measurements, which gave relatively low RMS roughness of ~1.5-2 nm from 20 μm ×20 μm areas. The sample thickness, and crystallinity were determined by Rutherford backscattering spectrometry (RBS). Random spectra acquired at 2.0 and 3.7 MeV showed distinct signals corresponding to In, Ge, and P (see Figure 2). The 3.7 MeV measurements were used to clearly separate Ge peaks from the films and the buffer in samples thicker than ~200 nm, thereby allowing precise quantification of the chemical composition. The films grown

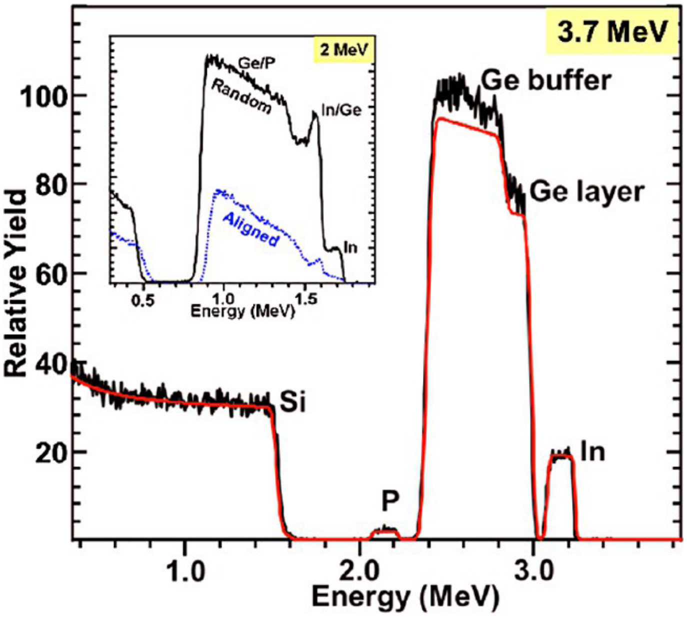

Figure 2: 3.7 MeV RBS spectra of In-P-Ge film grown on Ge/Si(100) showing distinct signals of the elements in the epilayer and Ge-buffer. Quantitative modeling of the random trace (red line) yields and average composition of $InPGe_6$ (75% Ge) (black line) and a thickness of 200 nm. Inset: 2.0 MeV spectra of the same sample showing a high degree of channeling consistent with the full substitutionality of the three elements in the cubic alloy structure.

at 330 °C typically exhibited a nominal RBS stoichiometry of $InPGe_{4.5\text{-}5}$ (using the more compact notation $InPGe_{(5\text{-}2y)/y}$ instead of the standard $(InP)_yGe_{5\text{-}2y}$, which can also be described as 30% InP and 70% Ge. The films produced between 330 and 430 °C contained a Ge fraction spanning the 70-90% range. In all cases, the In:P ratio was found to be 1:1 (30-10% InP), suggesting that these Ge-rich systems are likely formed by replacing Ge-Ge dimers in the parent structure by In-P pairs. RBS channeling indicated monocrystalline and highly aligned materials. The ratio of the aligned versus random peak heights ($\chi_{\min}$) of the In, Ge, and P were found to be nearly the same in any given sample indicating complete substitution of the atoms in the same structure.

The RBS analysis indicated the Ge-rich layers produced at the higher temperatures typically exhibited a large thickness on the order of 0.8-1.2 μm owing to higher growth rates afforded by the increased thermal activation of the reactants. The lattice dimensions and strain properties of these materials were measured by high-resolution X-ray diffraction (HR-XRD). In general, the XRD analyses show the layers are compressively strained as a result of the mismatch between the alloy and the Ge template. Note the Ge templates exhibit a slight tensile strain induced by heating the wafers to 600 °C to desorb the surface oxide then quenching to room temperature prior to growth yielding $a = b = 5.668$ Å and $c = 5.649$ Å. This tetragonal deformation fortuitously offers an advantage over bulk Ge because the slight increase in the in-plane lattice parameter allows better lattice matching of the epilayers with the target alloys.

The $\theta/2\theta$ scans of the Ge-rich epilayers typically revealed a strong but asymmetric peak with angular position clearly distinct from that of either InP or elemental Ge. The origin of the asymmetry is a result of a shoulder peak at lower diffraction angle with d-spacing very close to that of the main reflection. The off-axis (224) reciprocal space maps revealed two closely spaced broad peaks with asymmetrical shapes that extend to the right of the pseudomorphic line toward higher reciprocal Q_x values or a smaller d-spacing (see Figure 3). These two peaks correspond, respectively, to a fully strained bottom and an over-relaxed top of the $(InP)_yGe_{5-2y}$ layer. The (224) and (004) XRD plots were analyzed to determine the in-plane (a) and vertical (c) parameters for the two regions, indicating the alloy layer in this case is gradually over-relaxing relative to the Ge-buffer.

As an example, the (224) ($\phi = 0°$) plots of an $InPGe_{15}$ layer with thickness of 900 nm showed a double peak structure yielding in-plane lattice parameters $a_1 = 5.6648$ Å and $a_2 = 5.6445$ Å. The first corresponds to a fully strained layer adjacent to the

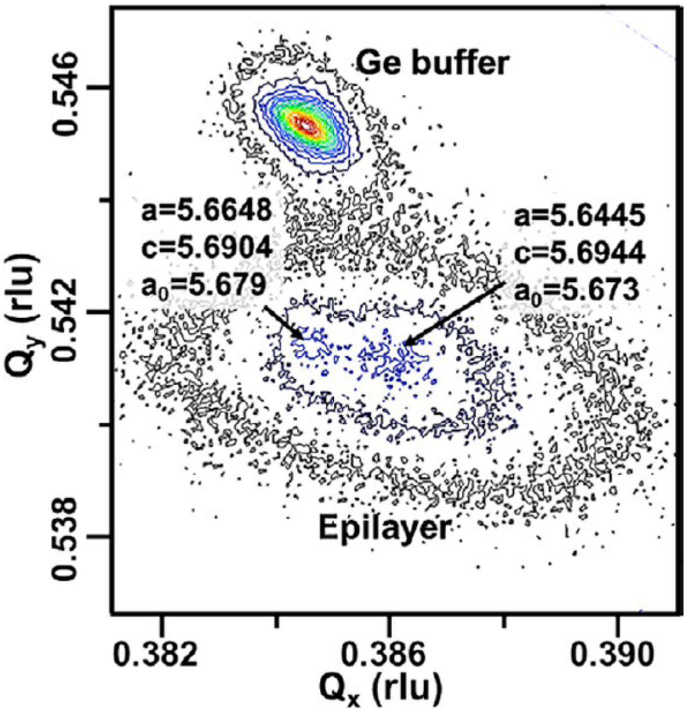

Figure 3: XRD (224) reciprocal space map of $InPGe_{15}/Ge/Si(100)$ (88% Ge) showing separate peaks for the fully strained bottom and over-relaxed top sections of the film. In both cases, the plots yield very similar values for the relaxed lattice constants (a_0), indicating no significant change in molar volume across the sample.

interface, while the other is slightly smaller consistent with the over-relaxation in the upper segment of the layer. The corresponding vertical lattice constants are smaller ($c_1 = 5.6904$ Å) near the interface and larger ($c_2 = 5.6944$ Å) in the over-relaxed region of the film. Collectively, the data indicate the molar volume is essentially preserved across the film as evidenced by the nearly equal values of the relaxed lattice parameters $a_{0,1} = 5.679$ Å and $a_{0,2} = 5.673$ Å. The latter are calculated by linearly interpolating the C_{12}/C_{11} elastic constant ratios of Ge and InP and are found to be close to the Vegard's law average of 5.683 Å determined using $a_{\mathrm{InP}} = 5.8687$ Å and $a_{\mathrm{Ge}} = 5.658$ Å. To exclude lower symmetry orthorhombic deviations in the over-relaxed samples, the $(\bar{2}24)$ ($\phi = 90°$) reciprocal space maps was also measured. The diffraction plots in this case were found to be virtually identical for both the (224) and ($\bar{2}$24) maps each showing two peaks with matching reciprocal point values yielding in-plane lattice constants within the error of the measurement (Δa/a $\sim$ 0.02%). Finally, note that similar observations of tetragonal over-relaxation of misfit strain has previously been found in heavily carbon doped GaAs films and are attributed to the formation of unusual defect structures.[35]

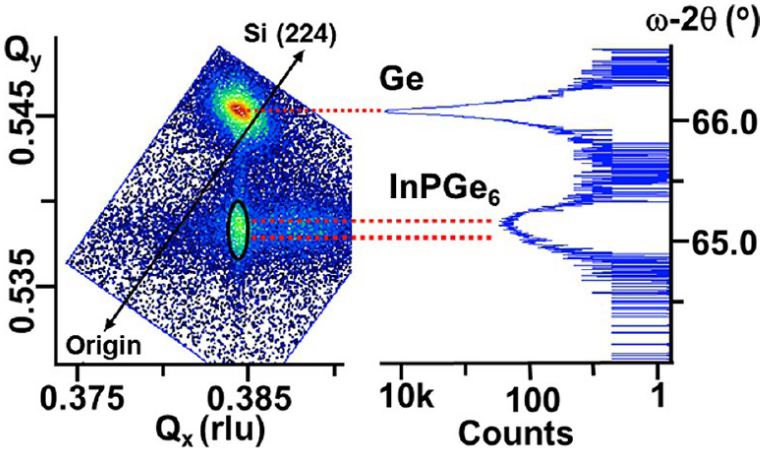

Figure 4: XRD plots of $InPGe_6$/Ge/Si(100). (left) Reciprocal space maps in the vicinity of the (224) reflection of the cubic structure showing in-plane lattice matching between the compressively strained epilayer and the tensile strained buffer. Note the Ge peak maximum lies above the relaxation line (double arrow) as expected. (right) Corresponding (004) 2θ plot of the heterostructure showing a slightly asymmetric and broad alloy peak relative to that of the Ge-buffer. The XRD data confirm the high crystalline quality of the epilayer.

For samples grown at lower temperatures in which the InP concentration is increased from ~20 to 30% ($InPGe_9$ to $InPGe_{4.5}$), the diffraction data show sharper and more intense asymmetrical (004) peaks due to improved crystallinity (see Figure 4 for typical diffraction patterns). In all cases the (224) reciprocal space map (RSM) analogues exhibit a corresponding sharp and highly intense diffraction map that is elongated in the vertical direction and exactly aligned with the Ge-buffer peak along the pseudomorphic line, indicating perfect in-plane lattice-matching between the two materials. Figure 4 shows XRD plots for a representative $\mathrm{InPGe}_{6.3}$ (76% Ge) film with thickness of 350 nm. The (004) reflection contains a strong main peak and a lower intensity shoulder, yielding $c = 5.7211$ Å and $c = 5.7280$ Å, respectively. As shown by the dotted lines, the (224) counterparts overlap in the vertical direction (same Q_x values), yielding a common in-plane lattice constant $a = 5.668$ Å which is identical to that of the underlying Ge, indicating the epilayer is pseudomorphic. The calculated a_0 values in this sample are 5.702 Å and 5.698 Å, which are both close to the Vegards's law value $a_\mathrm{Vegard} = 5.709$ Å. The slightly different (c) lattice dimensions are attributed to small variations in alloy concentration as discussed below. It is worth noting the over-relaxation behavior appears to be a strong function of thickness and not composition. For a range of sample with different Ge compositions, layer over-relaxation is not observed in thinner films because they are within range of their critical thickness. A Ge-rich InPGe_9 (82% Ge) film with thickness of 1200 nm shows over-relaxation throughout a significant portion of the layer, while the effect appears to be absent in a 300 nm analogue grown with virtually identical composition.

As shown in Figure 4, in addition to sharp (224) diffraction spots,in most samples a broad, diffuse background whose maximum intensity is significantly weaker but above the noise level relative to the primary peak is observed. The center of this feature exhibits a slightly smaller (224) d-spacing than that of the main peak, indicating a correspondingly reduced (a) parameter, by an average of 0.04 Å in thinner samples. With increasing sample thickness from 100 to 600 nm, this feature significantly increases in intensity and systematically coalesces with the pseudomorphic peak. In these cases, the (004) counterpart shows a similar Q_y value for both peaks, implying a slightly reduced (1-1.5%) molar volume of any materials associated with this broad scattering. This observation is difficult to reconcile with measurable variations in composition. However, the increase of intensity of the secondary diffuse peak is consistent with scattering from misalignment or over-relaxation of columns in the upper portion of the layer, leading to defects localized near the free surface. Ultimately, the coalescence of the (224) peaks with increasing thickness culminates in diffraction maps of the type described for the over-relaxed structure in Figure 3 for 900 nm thick samples where two closely spaced broad peaks with asymmetrical shapes in essence virtually coincide. Another possibility consistent with the absence of compositional change is the existence of a strain-induced polymorphic structure with reduced molar volume, for which a tetragonal strain distortion is stabilized.

Further structural analysis was conducted using cross-sectional transmission electron microscopy (XTEM), which demonstrated the presence of smooth, uniform, and crystalline layers exhibiting comparable thicknesses to those estimated by RBS. Figure 5 is a representative Z-contrast image of the most commonly found microstructure showing a sharp uniform interface between the slightly brighter alloy region and the Ge-buffer. High-resolution images (inset) from the interface region taken in [110] projection exhibit elongated bright spots corresponding to pairs of In-P-Ge atoms or "dumbbells". The XTEM micrographs of these samples also reveal highly oriented columnar features that appear to extend downward from the surface through a significant portion of the layer. Toward the surface where the sample is thinner, the film clearly exhibits a nearly periodic pattern of parallel striations aligned along the growth axis. These are likely associated with slight inhomogeneities of the alloy composition induced by fluctuation in growth conditions including temperature, pressure, and possibly precursor flux, all of which may have a significant effect on the instantaneous growth rate. This observation is not unexpected because both the complexity of the reaction mechanism and the crystal assembly at ultra-low temperatures employed here are both exceedingly sensitive to such fluctuations.

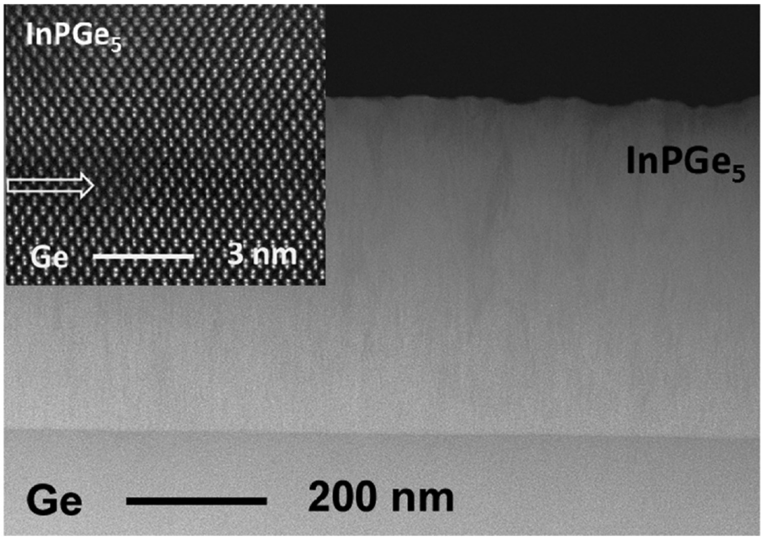

Figure 5: Z-Contrast STEM image of $InPGe_5$ films (brighter contrast) grown on Ge-buffer with thickness of ∼500 nm showing columnar features and vertical striations particularly near the top thinner portion of the layer. Inset: Z-Contrast high-resolution image from interface region between the film and Ge-buffer showing high quality epitaxy and sharp Ge-$InPGe_5$ heterojunction marked by the arrow.

To further investigate possible compositional variations, atomic-level EDX analysis with a 1.5 Å electron probe to study the uniformity of elemental distribution at the nanoscale was conducted. Typical elemental profiles were scanned both horizontally across columns and vertically within a given column in the film. In both cases, all three constituent elements, In, P, and Ge, appeared in every atomic-scale region probed, without any indication of phase segregation of individual elements. The atomic-resolution analysis results thus confirm the film contains an alloy of Ge and In-P at the atomic scale. Figure 6 shows a representative high-resolution image in the [110] projection clearly showing continuous []111[] lattice planes of the cubic structure spanning a field of view containing a column (bright region) and its adjacent boundary

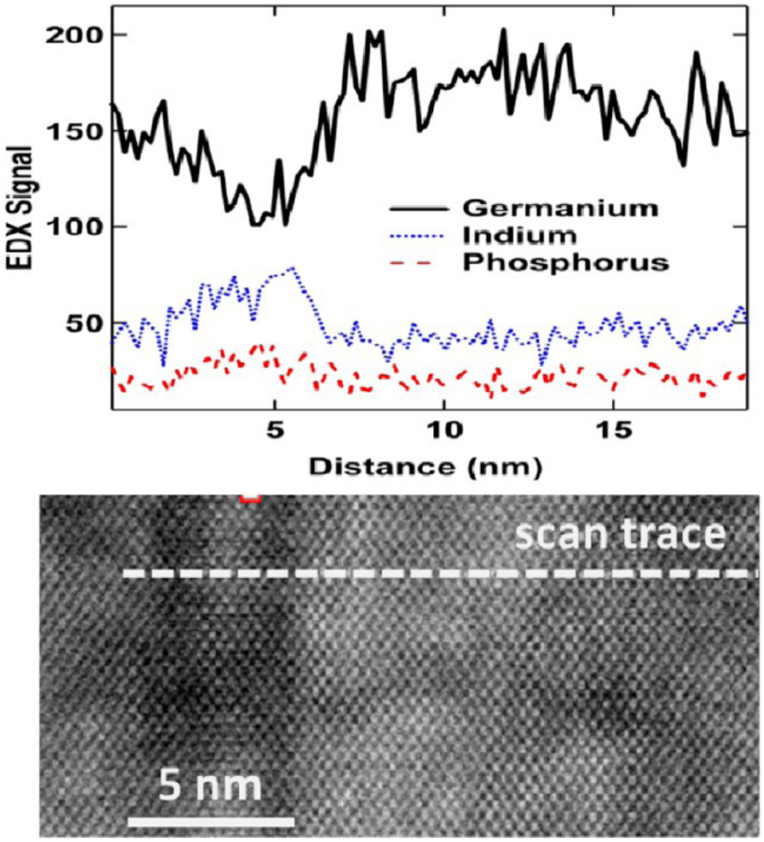

Figure 6: (top) EDX elemental profile scan of Ge (black line), In (blue line), and P (red line) sampled across 20 nm of a film with average $InPGe_5$ RBS composition, showing the distribution of all three constituent elements. (bottom) Bright field high-resolution image showing the region where the analysis took place on the film at the edge of a column and its boundary (darker intensity band at right). The scan is marked by a white dotted line in the upper portion of the image.

(dark vertical band), with no visible discontinuity or local defects of the crystal lattice across both regions. The horizontal EDX line scans show the elemental profiles are uniform across the column whose average RBS composition is determined to be close to $InPGe_5$. However within the narrow boundary region, the corresponding Ge/InP EDX counts show a sharp decrease/increase representing compositional variations of the type discussed above. In this example, the changes in Ge and InP content are estimated to correspond to $InPGe_{3.5\text{-}4}$, which is closer to the target stoichiometric $InPGe_3$ limit.

The above analysis is consistent with the XRD data for this sample, which also showed the main (004) peak and a shoulder in analogy with the alloy described in Figure 4. The latter peak gives a slightly larger lattice constant corresponding to InP-rich material of the type observed at the boundary of columns in the TEM images. The calculated relaxed lattice constants for the bulk material and the more concentrated narrow bands are 5.703 Å and 5.707 Å, which on the basis of Vegard's law correspond to $InPGe_5$ and $InPGe_4$ respectively. This is consistent with the estimates provided by the nanoanalysis results in Figure 6. Note this compositional change corresponds to an increase in molar volume and cannot be associated with the diffuse peak discussed earlier, which in this case has almost coalesced with the main peak in the XRD spectra.

Next, optical characterization of the alloys were conducted using spectroscopic ellipsometry (SE), photoluminescence (PL), and Raman scattering to investigate their dielectric function, direct gap emission, and local bonding properties. Figure 7 shows the complex pseudodielectric function for the $InPGe_5$ sample in Figures 5 and 6 and for the $InPGe_{15}$ sample in Figure 3, measured using a variable-angle spectroscopic ellipsometer (VASE from J.A. Woollam Co.) with a computer-controlled compensator. The results were compared with the dielectric function of bulk Ge to highlight the qualitative similarities with the Si-based III-V-IV_3 systems, for which the dielectric function has a line shape similar to a broadened Si dielectric function. In the $(InP)_yGe_{5\text{-}2y}$ case, the data in Figure 7 appear as a broadened Ge dielectric function. Whereas the broadening is small for $InPGe_{15}$, as expected, it is substantial for $InPGe_5$. In the latter sample, clear evidence for of a downshift in the so-called

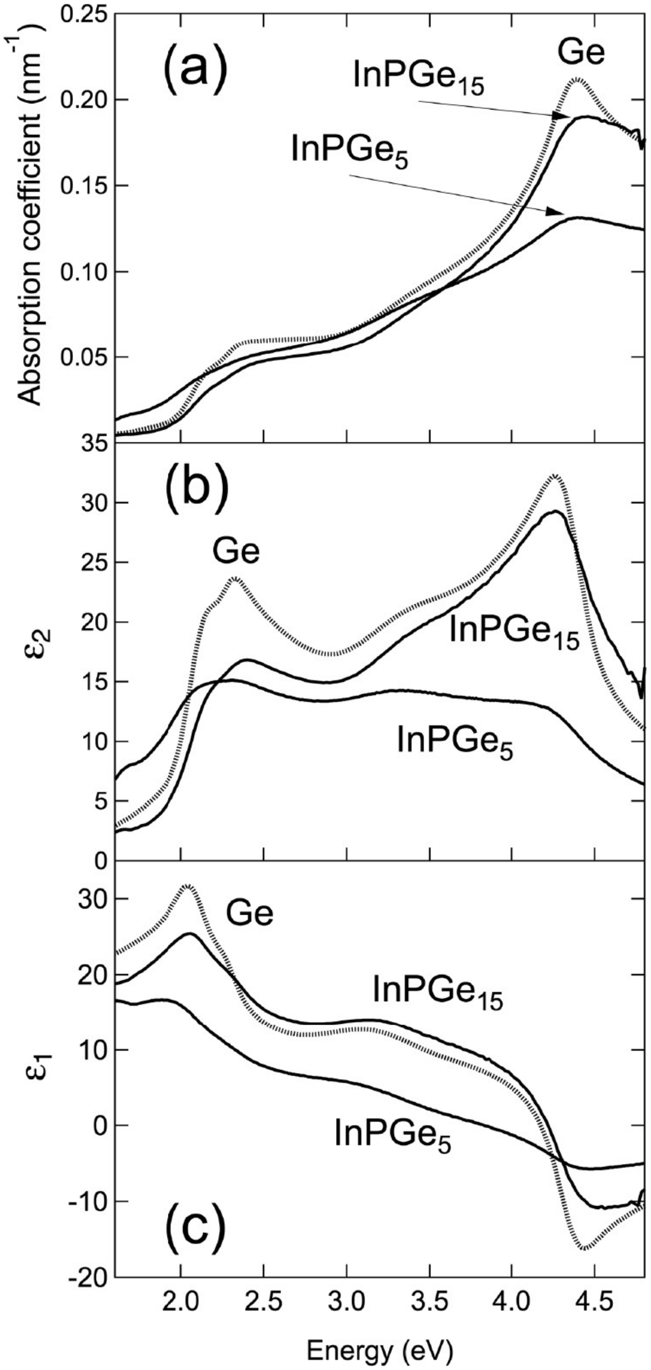

Figure 7: (a) Absorption coefficients calculated from ϵ_1 and ϵ_2. (b) Imaginary (ϵ_2) and (c) real (ϵ_1) parts of the pseudodielectric function of two $(\mathrm{InP})_{\mathrm{y}}\mathrm{Ge}_{5\text{-}2\mathrm{y}}$ films (solid black lines) compared with the dielectric function of bulk Ge (grey line)

$E_1/E_1+\Delta_1$ transitions in the 2.0 to 2.5 eV range are seen. The $E_1/E_1+\Delta_1$ transitions in InP appear at substantially higher energies than Ge,[36] so the downshift observed implies a large quadratic term with a coefficient (bowing parameter) close to b = 2 eV. Such large bowing coefficients are in qualitative agreement with findings in the III-V-Si systems.[39,40] When the linear interpolation is applied to the lowest direct (Γ-point in the diamond Brillouin zone) and indirect (L-point) gaps, predictions indicate the material becomes a direct gap semiconductor for $x > 0.5$, as seen in Figure 8. The predicted band gap value at the indirect-to-direct transition is $E_0 \sim 0.9$ eV. To

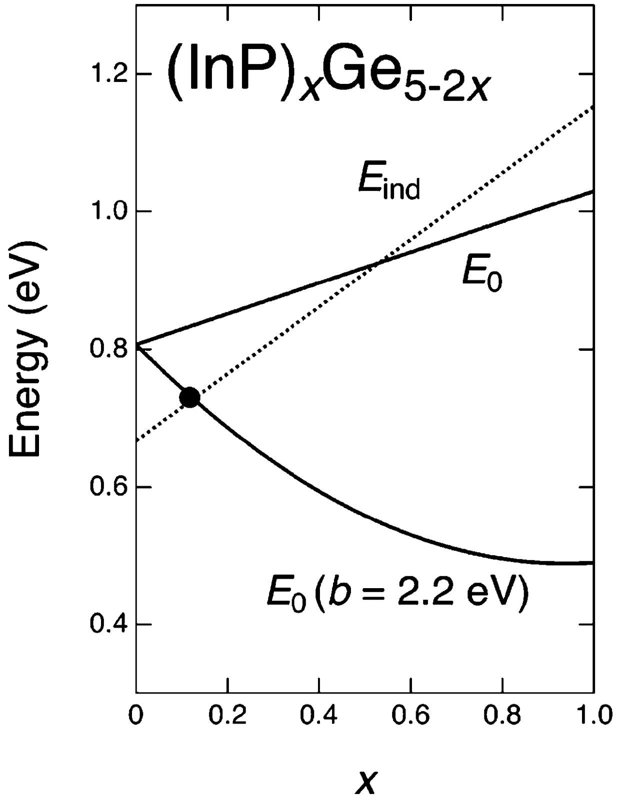

Figure 8: Straight lines show linear interpolations between the direct (solid line) and indirect (dotted line) band gaps of Ge and InP, with data from references as discussed in the text.[36–38] The circular dot shows the measured energy of the PL peak in sample $InPGe_{15}$, and the solid curved line is a calculation of the direct gap of the alloy with a bowing parameter of b = 2.2 eV

shed some light on the possibility of direct gap $(InP)_yGe_{5\text{-}2y}$ alloys, preliminary PL experiments were performed. The samples were excited with 400 mW from a 980 nm laser, and the emitted light was analyzed with a Horiba Micro-HR spectrometer equipped with an extended InGaAs detector. Figure 9 shows results for the $InPGe_{15}$ sample. A clear peak near 1700 nm (0.73 eV) mounted on a sloping background is observed, which may be associated with defects.[41] For the $InPGe_5$ sample (not shown), a rising PL intensity approaching the detector cutoff wavelength is observed, suggesting a PL peak below 0.6 eV.

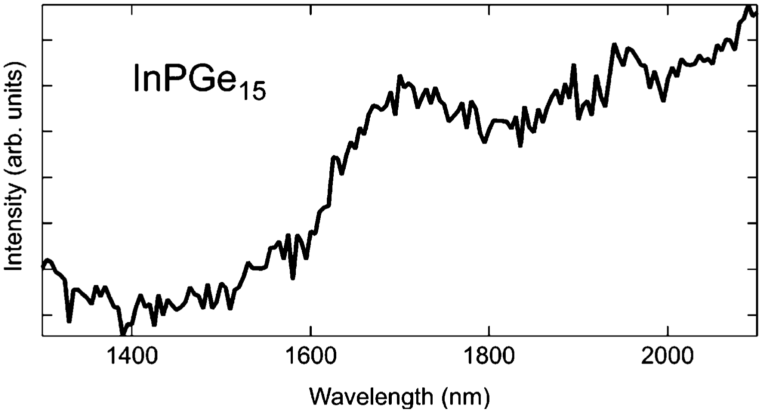

Figure 9: Room temperature photoluminescence of an $InPGe_{15}$ film obtained with 980 nm excitation. The peak near 1700 nm is tentatively assigned to the direct gap E_0 based on similar studies of Ge films. The rising background is probably due to dislocation luminescence

The PL peak energy for the $InPGe_{15}$ sample is shown as a dot in Figure 8, and it is in good agreement with the predicted indirect gap for this composition. However, the agreement may be fortuitous. First, there is no universal agreement as to the exact value of the lowest indirect gap in InP.[42] The value obtained in an empirical pseudopotential calculation of the band structure of InP is used.[37] Because the temperature dependence of this transition is not well-known either, we obtained room temperature values by assuming that the temperature dependence of the direct and indirect edges is the same and using the measure temperature dependence of the E_0 transition.[36] This gives $E_L = 1.88$ eV at room temperature. More importantly, the assignments of the PL peak to the indirect transition would imply that the bowing of the lowest direct and indirect gaps is very small, which appears unlikely. In fact, a bowing parameter $b = 2.2$ eV, very similar to the observed bowing for the $E_1/E_1+\Delta_1$ manifold, would bring the direct gap energy in agreement with the experimental data point, as seen in Figure 8. Moreover, such a large bowing parameter would imply a lower direct band gap for the $InPGe_5$ sample, as appears to be the case experimentally. Therefore it is not possible at this time to unambiguously assign the PL peak in Figure 9. Substantial additional work, both experimental and theoretical, will be needed to elucidate the nature of the lowest band gap in these systems, but the resultant and theoretical analyses do suggest that $(InP)_yGe_{5-2y}$ may be a direct-gap semiconductor over a broad range of compositions. On the experimental side, the role of compositional fluctuations such as those suggested by Figure 6 must be carefully analyzed, particularly in regard to the PL experiments. On the theoretical side, density functional theory calculations within the local density approximation are shown below which suggest a direct band gap for $y = 1$, but more accurate band structure methods are required to make reliable predictions.

Figure 10 compares the Raman spectrum of two $(InP)_yGe_{5-2y}$ samples with that of pure Ge, obtained with 364 nm excitation. At this wavelength, the penetration depth of the light is very small and the signal can be assigned to the top film only. The main Raman peak in the alloy samples is attributed to Ge-Ge vibrations, as it is clearly derived from the Ge Raman peak. The alloy peak is somewhat asymmetric, as observed in other alloy systems, and significantly broadened (by a factor larger than two) with respect to the Ge reference. At the highest InP concentration, a clear

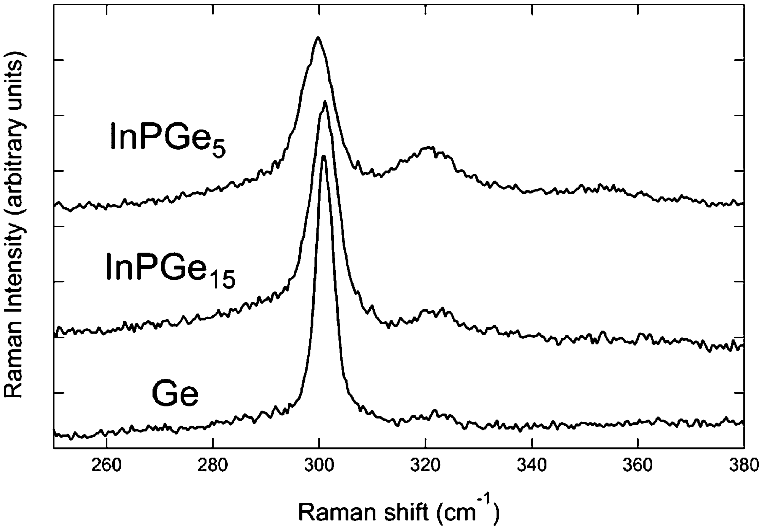

Figure 10: Unpolarized, room temperature Raman spectrum of two $(InP)_yGe_{5-2y}$ samples compared with the Raman spectrum of bulk Ge obtained under the same experimental conditions.

downshift of 0.9 cm^{-1} is seen. These results provide strong evidence of single-phase material precluding phase separation. Whereas the presence of InP pairs uniformly distributed over the Ge matrix accounts for the observed broadening and downshift, similar results can only be observed in Ge for particle sizes of about 10 nm.[43] However, the presence of such small crystallites is clearly inconsistent with the single-crystal nature of these films as evidenced by the electron microscopy and X-ray diffraction studies. Moreover, the pure InP TO and LO Raman modes at 304 and 345 cm^{-1}, respectively, are not observed.[44] A relatively narrow second peak is seen near 320 cm^{-1}, and in the InPGe$_5$ sample there is a hint of a third feature emerging near 355 cm^{-1}. The intensity of the 320 cm^{-1} peak appears to scale with InP concentration, and it is tempting to assign it to vibrations involving InP bonds in $(InP)_yGe_{5-2y}$. By subtracting the shifts induced by the long-range Coulomb interaction (LO-TO splitting) in bulk InP, an optical mode frequency of 318 cm^{-1} is obtained. Because the LO phonon branches in InP are extremely flat, the highest vibrational mode of an isolated InP pair (involving mainly P-atom displacements) should remain close to 318 cm^{-1}.[45] From this perspective, the observed mode frequency in the 319-322 cm^{-1} range, as seen in Figure 10, appears as reasonable, particularly if the fact that the InP bond in a Ge matrix should be under compressive strain is taken into account, which upshifts the frequency. On the other hand, there is a weak peak at about the same frequency even in bulk Ge. This is a second-order Raman feature that has been reported previously.[46] Therefore, an alternative explanation for the 320 cm^{-1} peak is second-order Raman scattering involving mainly Ge-like modes, which for 364 nm excitation could become more resonant in the $(\mathrm{InP})_y\mathrm{Ge}_{5-2y}$ material due to changes in the electronic structure induced by alloying. Selective resonances of specific second-order Raman features have already been reported for Ge.[47]

The frequency shift of the main peak relative to bulk Ge can be rationalized in terms of a simple model that considers the main contributions to frequency shifts in alloy semiconductors.[43] For the Ge-Ge mode in $\mathrm{Ge}_{1-z}\mathrm{Si}_z$ alloys, this shift can be written as:

$$\Delta\omega(z) = \mathrm{A}\omega_0 z + \mathrm{B}\omega_0(1 - a^{**})\frac{\Delta a_0(z)}{a_0} \tag{2.2}$$

where A and B are constants, ω_0 and a_0 are the bulk Ge Raman frequency and lattice parameter respectively, a^{**} is the bond rigidity parameter defined by Cai and Thorpe, and Δa_0 is the difference in lattice parameter between the alloy and bulk Ge.[48] The first term in Equation 2.2 is the so-called "mass" contribution, which mainly arises from the presence of atoms of different masses from those with large amplitudes in the Raman-active vibration. The second term is the "bond" contribution, which is caused by the bond distortions required to accommodate the alloys average lattice parameter. The constants A and B have nearly universal values for all group-IV alloys semiconductors, and for the Ge-Ge mode the fit values are A = 0.11 and B = 2.60, very close to the theoretically expected values of A = 0.1 and B = 3 based on a simple model.[39] When the alloy is grown as a thin film on a substrate, there is an additional contribution to the frequency shift due to the epitaxial strain, which in the case of (001)-oriented Ge is given by:

$$\Delta\omega^{\mathrm{EPI}} = -\gamma(2\epsilon_{\parallel} + \epsilon_{\perp})\omega_0 - \frac{2}{3}a_{\mathrm{s}}\omega_0(\epsilon_{\parallel} - \epsilon_{\perp}) \tag{2.3}$$

Here $\epsilon_{\parallel}$ and $\epsilon_{\perp}$ are the components of the strain tensor parallel and perpendicular to the film surface, γ is the Grüneisen parameter, and a_s the shear phonon deformation parameter. For Ge, $\gamma = 0.96$ and $a_s = 0.23$.[49] Assuming the validity of Equations 2.2 and 2.3 for $(\mathrm{InP})_{\mathrm{y}}\mathrm{Ge}_{5\text{-}2\mathrm{y}}$ alloys, using $\mathrm{z} = \frac{2\mathrm{y}}{5}$ and the parameters for the Ge-Ge mode in $\mathrm{Ge}_{1\text{-}\mathrm{z}}\mathrm{Si}_{\mathrm{z}}$, a shift of -2.8 (-9.0) cm^{-1} is predicted for the InPGe_{15} (InPGe_5) samples in Figure 10. This should be compared with the experimentally observed shifts of 0 cm^{-1} (InPGe_{15} and -0.9 cm^{-1} (InPGe_5). It is therefore apparent the Ge-Ge mode in $\mathrm{Ge}_{1\text{-}\mathrm{z}}\mathrm{Si}_{\mathrm{z}}$ alloys and the Ge-Ge mode in $(\mathrm{InP})_{\mathrm{y}}\mathrm{Ge}_{5\text{-}2\mathrm{y}}$ alloys cannot be described with a common model. It is instructive to speculate on the origin of this difference. To the extent that both systems follow Vegard's law to a very good approximation, it is hard to see why the terms in Equations 2.2 and 2.3 related to bond deformations (either in the relaxed alloy or induced by epitaxial strain) should be very different in the two systems. For the "mass" term in Equation 2.2, on the other hand, the physics is quite different. Whereas in the $\mathrm{Ge}_{1\text{-}\mathrm{z}}\mathrm{Si}_{\mathrm{z}}$ the fraction z of Si atoms is distributed at random, in $(\mathrm{InP})_{\mathrm{y}}\mathrm{Ge}_{5\text{-}2\mathrm{y}}$ the fraction $\mathrm{z} = \frac{2\mathrm{y}}{5}$ of non-Ge atoms is not entirely random because the In and P atoms appear in pairs. Therefore, for the same value of z, the probability that a Ge atom is bonded to another Ge atom is higher in the $(\mathrm{InP})_{\mathrm{y}}\mathrm{Ge}_{5\text{-}2\mathrm{y}}$ than in $\mathrm{Ge}_{1\text{-}\mathrm{z}}\mathrm{Si}_{\mathrm{z}}$. Thus the mass term is expected to be smaller in $(\mathrm{InP})_{\mathrm{y}}\mathrm{Ge}_{5\text{-}2\mathrm{y}}$, which is exactly what is observed. Using A as an adjustable parameter, the best fit is obtained for A = 0.016, a factor of seven smaller than the $\mathrm{Ge}_{1\text{-}\mathrm{z}}\mathrm{Si}_{\mathrm{z}}$ value. The shifts predicted for this fit value are 0.51 cm^{-1} (-1.2 cm^{-1}) for the $InPGe_{15}$ ($InPGe_5$) samples. The agreement with experiment is far from perfect but can be considered acceptable in view of the partial cancellation of effects when Equations 2.2 and 2.3 are applied (which magnifies the errors) and to the compositional fluctuations observed in Figure 6, which may introduce additional shifts not included in the calculations. Further experimental and theoretical work will be needed to fully understand the vibrational properties of $(InP)_yGe_{5-2y}$ alloys, but the results so far appear consistent with the structural models consisting of bonded InP pairs in a Ge matrix.

2.3.1 Structural and Bonding Changes from Molecule to Solid

In prior CVD synthesis of $Al(P_{1-x}N_x)_ySi_{5-2y}$ and $Al(As_{1-x}N_x)_ySi_{5-2y}$ alloys via reactions of Al atoms with $M(SiH_3)_3$ (M = N, P, As) molecules (or their mixtures), it is envisioned the deliberate incorporation of molecular core structures into the solid products involves: (a) formation of intermediate "$Al{\cdot}M(SiH_3)_3$" complexes, (b) desorption of molecular hydrogen, and finally, (c) some degree of structural adjustment of the molecular core to accommodate its new bonding environment within the covalent crystalline network.[25–27] For the above Si-based systems it has been shown, using quantum chemistry and solid state simulations of the molecules and solids, that this building-block assembly process is both thermodynamically and chemically plausible.[27,28] Here the same type of simulation approach is applied to the Ge-based system, focusing for the first time on the analogous role of "$In\text{-}P\text{-}Ge_3$" cores delivered by In atom interactions with $P(GeH_3)_3$ molecules during the formation of the $(InP)_yGe_{5-2y}$ alloys, the focal point of the present study. Specifically, we use density functional theory (DFT) in the local density approximation (LDA) for exchange and correlation to simulate the ground-state energy and structure of both molecules and solids. Although more sophisticated DFT schemes might be warranted, the LDA is adopted here because its predictive ability is well-established and because it is implemented in both molecular and solid-state simulation packages, allowing meaningful structural trends to be compared within the same theoretical framework. In this regard, all molecular properties were generated by the Gaussian03 package using 6-311++G-(3df,3pd) basis sets for all atoms, except In, for which an effective core potential (ECP) was employed.[50] To simulate the properties of solids, the plane-wave basis VASP code, which eliminates the by-standing core electrons via ultrasoft pseudopotentials (ECPs) was applied.[51–53] Electronic wave functions, potentials, and densities were expanded in a plane-wave basis up to an energy cutoff of 400 eV, and reciprocal space (k-point) integration grid density was optimized to ensure convergence of atomic forces, cell stress, and energy to levels below 0.01 eV/Å, 0.1 kbar, and 0.1 meV/atom, respectively.

The main results of the molecular simulations are summarized in Figure 11, which compares the structure and nucleophilic properties of the $P(GeH_3)_3$ and $P(SiH_3)_3$ precursors as well as the molecular core structure of the hypothetical H_3In-$P(GeH_3)_3$ with the corresponding structure of the "In-P-Ge_3" building block extracted from a typical ground-state crystal environment. In growth experiments to date, the relative reactivity of the $P(SiH_3)_3$ and $P(GeH_3)_3$ precursors is found to be quite similar, suggesting the propensity of these molecules to donate bonding charge in the context of the Lewis-acid-base coordination with the group-III atoms is also comparable. Here, to elucidate this tendency the total molecular electrostatic potential (ESP) is mapped onto an appropriate charge density contour to reveal electron-rich and electron-poor regions of the molecule associated with local nucleophilic and electrophilic character, respectively. The ESP maps for $P(GeH_3)_3$ and $P(SiH_3)_3$

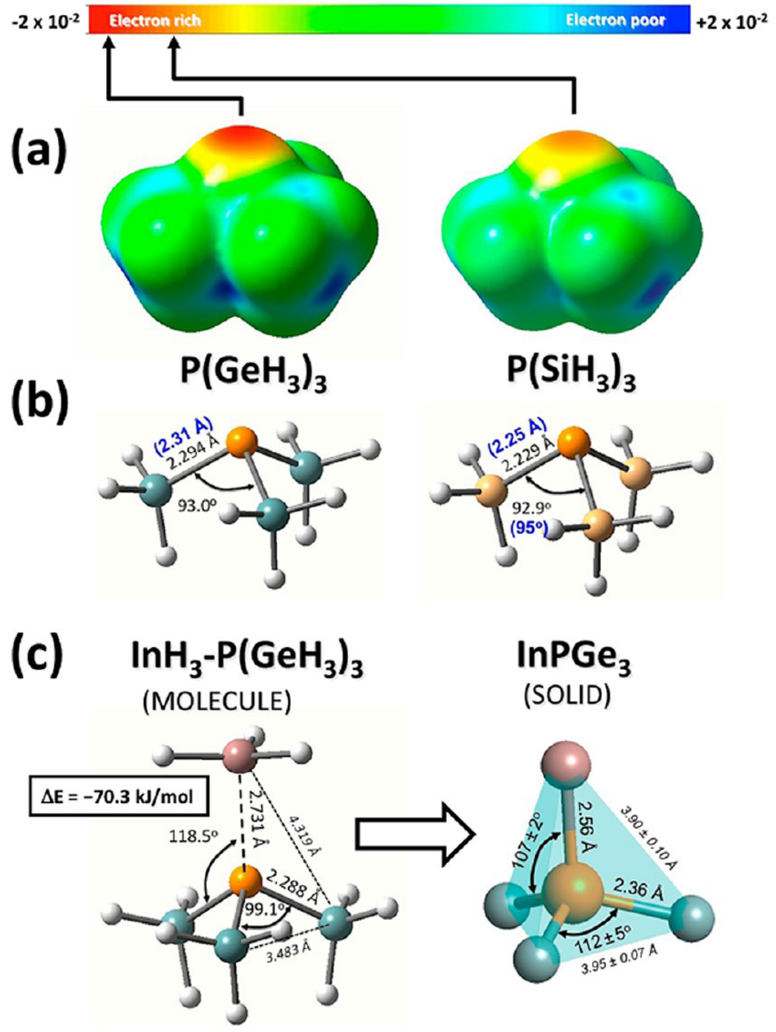

Figure 11: (a) Molecular electrostatic potentials (ESP) of the $P(GeH_3)_3$ and $P(SiH_3)_3$ molecules mapped onto their respective $\rho = 0.0005$ isodensity surfaces, showing a slightly enhanced nucleophilic character (red shaded) above the P atoms in the $P(GeH_3)_3$ compound. (b) Equilibrium structures of $P(GeH_3)_3$ and $P(SiH_3)_3$, showing good agreement between calculated and experimental (in parenthesis) bond lengths and angles. (c) Structure of the hypothetical $H_3In\text{-}P(SiH_3)_3$ adduct indicating slight P-Ge bond length contraction and $\angle$Ge-P-Ge bond angle opening in the "In-PGe_3" core (see text), resulting in a distorted tetrahedral structure. The corresponding "In-P-Ge_3" units within the equilibrium crystal structure (bottom right) show the molecular core is "regularized", exhibiting close to tetrahedral angles, edge lengths, and significantly reduced bond length variance.

molecules, shown in Figure 11(a), corroborate the similar reactivity observed for these two molecules and indicate a slightly enhanced nucleophilic character (red shade) above the P atoms for the $P(GeH_3)_3$ compound. This similarity in chemical behavior likely originates from the very similar ground-state structures of $P(GeH_3)_3$ and $P(SiH_3)_3$ molecules which both consist of symmetrically canted germyl/silyl groups with downward pointing apical hydrogen atoms, as shown in Figure 11(b). In both cases, the calculated DFT-LDA bond lengths and angles are in reasonable agreement with available experimental values (in parentheses) obtained from gas electron studies.[54] As to the relative strength of acid-base interactions in the context of $P(GeH_3)_3$ "building blocks", previously estimated the heats of reaction for the related hypothetical Si-based $H_3Al\text{-}M(SiH_3)_3$ adducts are found to be in the range of -84 to -96 kj/mol by combining the enthalpy corrected electronic energies (at 298K) for the AlH_3 and $M(SiH_3)_3$ units and subtracting these from the corresponding values for the adducts.[28] As shown in Figure 11(c), the binding energy for the $H_3In\text{-}P(GeH_3)_3$ molecule is about -70 kj/mol, which is only slightly weaker than the typical values for the Si-based analogues, indicating that the formation of "$In{\cdot}P(GeH_3)_3$" intermediates and the subsequent incorporation of "$In\text{-}P\text{-}Ge_3$" cores into the solid is certainly plausible. The bottom panel of Figure 11 also summarizes the key bond lengths and bond angles of the hypothetical $H_3In\text{-}P(GeH_3)_3$ compound. These are found to exhibit systematic changes relative to the parent $P(GeH_3)_3$ molecule very similar to those reported in prior studies for the analogous $H_3Al\text{-}P(SiH_3)_3$ molecule in relation to its $P(SiH_3)_3$ parent. For example, here the dative bonding induces a contraction of <0.01 Å in the P-Ge bond lengths ($\sim$2.29 Å) and $\sim 6^\circ$ opening of the pyramidal ($\angle$Ge-P-Ge $\sim 99^\circ$). Meanwhile, the In-P bond length and $\angle$Ge-P-In bond angle are calculated to be 2.73 Å and $\sim 119^\circ$, respectively, resulting in a significant departure from tetrahedral symmetry. This distortion leads to very dissimilar tetrahedral edge lengths, as indicated by dashed lines in the structure, corresponding to Ge-Ge (3.48 Å) and Ge-In (4.32 Å) distances.

To elucidate the nature and degree of "accommodation" required for the incorporation of the "In-P-Ge_3" tetrahedron extracted from the equilibrium crystalline structure, details of the solid state calculations are presented below. As can be seen by comparing the structure in the left and right panels (molecule, and solid respectively), the core solid structure becomes substantially regularized when linked within its crystalline network. For instance, the In-P bond length in the adduct structure is shortened to 2.56 Å, very close to the corresponding LDA bond length of 2.52 Å in the binary InP compound, while the P-Ge bond length dilates by 0.07 Å to a value of 2.36 Å. Furthermore, the internal bond angles approach the tetrahedral range such that $\angle$Ge-P-Ge $\sim 112.0 \pm 0.5°$ and $\angle$Ge-P-In $\sim 107 \pm 2°$. Collectively, these bond length and bond angle adjustments lead to a dramatic regularization on the tetrahedral edge lengths which now span a range of 3.93 ± 0.10Å, thereby facilitating the assembly of a tetrahedral framework. Similar comparisons for the $AlPSi_3$ and $AlAsSi_3$ systems also predict more regularized tetrahedral structures, consistent with experimental observation based on XRD, XTEM, and Raman scattering analyses.[25,27,28] On the basis of the deviations from perfect tetrahedral geometry of the "In-P-Ge_3" building-block structure in the crystalline habit predicted in Figure 11(c), one might anticipate similar departures from the extended diamond-cubic form, as discussed below.

An intriguing aspect of the $(InP)_yGe_{5-2y}$ alloy formation mechanism is that the concentration of In-P pairs can be systematically depleted relative to the limiting $InPGe_3$ composition via unimolecular $P(GeH_3)_3$ decomposition reactions at higher temperatures. These produce highly reactive germylene-like moieties

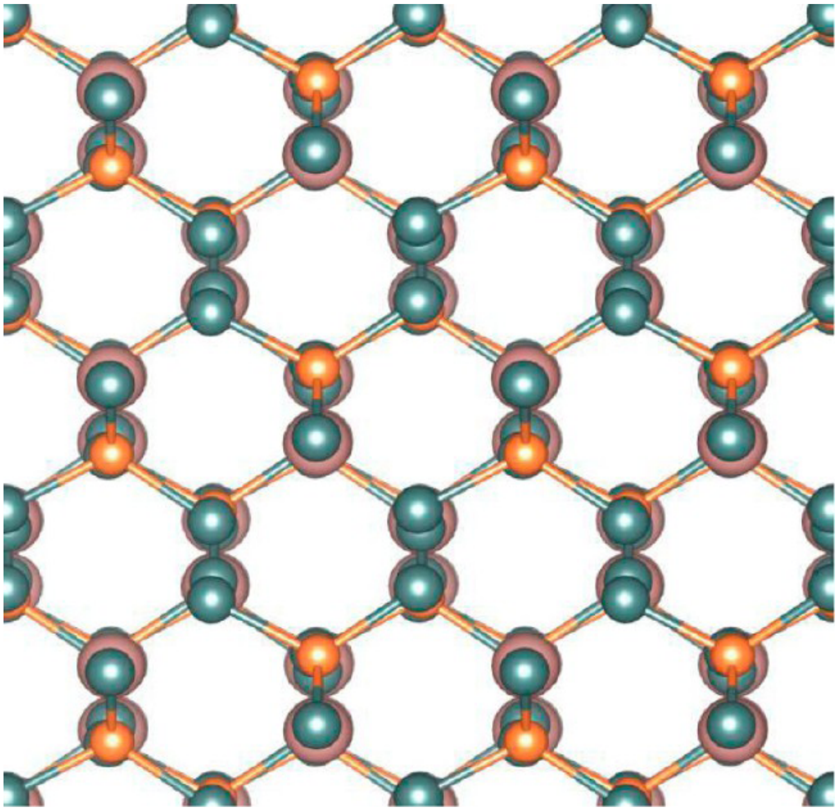

Figure 12: View of the optimized $InPGe_3$ crystal structure along the crystallographic [110] direction indicating slight deviations from perfect diamond symmetry as evidenced by misalignment of the "dumbbell" pairs (In, P, and Ge atoms are shown in pink, orange, and green spheres, respectively.

which in turn enrich the Ge content of the solid product. The net result is the formation of a crystal consistent of In-P pairs completely isolated from one another, and in the limiting $InPGe_3$ case, the P atoms reside on a third-nearest neighbor sublattice in a manner precluding the formation of energetically unfavorable In-In bonds. The lattice vectors of the primitive $InPGe_3$ cell containing two formula units are $\vec{a}_1 = a_0(\text{-}\frac{1}{2},1,\text{-}\frac{1}{2}),\vec{a}_2 = a_0(\text{-}\frac{1}{2},1,\frac{1}{2}),\vec{a}_3 = a_0(\text{-}\frac{3}{2},\text{-}\frac{1}{2},0)$, where a_0 represents the crystallographic lattice constant of a conventional cubic diamond crystal and the Cartesian components are aligned with the conventional cubic (100), (010), and (001) directions in the parent diamond cubic lattice. For instance the [001] projection is obtained from $\vec{a}_2$ - $\vec{a}_1$ = a_0(0,0,1). The In, P, and Ge atoms are initially placed on a perfect diamond lattice using fractional coordinates provided in Grzybowski et al.[27] Structural optimization then yields a static lattice ground-state structure possessing C1c1 symmetry with cell parameters $a = b = 6.971$ Å, $c = 8.932$ Å, $\alpha = \beta = 130°$, and $\gamma = 48.73°$ and atomic positions In(0.015,0.791,0.099), P(0.548,0.850,0.789), Ge(0.600,0.417,0.507), Ge(0.411,0.178,0.690), and Ge(0.260,0.951,0.907). This unit cell possesses a nearly cubic symmetry as can be seen from the [110] projection shown in Figure 12, which also illustrates the slight departures from perfect diamond cubic symmetry in which the In, P, and Ge atoms are not precisely aligned. Although the foregoing ground-state results were obtained using the primitive 10-atom setting, a more general 20-atom representation containing four $InPGe_3$ units can be used to identify higher energy metastable configurations containing various alternative "In-P" dimer orientations devoid of In-In nearest neighbor bonds. Using the notation $\{V_1', V_1'', V_1''', V_1''''\}$ established in prior work, the ground-state $InPGe_3$ structure described above corresponds to configuration {1,1,1,1} while configurations {1,4,3,2} and {1,2,1,4} with energies +22.6 and +24.0 meV/atom above the ground-state (respectively) are found to possess slightly expanded molar volumes of +0.16 and +0.33%.[27] Accordingly, the existence of slightly metastable configurations containing orientationally disordered "In-P" dimers may also be thermodynamically plausible and can lead to composition-independent molar volume fluctuations.

To further elucidate the experimental studies over the broader composition range of the synthesized alloys ($InPGe_{15}$ to $InPGe_{4.6}$), a series of supercells were constructed containing up to 20 atoms and substituted the requisite number of In-P pairs by Ge atoms to yield systems with composition $InPGe_{18}$ and $InPGe_8$. To eliminate scaling artifacts the same supercell structures were used to calculate the corresponding ground-state properties of Ge (cubic-diamond) and binary InP (zincblende) end-members. The main simulation results for the solid $(InP)_yGe_{5-2y}$ systems are summarized in Table 1 and Figure 13, where they are compared with the corresponding experimental systems for which relaxed lattice constants have been determined from XRD measurements. The data listed in Table 1 includes the static lattice ground-state energy per atom (E_0) showing the expected trend of decreasing binding energy from Ge to InP. The energy ΔE is an approximation to the formation enthalpy of a given compound relative to Ge and InP and is obtained as the difference between the $(InP)_yGe_{5-2y}$ alloy energy and that of the corresponding stoichiometric sum of InP and Ge end-members. The positive values for ΔE indicate that all systems are metastable relative to the binary InP alloy and Ge. The effective cubic LDA lattice parameters, listed as $\langle a_0 \rangle$ in the table, were obtained from the diamond-like optimized structures by $(8\Omega_0)^{1/3}$, where Ω_0 is the volume per atom of a given system. These lattice constants were then corrected to account for the typical underestimate obtained

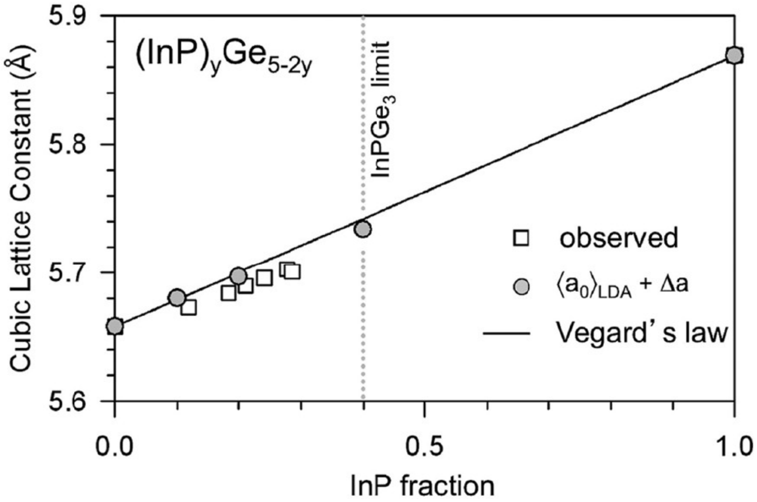

Figure 13: Plot of the corrected LDA and observed lattice constants as a function of InP content showing a close correspondence with Vegard's law (solid line). The vertical dotted line indicates the maximum 40% InP composition possible via incorporation of intact "In-P-Ge_3" units.

from the LDA by including a composition-dependent linear correction Δa varying from 0.6 to 0.7% of $\langle a_0 \rangle$ in going from Ge to InP. This allows a straightforward comparison of experimental and theoretical trends with respect to Vegard's law, as shown by the plot in Figure 13 where the agreement between the observed and the predicted data is seen to be very good. Note a slight negative bowing behavior away from ideal Vegard behavior is both observed and predicted on the basis of LDA calculations.

Table 1: Summary of LDA Calculations for $(InP)_yGe_{5\text{-}2y}$ Alloys Including Static Lattice Energies Relative to the Ge and InP End-Members, Equivalent Cubic Lattice Parameters $\langle a_0 \rangle$, Corrected LDA Values (See Text), and Experimental a_0 Values Determined by XRD

System	E_0/atom (eV)	ΔE/atom (meV)	$\langle a_0 \rangle_{LDA}$ Å	$\langle a_0 \rangle_{LDA} + \Delta a$ Å	$a_{0,EXP}$ Å
Ge	-5.1997	0	5.265	5.658	5.658
$InPGe_{18}$	-5.1329	33	5.646	5.680	
$InPGe_{15}$					5.673
$InPGe_{8.9}$					5.684
$InPGe_8$	-5.0769	56	5.662	5.697	
$InPGe_{7.5}$					5.690
$InPGe_{6.3}$					5.696
$InPGe_{5.2}$					5.703
$InPGe_5$					5.701
$InPGe_{4.6}$					5.699
$InPGe_3$	-4.9776	88	5.698	5.734	
InP	-4.8638	0	5.828	5.869	5.869

Finally, the electronic structure of the full stoichiometric $InPGe_3$ alloy was investigated within the LDA framework. Routine band structure calculations of the InP and Ge end-members using this level of theory and primitive cells containing only two atoms (zincblende and diamond structures, respectively), yield a direct gap of 0.56 eV for InP and a vanishing fundamental gap in Ge. The severe underestimation of band gaps, and the closure of the fundamental gap in Ge, are well-known failures of

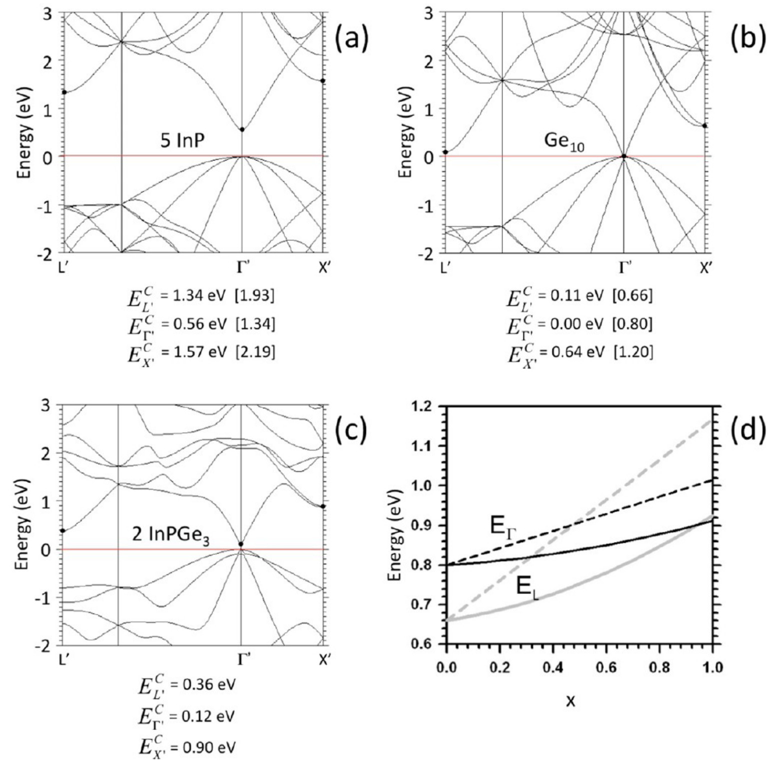

Figure 14: (a-c) LDA band structure plots of InP, Ge, and $InPGe_3$ respectively, using a common 10-atom representation (see text). Critical points are indicated by solid dots and the corresponding numerical values are listed below each panel (experimental values are in square brackets) and indicate a marginally direct gap in $InPGe_3$ at this level of theory. (d) Composition dependence of the Γ and L point energy gaps obtained by linearly interpolating between experimental values (dashed lines) and by indicating a bowing correction deduced from the LDA band structure (solid lines).

the LDA. Nevertheless, the compositional trends of the critical points corresponding to key transitions between the valence and conduction band (energy differences) in alloy systems are often quantitative. Here this approach is applied, with its inherent limitations, to the calculation of band structures of InP, $InPGe_3$, and Ge by adopting the common 10-atom representation for all three systems. This allows a direct comparison of the critical point energies. Use of lattice vectors whose Cartesian components are aligned with the conventional diamond lattice plane simplifies the interpretation of the band structure as shown in Figure 14, which illustrates the composition dependence of the energy bands in the salient portion of the gap region. The k-points L′, Γ′, and X′ in the 10-atom representation correspond to the conventional L, Γ, and X points in the FCC lattice (additional valence and conduction band states at L′, Γ′, and X′ are due to Brillouin zone folding). The calculated values of the critical point energies in the $InPGe_3$ alloy are slightly lower than the Vegard average, indicating negative compositional bowing. From the LDA critical point energies contained in the figure, bowing parameters b_{L} = -1.008 eV, b_{Γ} = -0.433 eV, and b_{X} = -0.467 eV are obtained. As discussed earlier in connection with PL measurements on $(InP)_yGe_{5-2y}$ alloys, a linear compositional interpolation between the (InP and Ge) end-members predicts an indirect-to-direct crossover near y ∼ 0.5 and a corresponding direct gap of ∼0.9 eV. However, incorporation of the calculated LDA-derived bowing parameters shifts this crossover to y ∼ 0.95, leading to a direct gap of ∼0.91 eV in $InPGe_3$ (note that the use of E_L[InP] = 1.88 eV in place of the value 1.93 eV listed in Figure 14 lead to a slight shift of the indirect-direct crossover to y ∼ 1). Future work, will re-examine the band structure of this class of alloys with a focus on indirect-direct behavior using more quantitative methods such as the GW approximation.

2.4 Conclusions

This study, demonstrated, for the first time, the synthesis of a class of monocrystalline $(InP)_yGe_{5-2y}$ alloys on Ge/Si(100), with InP content between 10 and 30% using an approach previously developed to successfully fabricate analogous $Si_{5-2y}(AlX)_y$ {X = N, P, As} semiconductors directly on Si(100). Structural characterization of the $(InP)_yGe_{5-2y}$ materials indicate they possess composition-dependent variation in lattice constants, while PL studies indicate a concomitant variation in band gap behaviour and possible direct gap values below that of Ge (0.80 eV) in the near IR. Density functional theory simulation at both the molecular and solid-state level were used to elucidate the assembly pathway, from precursor interactions, to formation of intermediate building-block structures, to the solid product and indicate the overall process is thermodynamically favorable. The observed dependence of the $(InP)_yGe_{5-2y}$ lattice constants on InP contents is closely reproduced by first principles simulations, and the corresponding Raman spectra are consistent with the "In-P-Ge_3" building-block interpretation of the crystal structure. Collectively, this and prior work provides further compelling evidence for the generality of a building-block approach to the assembly of robust, covalent crystalline solids, opening the door to a vast range of hitherto inaccessible III-V-IV solid compositions with potentially useful technological applications.

This Page Intentionally Blank

Chapter 3

CRYSTALLINE $Al_{1-X}B_XPSi_3$ AND $Al_{1-X}B_XAsSi_3$ TETRAHEDRAL PHASES VIA REACTIONS OF $Al(BH_4)_3$ AND $M(SiH_3)_3$ (M = P, As)

Portions of this chapter were reprinted with permission from Sims, P.; Aoki, T.; Favaro, R.; Wallace, P.; White, A.; Xu, C.; Menéndez, J.; Kouvetakis, J. *Chem. Mater.* **2015**, 27, 3030-3039. Copyright 2015 American Chemical Society.[55]

Portions of this chapter were reprinted with permission from Sims, P.; Aoki, T.; Menéndez, J.; Kouvetakis, J. *Microsc. Microanal.* **2015**, S3, 1923-1924. Copyright 2015 Cambridge University Press.[56]

Synopsis

This chapter details the synthesis of hybrid alloys described by the following formula: $Al_{1-x}B_xPSi_3$. These materials were grown directly on Si(100) substrates via reactions of a highly reactive aluminum source, $Al(BH_4)_3$, and a molecular source of group-V and -IV atoms, $P(SiH_3)_3$. The reaction mechanism is expected to proceed through the formation of $H_3Al\text{-}P(SiH_3)_3$ via elimination of B_2H_6 from the $Al(BH_4)_3$. Again, the building-block approach is employed, interlinking of these tetrahedral units leads to an extended solid with bulk $AlPSi_3$ stoichiometry. However, there is a significant flux of B_2H_6 at the growth front, though this molecule has low reactivity it is nevertheless incorporated into the films, leading to the desired $Al_{1-x}B_xPSi_3$ alloys.

The use of $Al(BH_4)_3$ in the place of Al atomic beams was explored with three major objectives in mind. The parent $AlPSi_3$ phase has a lattice dimension slightly larger than that of Si, through the incorporation of small amounts of B, in place of Al, full lattice matching to Si can be attained. The replacement of Al with B facilitates bandgap engineering, extending the optoelectronic capabilities of Si-compatible materials. Finally, the departure from solid sources of group-III atoms and exchange for common CVD compatible chemicals is an obvious boon for development of industrial scale synthesis where high-volume, high-throughput, production is necessary.

3.1 Introduction

3.1.1 $AlPSi_3$ System

Recent theoretical and experimental work has shown the newly introduced $AlPSi_3$ alloy system represents a lattice-matched single phase material with possible applications in Si-based multijunction photovoltaics.[25,40] Previously, attempts to produce similar metastable alloys by sputtering, evaporation, or vapor-phase deposition led to inferior film quality, primarily due to phase separation issues.[23] Recently we have shown that epitaxial $AlPSi_3$ and other $Si_{5\text{-}2y}(AlP)_y$ phases can be grown directly on Si wafers using specially designed molecular routes described by Equation 3.1.[25,26]

$$P(SiH_3)_{3(g)} + Al_{(atoms)} \rightarrow \text{“Al-P(SiH}_3)_3\text{”} \rightarrow AlPSi_{3(s)} + \tfrac{9}{2}H_{2(g)} \qquad (3.1)$$

Here the $P(SiH_3)_3$ compound combines with Al atoms generated from a Knudsen cell to form "Al-$P(SiH_3)_3$" intermediates from which hydrogen is then eliminated to deliver $AlPSi_3$ building blocks to the growth front of the crystal. By design this approach yields previously unknown classes of Al-P-Si semiconductors in which Al-P pairs are embedded within a Si matrix as isolated units, preventing phase segregation

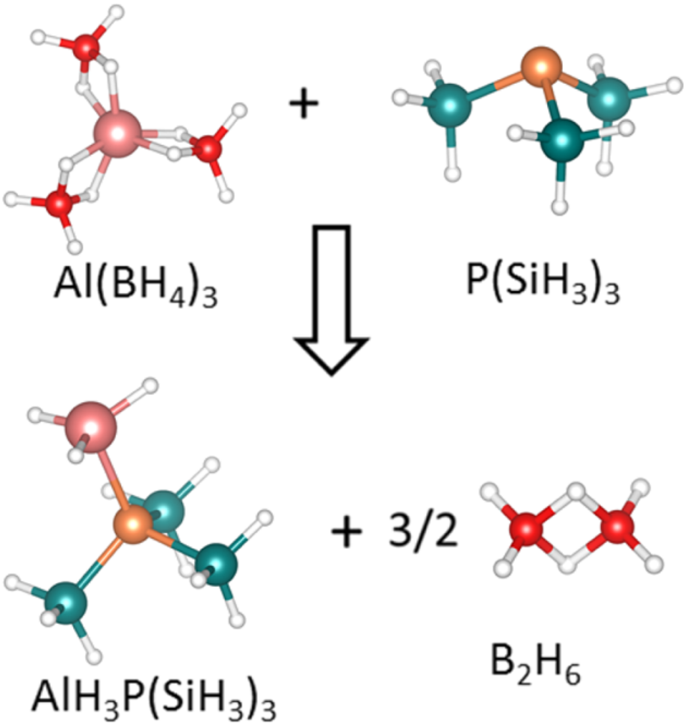

Figure 15: Idealized reaction of $Al(BH_4)_3$ with $P(SiH_3)_3$ prodcucing B_2H_6 side products and "$H_3Al\text{-}P(SiH_3)_3$" intermediate complexes containing the desired $AlPSi_3$ building unit of the Al-P-Si diamond-cubic lattice. The structures were generated using VESTA.[57]

and AlP precipitation. In terms of composition, the Al-P-Si_3 building blocks fix the stoichiometry of the film but in practice small aluminum deficiencies are commonly present, leading to large concentrations of background dopants (10^{21} atoms/cm^3) in the final product. While the bulk composition of the materials is reproducible, subtle changes in reaction conditions tend to produce variations of composition at the nanoscale whose impact on performance is not yet fully established.[58] For example, precise control of the Al flux generated from Knudsen cells is difficult to maintain and reproduce between experiments. This problem leads to the aforementioned unavoidable variation of Al content in some cases. The gas-source MBE approach employed is also not practical for large-scale, high-throughput production of thick films on large-area substrates, as required for photovoltaic applications. Both of these limitations can be substantially eliminated by replacing the atomic Al source with a molecular precursor that is chemically compatible with the $P(SiH_3)_3$ coreactant. In this case the precursor must be a volatile hydride, devoid of organic constituents, to prevent extraction of -SiH_3 groups from the building blocks as organic silanes. Aluminum hydride, AlH_3, with a dimeric structure analogous to B_2H_6 would be an ideal precursor for this application. However, the compound exists as a polymeric solid, and is therefore not suitable for CVD processing due to complete lack of volatility.[59,60] In contrast to AlH_3, the classic $Al(BH_4)_3$ is a purely inorganic (carbon-free) and stable compound that satisfies all requirements, including sufficient reactivity toward $P(SiH_3)_3$ and the necessary volatility for CVD use (150 Torr at room T).[61] This compound decomposes via elimination of B_2H_6, which does not react with $P(SiH_3)_3$ under typical growth conditions. Thus, it is envisioned the reaction between $P(SiH_3)_3$ and $Al(BH_4)_3$ could form the desired AlH_3-$P(SiH_3)_3$ intermediates provided the BH_4 units release B_2H_6 according to the reaction depicted in the schematic of Figure 15. The resultant AlH_3-$P(SiH_3)_3$ complex contains a tetrahedral $AlPSi_3$ building block terminated with H atoms (see Figure 15). These atoms desorb at the growth front as H_2 leaving behind the $AlPSi_3$ cores which interlink to produce the desired $AlPSi_3$ solid.

3.1.2 $Al_{1-x}B_xPSi_3$ System

Although it is not expected that the B_2H_6 by-product will react with $P(SiH_3)_3$ under the processing conditions (discussed in subsequent sections), its presence at the growth front may nevertheless lead to some degree of B substitution on the Al sublattice of $AlPSi_3$ to produce new $Al_{1-x}B_xPSi_3$ phases. Prior studies on $AlPSi_3$ films have also shown that small compressive strains are present in pseudomorphic layers grown on Si due to the slightly larger lattice parameters of $AlPSi_3$ (5.440 Å) relative to Si (5.431 Å).[25] This represents a 0.15% mismatch which can limit the layer thickness that can be achieved without generating unacceptable levels of strain-induced defects. Thus, any B substitution in small concentrations (3-4% relative to Al) is desirable because it could promote strain-free lattice matching of the parent structure with Si. This in an important requirement for fabrication of devices devoid of strain-related issues. The presence of boron in the lattice is also expected to influence the optoelectronic properties since the cubic BP end member is a wide-gap semiconductor. Accordingly, the incorporation of B into $AlPSi_3$ might not only provide strain relief with Si but also increase the band gap energy above the 1.3 eV value calculated for $AlPSi_3$.[40] In this regard, the new $Al_{1-x}B_xPSi_3$ alloys may be more suitable than pure $AlPSi_3$ for dual-junction solar cells, since the ideal band gap value for a cell built on top of a Si cell is 1.7 eV.[62]

This work demonstrates the growth of monocrystalline $Al_{1-x}B_xPSi_3$ layers directly on Si(100) substrates via reactions of $Al(BH_4)_3$ and $P(SiH_3)_3$ using low-pressure CVD. The samples are found to contain B atoms in the range of ~6% relative to Al. The B atoms are incorporated as isolated B-P pairs within the tetrahedral matrix as illustrated in the structural model in Figure 16.

Intriguingly, the B content remains consistent in all samples regardless of slight variations in deposition conditions. This can be explained by the fact that $Al(BH_4)_3$ serves effectively as an aluminum source only, while the BH_4 ligands are completely eliminated as B_2H_6 which represents a nonreactive leaving group. This is corroborated by control deposition experiments in which pure B_2H_6 is reacted with $P(SiH_3)_3$ under conditions identical to those employed for the $Al_{1-x}B_xPSi_3$ growth. These experiments

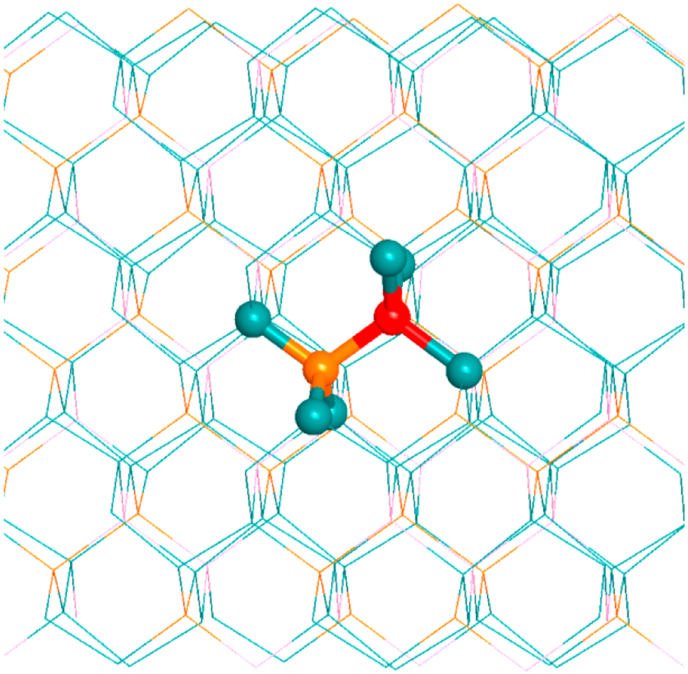

Figure 16: Ground state structure of diamond-cubic $AlPSi_3$ host lattice (lines) incorporating $BPSi_3$ tetrahedral units (spheres). The B-P moiety of the structure is represented by red-orange spheres, and the Si atoms are shown by green spheres. The lattice is drawn in a [110] projection with green, pink, and orange lines corresponding to Si, Al, and P sites, respectively.

did not generate any solid products, presumably due to the low reactivity of B_2H_6. The presence of small amounts of boron in these samples can then be explained as collateral incorporation of the atom resulting from significant quantities of B_2H_6 at the growth front. In this case B atoms preferentially bond to P or Si to yield the substitutional levels achieved in these experiments. It is speculated that the specific amount of B may in fact reflect the solubility limit of the atom in the Si-like $AlPSi_3$ matrix under the reaction conditions employed here. The presence of favorable B-P bonds slightly enhances the B incorporation relative to the amounts found in pure *p*-type commercial Si wafers. The uptake of boron is also completely in line with the levels required to compensate the misfit strain between $AlPSi_3$ and Si on the basis of

Vegard's law (assuming linear interpolation between $AlPSi_3$ and $BPSi_3$ end members). In fact, the B level slightly overcompensates relative to the amount needed for ideal lattice matching, as described later in the chapter.

3.1.3 $Al_{1-x}B_xAsSi_3$ System

The successful preparation of $Al_{1-x}B_xPSi_3$ prompted us to explore growth of the analogous $Al_{1-x}B_xAsSi_3$ phase via reactions of $Al(BH_4)_3$ with $As(SiH_3)_3$. These produced predominately $AlAsSi_3$ films doped with boron at concentrations of 10^{20} atoms/cm^3. The B uptake in this case is much smaller than the amounts incorporated in the $Al_{1-x}B_xPSi_3$, presumably due to the larger bond strains associated with substitution of B in the $AlAsSi_3$ lattice. Furthermore, the driving force for B-P bond formation in $Al_{1-x}B_xPSi_3$ is much stronger than B-As in $Al_{1-x}B_xAsSi_3$. This may be the reason why crystalline BAs films with cubic zincblende structure remain elusive in spite of significant interest due to promising applications in thermal management technologies.[63]

This chapter is organized by first discussing the growth procedures and reaction conditions to synthesize the target materials. A thorough characterization of structure, composition, and phase purity of $Al_{1-x}B_xPSi_3$ and Si deficient derivatives is then discussed including theoretical simulations of the reaction mechanism. These characterizations utilized Rutherford backscattering spectrometry (RBS), secondary ion mass spectrometry (SIMS), high-resolution X-ray diffraction (HR-XRD), high-resolution transmission electron microscopy (XTEM), atomic-scale aberration-corrected electron energy loss spectroscopy (EELS) and energy dispersive spectroscopy (EDS). Raman scattering is used to determine the local bonding arrangements and spectroscopic ellipsometry is used to obtain the dielectric function and thus elucidate the absorption behavior. Finally the $Al_{1-x}B_xAsSi_3$ growth experiments are reported and discussed, and the results are compared with the $Al_{1-x}B_xPSi_3$ system.

3.2 Experimental

3.2.1 Growth of $Al_{1-x}B_xPSi_3$

Si(100) wafers with resistivity of 1-10 Ω-cm were used as substrates in these experiments. A full wafer was cleaved into small rectangular pieces with dimensions of 1.0×1.5 cm^2 to fit onto the reactor stage. Each piece was sonicated in a 5% HF bath for ~3 minutes, rinsed with methanol, and dried using a nitrogen nozzle. They were then loaded into the chamber via a load lock at ultra-high vacuum (UHV) conditions. The samples were initially heated on the deposition stage at 650 °C by passing current through the material to remove volatile impurities from the surface. After this step the samples were flashed at 1025 °C and 1.0×10^{-8} Torr (10 times for 10 seconds each time) to desorb the native oxide and expose an epi-ready surface. Subsequently, a silicon initiation layer was grown on the substrate using mixtures of tetrasilane (Si_4H_{10}), 10% by volume in H_2. The growth was conducted at ~540 °C and $\sim1.0\times10^{-5}$ Torr for 20 minutes producing Si buffers with thickness of ~40 nm at a rate of 2 nm/minute. Immediately thereafter the epilayers were deposited on top of the initiation buffers at 535-540 °C and $8.0\text{-}10.\times10^{-6}$ Torr using mixtures of $Al(BH_4)_3$ and $P(SiH_3)_3$ in 1:2 molar ratio. These mixtures were prepared by transferring an appropriate amount of $P(SiH_3)_3$ into a 1.0 L glass bulb using a high-vacuum line. Next, gaseous aliquots of purified $Al(BH_4)_3$ were slowly added into the bulb in small increments until the desired amount was added to give the target 1:2 molar ratio of the precursor compounds. The total pressure of the mixtures was typically 1.5 Torr. The crystal growth was initiated by admitting the combined flux of the precursors into the chamber using a high-precision metering valve. The deposition times varied between 15 and 60 minutes producing films with thickness of 60-500 nm, respectively. The growth rates were very sensitive to the deposition flux and varied from 4-11 nm/minute depending on pressure from 8.0×10^{-6} to 1.0×10^{-5} Torr.

Note that very shortly after the mixture was prepared, a thin hazy film appeared on the vessel walls, indicating the formation of a solid substance, presumably a result of a side reaction between the compounds on the glass surface. This prompted an IR analysis of the gaseous content of the vessel which revealed only $P(SiH_3)_3$ and $Al(BH_4)_3$, with no sign of decomposition products, indicating this reaction is too slow at room temperature to significantly affect the bulk stoichiometry and deplete the contents of the mixture. Although the appearance of the solid residue appears to remain unchanged, it represents such a small fraction of the bulk sample that it cannot be isolated in sufficient quantities to allow characterization. One possibility is the compounds combine to form Lewis acid-base type adducts which then condense on the glass walls of the container. For example the interaction of $P(SiH_3)_3$ with $Al(BH_4)_3$ may produce short-lived $Al(BH_4)_3$-$P(SiH_3)_3$ intermediates that eliminate B_2H_6 to yield more stable $HAl(BH_4)_2$-$P(SiH_3)_3$ complexes which then adsorb onto the glass walls (Equation 3.2).

$$\mathrm{Al(BH_4)_3 + P(SiH_3)_3 \rightarrow \text{“ }HAl(BH_4)_2\text{-}P(SiH_3)_3\text{”} + \tfrac{1}{2}B_2H_6} \tag{3.2}$$

This hypothesis is supported by the known decomposition reactions of $Al(BH_4)_3$ at 70 °C producing stable dimers of $HAl(BH_4)_2$ and B_2H_6.[64] Emphasis is placed on the fact that most depositions using freshly prepared gas phase mixtures yield materials with reproducible elemental contents. The content of the bulbs was reused until depleted to produce a series of films allowing a thorough characterization of the materials properties and a detailed investigation of the reaction trends, as described later.

3.3 Results and Discussion

3.3.1 Compositional and Structural Analysis of $Al_{1-x}B_xPSi_3$

The bulk chemical compositions of all films were initially measured by RBS at 2.0 MeV using a Tandem General Ionics accelerator in the Cornell geometry. Figure 17 displays a representative spectrum illustrating distinct and well-resolved signals of the heavy Al, P, and Si atoms in the films. The spectra were fitted using the program RUMP, yielding P:Si molar ratios close to 1:3. This result implies the PSi_3 core of the precursor is likely incorporated intact into the film, as expected. The RBS fits also yield Al:P molar ratios near unity in most cases, indicating the products exhibit an average $AlPSi_3$ stoichiometry akin to that of the model lattice. The 2.0 MeV RBS spectra showed no evidence of boron, due to its low mass number and small scattering cross-section. Resonance measurements at 3.9 MeV aimed to enhance the intensity of the signal did not reveal any discernible boron peaks above the background, indicating the content is below the sensitivity limit of the technique (~5-10% of total atomic content). Indirect evidence of B incorporation was first obtained from HR-XRD measurements. The $\theta/2\theta$ plots showed (004) peaks of the cubic structure with a *d*-spacing smaller than that of Si, as expected due to significant B substitution in the

$AlPSi_3$ lattice. The B incorporation in the samples was then investigated by SIMS using a Cameca 6f instrument. Figure 18 shows the elemental profile of a representative sample, illustrating a uniform distribution of all constituent Al, B, P, and Si atoms in the layer. The plots show the signals remain constant throughout the film and then drop at the interface except for Si, whose magnitude increases from film to substrate. The concentration of B was estimated from SIMS to be ∼4% with respect to Al using reference standards of B implanted Si wafers at 1.0×10^{19} atoms/cm^3. The RBS and SIMS data collectively indicated the stoichiometry for the sample with a parent phase composition of $AlPSi_3$ can be described as $Al_{0.94}B_{0.04}PSi_3$. The B fraction determined by XRD is 6% relative to Al using Vegard's law, interpolating between $AlPSi_3$ and $BPSi_3$ end-members.

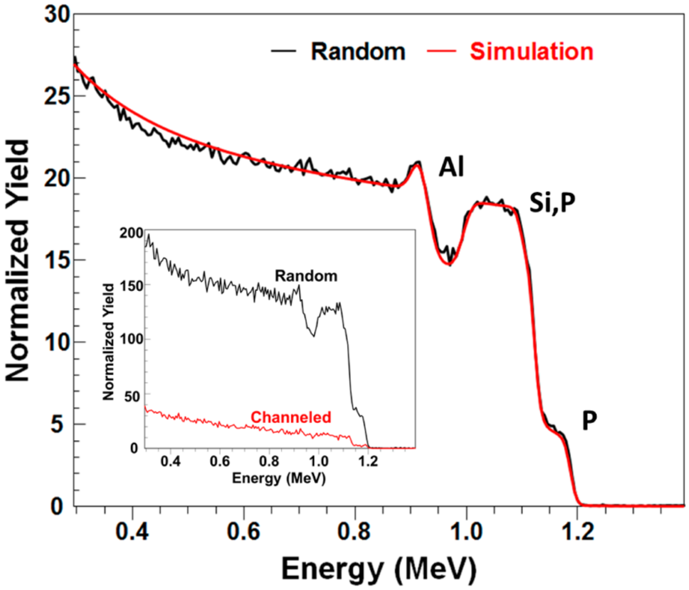

Figure 17: Random RBS (black line) showing distinct Al, P, and Si signals. Simulations using the program RUMP yield film composition $AlPSi_3$ and thickness 440 nm. Inset compares (100) aligned and random RBS spectra. The high degree of channeling as evidenced by the reduced intensity of the channeled signal (red line) indicates single crystal character of the film and epitaxial registry between the epilayer and the underlying Si-buffer

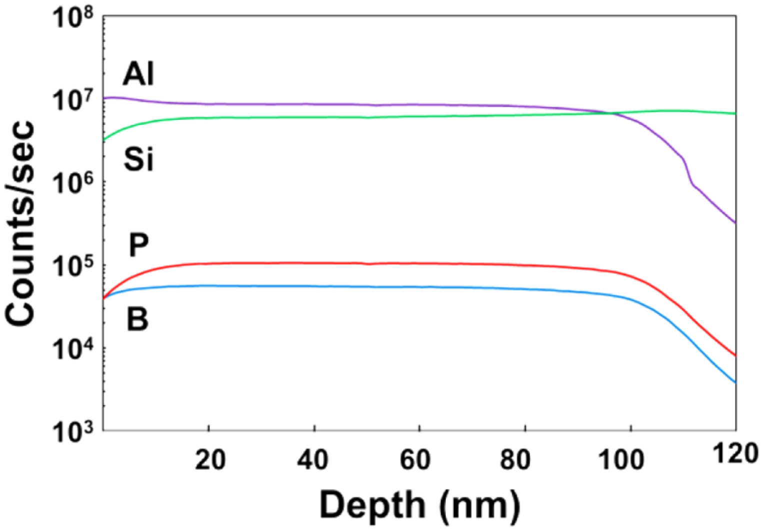

Figure 18: SIMS depth profile of a 100 nm thick $Al_{1\text{-}x}B_xPSi_3$ film grown on Si(100). The data verify the presence of B in the epilayer and demonstrate homogeneous elemental profiles of all constituent atoms in the alloy.

A series of samples were produced and analyzed following the previous procedures. The data collectively indicated the epilayers possess a narrow range of B contents between 4 and 6%. Table 2 summarizes the $Al_{1\text{-}x}B_x$ compositions as a function of growth parameters for a subset of representative samples selected among 28 thoroughly characterized prototypes exhibiting the typical structure-composition relationships described in this work. The table also displays relaxed lattice constants measured by HR-XRD showing a systematic compositional dependence as expected due to significant B incorporation.

HR-XRD using an X'Pert Panalytical diffractometer was extensively applied to establish the single phase character and also measure the lattice constants and strain states of the films.

Figure 19a shows a $2\theta/\omega$ spectrum featuring a strong and narrow peak corresponding to the (004) reflection of the Si substrate and a secondary low-intensity feature next to the Si peak assigned to the epilayer. The thickness fringes, appearing

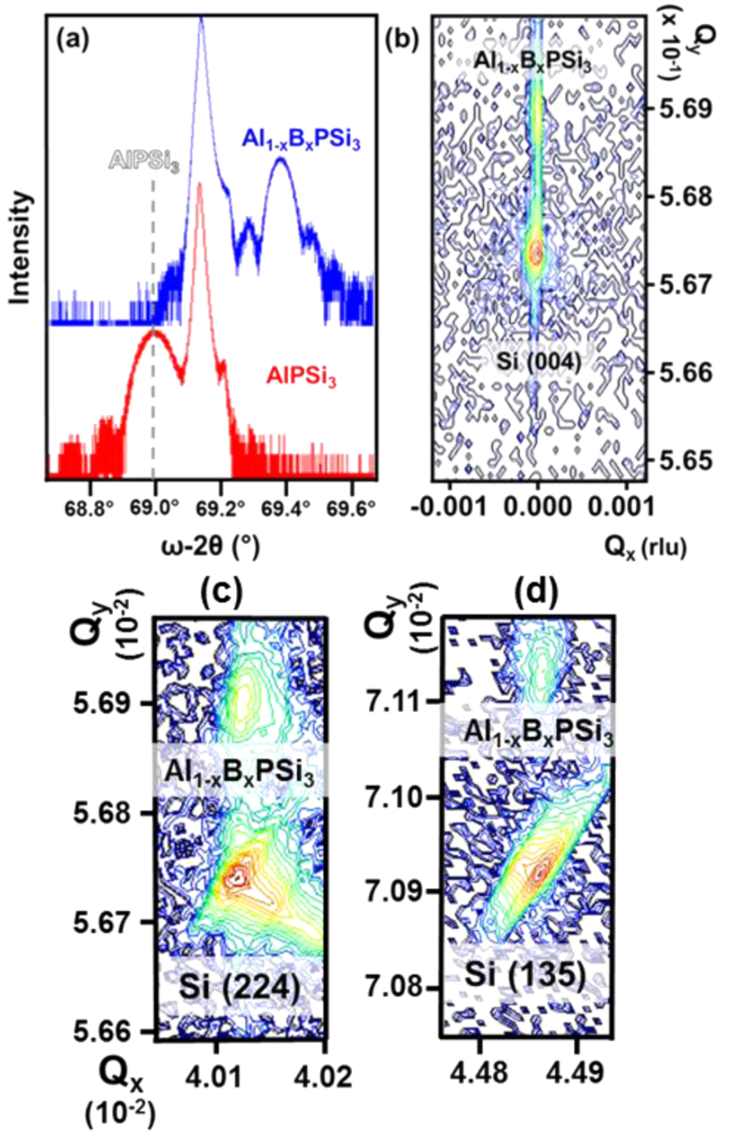

Figure 19: HR-XRD measurements of representative samples: (a) $2\theta/\omega$ plots of $Al_{1-x}B_xPSi_3$ alloy (blue trace) and pure $AlPSi_3$ reference material (red trace) showing (004) reflections of the diamond lattice for the Si (main peak) and $Al_{1-x}B_xPSi_3$ alloy (peak with thickness fringes on both sides; the latter is shifted to higher angles relative to $AlPSi_3$ due to substitution of B in Al sites). (b) (004) map indicating no apparent crystal tilt as evidenced by the vertical alignment of the film and Si peaks. (c,d) (224) and (135) maps indicating pseudomorphic growth of the epilayer on the Si substrate (same Q_x). The Q_x and Q_y values in all cases are expressed in reciprocal lattice units.

Table 2: Film Parameters (Thickness and Growth Rate) and Structure-Composition Trends (Lattice Constants vs $Al_{1-x}B_x$ Stoichiometry) for Representative Samples

a_0 (Å)	Growth Rate (nm/min)	Thickness (nm)	$Al_{1-x}B_x$ SIMS	$Al_{1-x}B_x$ XRD
5.4206	3.7	60		$Al_{0.937}B_{0.063}$
5.4217	7.3	440		$Al_{0.940}B_{0.060}$
5.4219	6.7	100	$Al_{0.963}B_{0.037}$	$Al_{0.942}B_{0.058}$
5.4221	5.7	113	$Al_{0.962}B_{0.038}$	$Al_{0.941}B_{0.059}$
5.4239	2.3	70		$Al_{0.946}B_{0.054}$
5.4245	4.7	70	$Al_{0.968}B_{0.032}$	$Al_{0.948}B_{0.052}$
5.4260	6.7	103		$Al_{0.952}B_{0.048}$
5.4304	11.2	504		$Al_{0.963}B_{0.037}$

Note: The last two columns compare XRD compositions with available SIMS data showing the B contents fall within the error of the measurement (∼2% relative to Al in the case of SIMS). In most cases the Si amount is 60% (Si_3) based on the ideal $AlPSi_3$ model

on both sides near the baseline of the alloy peak, corroborate the formation of flat surfaces and abrupt well-defined interfaces with Si. No reflections corresponding to either stoichiometric $AlPSi_3$ or Si-rich $(AlP)_xSi_{5-2x}$ derivative phases are found in the spectra. These peaks are typically located at lower angles with respect to Si in the vicinity of 69.0-69.1° as shown in Figure 19(a) displaying the (004) peak (red trace) for pure $AlPSi_3$/Si(100) whose angular position is marked by the dashed line. The (004) peak of the alloy (blue trace) has shifted to higher Bragg angle indicating the lattice constant of the film is smaller than the substrate, as expected due to the substitutional incorporation of the smaller B atoms in the place of Al in the $AlPSi_3$ lattice. No other peaks are observed in long XRD scans from 10 to 90°, providing further evidence the layer is a monocrystalline single phase material with cubic structure oriented along the [004] direction. Double crystal Ω rocking curves were taken and used to asses the crystal quality of the samples. The full width at half-maximum (FWHM) of the alloy peaks were determined to be between 97 and 115 arc-seconds which is only 3-4 times higher than that of the Si(004) peak (~37 arc-seconds). These low values indicate a high degree of crystalline ordering and suggest very low threading dislocation densities.

The lattice parameters of the samples were measured using two-dimensional reciprocal space maps (RSM) of the (224) and (135) off-axis reflections. Panels (c) and (d) of Figure 19 show corresponding contour maps in which both the film and substrate peaks are clearly visible. In each case the intensity maxima are closely aligned in the vertical direction along the pseudomorphic line indicating the lateral lattice constant (a) of the film is identical to that of the substrate. The separation of the Si/film peaks along Q_{y} indicates the crystal is tensile strained to the underlying wafer ($c_{\perp} < a_{\parallel}$) and undergoes a slight tetragonal distortion from cubic symmetry. The relaxed cubic parameter was determined to be $a_0 = 5.4217$ Å from linear elasticity theory and the measured $a = 5.430$ Å and $c = 5.4154$ Å lattice constants using the (224) plots. These values are nearly identical to those measured using the (135) plots ($a_0 = 5.4219$ Å, $a = 5.4295$ Å, and $c = 5.4154$ Å) and within the error of the technique (±0.0003 Å), as expected. To investigate the possibility of crystal tilt, (004) reciprocal space maps were also collected. A representative plot is shown in Figure 19(b) illustrating vertical alignment of the peak maxima along Q_{x} precluding any significant tilt generation between the epilayer and the Si wafer. Collectively, these results support the interpretation that the material is tetragonally strained and possesses an average diamond-like structure.

As shown in Table 2, the relaxed cubic parameter of representative samples fall within a narrow range of 5.4206-5.4304 Å, depending on the amount of B substitution. These (a_0) values are intermediate to zincblende $\mathrm{Al_{1\text{-}x}B_xP}$ and Si. However, on the basis of the XRD analysis alone, the possibility of phase separation to $Al_{1-x}B_xP$ and Si end-members with similar XRD parameters cannot be entirely ruled out. This is because the diffraction peaks of pure Si in the sample would overlap with the dominant (004) peak of the substrate. To investigate this possibility, the Si substrate background was removed from the XRD plots completely by substituting GaP wafers. This platform was selected as a suitable alternative because its lattice parameter ($a = 5.451$ Å) is marginally larger than Si ($a = 5.431$ Å), and thus its Bragg reflections appear at slightly lower angles relative to Si. Furthermore, the drawback of a larger a is not significant enough to hinder epitaxial integration of the target alloys thus making GaP an ideal platform for this investigation. The depositions on GaP produced fully coherent monocrystalline films with composition $Al_{0.94}B_{0.06}PSi_3$ with a relaxed cubic parameter $a_0 = 5.4203$ Å. No peaks associated with pure Si or $Al_{1-x}B_xP$ components were observed in the XRD spectra, thus providing strong evidence that the material is a single phase alloy. Furthermore, Raman scattering demonstrated the incorporation of B occurs in the form of randomly distributed B-P pairs embedded as isolated units into the diamond Si matrix. This also proves the presence of a single phase and precludes the possibility of zincblende $Al_{1-x}B_xP$ segregation having occurred, as described in detail later. Finally, note the last row of Table 2 which describes a $Al_{1-x}B_xPSi_3$ sample with x = 3.7, exhibiting $a_0 = 4.53$ Å identical to that of Si. The film is deposited at a high growth rate (∼11 nm/min) and with large thickness (∼500 nm) devoid of lattice distortions and misfit strains. The fact that the material lattice-matches Si validates the feasibility of the $Al(BH_4)_3$ strategy for the production of $Al_{1-x}B_xPSi_3$ layers suitable for possible applications in Si-based PV devices.

Collectively the preceding SIMS, XRD, and RBS results listed in Table 2 demonstrate that $Al(BH_4)_3$ depostions produce stoichiometric (Si_3) alloys with reproducible compositions in which the P content and the combined Al_{1-x} and B_x fractions are 1:1. The reliability afforded by the new process represents a significant improvement over the previous MBE method in which difficulties in controlling the Al flux caused Al variations and unintentional autodoping. Furthermore, the MBE method required a narrow range of temperatures and pressures in order to reproduce the target Al-P-Si samples, making the process tedious.

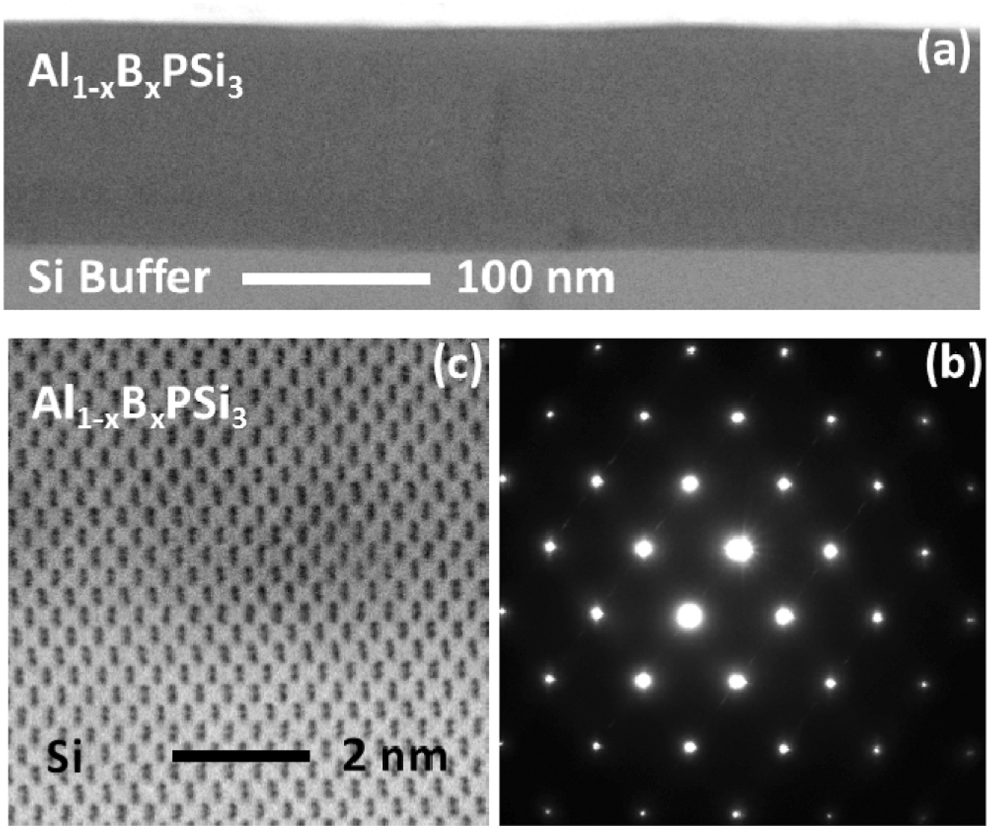

Figure 20: XTEM micrographs taken from a representative $Al_{1-x}B_xPSi_3$/Si(100) sample. Panel (a) shows a diffraction contrast image of a full epilayer revealing a planar surface and uniform thickness throughout. Panel (b) is an electron diffraction pattern showing the Si-like symmetry in [110] projection. Panel (c) is a high-resolution image of the interface region illustrating full coherence of the {111} lattice planes of the film and substrate.

Further characterization of the film structure, crystallinity, and epitaxial quality were performed by RBS channeling and XTEM. The channeled spectrum for a typical sample is shown inset in Figure 17. The ratio of the channeled vs the random peak heights for Al, P, and Si is found to be nearly equal in a given sample, indicating all atoms occupy substitutional sites in the same tetrahedral lattice. Furthermore, the film and the substrate channel at the same angle indicating that the material is single crystal and epitaxially matched to the substrate. The XTEM micrographs revealed uniform monocrystalline layers with planar surfaces and thicknesses of 55-500 nm which are comparable to those determined by RBS. The bulk layer microstructure revealed intermittent threading dislocations and stacking defects with no obvious sign of phase separation as illustrated by the micrograph in Figure 20(a). Electron nanodiffraction was applied to study the local structure using a JEOL ARM 200F microscope operated at 200 kV. Figure 20(b) shows a representative pattern in [110] projection taken from an 80 nm diameter region of the epilayer, illustrating a diamond-like symmetry akin to Si, as expected on the basis of previously reported structural models of $AlPSi_3$. Several spots along specific directions appeared to be broadened and slightly elongated, presumably due to the presence of defects scattered over isolated sections of the bulk crystal. Aberration corrected images of the interface region shown in Figure 20(c) revealed a 1:1 correspondence of the Si {111} lattice planes with those of the epilayer, as expected due to the similarity in crystal structure and lattice spacing between the two materials.

Additional characterizations of the elemental distribution were performed using atomic-scale EELS and EDS with nanometer sized probes. EELS detected significant amounts of boron, but the close overlap of the B K-edge with the Si L-edge prevented the quantification of the concentration. EELS nevertheless shows strong and distinct peaks corresponding to K-edges of the heavy Al, P, and Si atoms at 1560, 2153, and

1839 eV respectively. Quantitative analysis yielded virtually stoichiometric $AlPSi_3$ compositions consistent with the bulk values measured by RBS. The EELS analysis was further corroborated by EDS using the same JEOL ARM 200F microscope. The spectra in this case showed K-α peaks for Al, P, and Si which were fitted to yield atomic concentrations of 20%, 19%, and 61%, respectively, as expected for $AlPSi_3$. EDS line scans revealed uniform atomic profiles across the layers and abrupt transitions at the interfaces with Si, corroborating the SIMS results discussed previously. Finally the layer morphology was examined by Nomarski imaging showing flat and smooth surfaces devoid of large-scale flaws such as cracks, pores, or impurity precipitates. Collectively the morphology, microsctructure, and nanoanalysis results demonstrated high crystal quality films amenable to a thorough characterization and unambiguous evaluation of their properties. The results support the notion that the crystal assembly proceeds via direct single-channel reactions of gas phase molecules and any secondary dissociation reactions of the co-reactants that could give rise to amorphous impurities do not seem to play a role in this process. The crystal growth is further facilitated by the close lattice matching and chemical compatibility between the films and the Si platform.

3.3.2 Atomic Scale Structure and Bonding Configurations of $Al_{1-x}B_xPSi_3$ Determined via Atomic-Resolution STEM-EELS

The structural and compositional homogeneity of $Al_{1-x}B_xPSi_3$ was further investigated using atomic-resolution electron energy loss spectroscopy (EELS). This analysis was done to eliminate any concerns over phase separation into Si and zincblende $Al_{1-x}B_xP$ domains. EELS mapping was performed using a Nion UltraSTEM

100 equipped with HERMES^{TM} and Gatan Enfinium^{TM} EELS spectrometer. This instrumental configuration allows for simultaneous high-resolution imaging and compositional mapping using STEM and EELS using probe sizes comparable to the atomic spacing. The bonding patterns and constituent atoms are identified yielding the alloy composition and structure at the ångström level. Figure 21(a) shows a low magnification micrograph of the entire $Al_{1-x}B_xPSi_3$ film grown on Si-buffered Si(100). The image reveals a planar surface and uniform contrast throughout, indicating a homogeneous material with uniform microstructure. As stated previously the use of an initiation layer is to ensure the material growth is conducted on a clean epiready surface. This micrograph illustrates the effectiveness of this approach, note the defects observed in this field of view are confined to the Si-initiation layer/Si(100) interface allowing for near perfect epitaxial commensuration. STEM-EELS experiments were conducted in [110] projection, the EELS maps were collected from the area shown in Figure 21(b) which was collected in tandem with the EELS spectral maps. Panels (c-e) are fitted EELS maps corresponding to the K-edges of Al, P, and Si; panel (f) is an overlay of all three maps showing the uniform distribution of all three elements on the diamond-like lattice. Figure 21(g) shows a structural model of the parent $AlPSi_3$ lattice in the same projection, showing the close correspondence between experiment and theory.

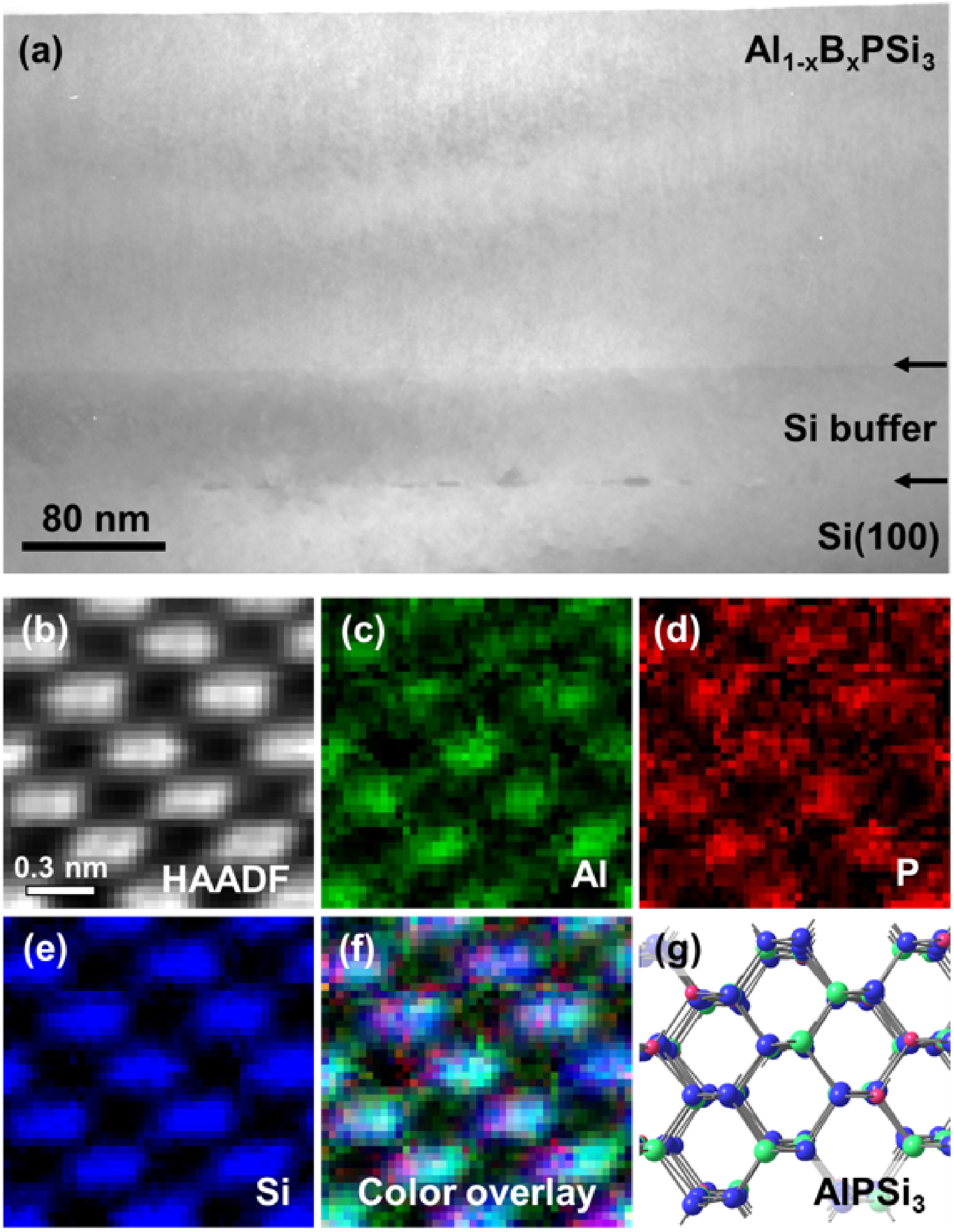

Figure 21: XTEM micrograph and multiple linear least squares fitted STEM EELS mapping of $Al_{1-x}B_xPSi_3/Si(100)$; (a) Low-magnification XTEM micrograph of the entire Al1-xBxPSi3 layer and Si buffer showing uniform contrast indicating the layer is a single-phase monocrystalline material; (b) HAADF reference image; (c) Al K-edge map; (d) P K-edge map; (e) Si K-edge map; (f) Color Overlay; (g) structural model for the $AlPSi_3$ parent structure in the same projection.

3.3.3 Si Deficient Alloy Analogues of $Al_{1-x}B_xPSi_3$

The samples listed in Table 2 contained mostly stoichiometric $Al_{1-x}B_xPSi_3$ compositions produced via intact incorporation of the PSi_3 molecular core in the structure. However, in some samples the Si:P ratio was found to be lower than 3:1 ranging from 2.8:1 to 2.5:1 irrespective of the reaction conditions. These samples exhibited a concomitant increase in lattice dimensions with decreasing Si fraction as shown in Figure 22, which compares the (004) peaks for pure $AlPSi_3$, $Al_{1-x}B_xSi_3$ and silicon deficient $Al_{1-x}B_xPSi_{2.7}$ alloys containing the same amount of boron. The alloy films are fully coherent to Si and thus possess a common in-plane lattice constant (a). The XRD peaks exhibit a strong and sharp profile allowing clear resolution of their angular position despite the close similarity in *d*-spacings. Accordingly, in spite of the minute deviation between the lattice parameters of $Al_{1-x}B_xSi_3$ and $Al_{1-x}B_xSi_{2.7}$, a measurable increase of the vertical (c) lattice constant is found as the amount of Si is reduced from 3 to 2.7. The observed Si deficiencies are significant from the point of view of influencing the material fundamental properties. For example, lowering the amount of Si should increase the band gap relative to $Al_{1-x}B_xSi_3$. This outcome should be beneficial for photovoltaic applications as discussed in section 3.1 provided the Si content does not significantly deplete to the extent that it compromises the integrity of the parent Si matrix (i.e., it does not get below $Al_{1-x}B_xPSi_2$ or 50% Si).

The preceding Si deficit may be attributed to side reactions producing $HAl(BH_4)_2$-$(SiH_3)_3$ intermediates via interaction of $P(SiH_3)_3$ with $Al(BH_4)_3$ as proposed earlier by Equation 3.2. As illustrated by the idealized reaction in Equation 3.3, these intermediates might eliminate SiH_4 side products which are then pumped away and do not participate in film growth under the low-temperature,

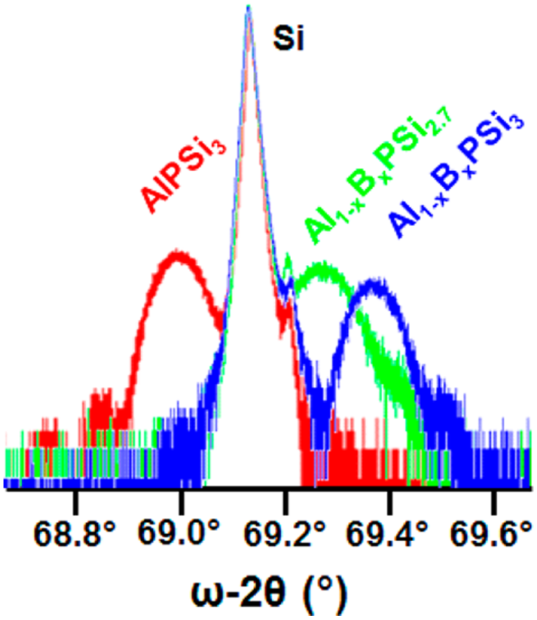

Figure 22: XRD (004) peaks of alloy samples $Al_{1\text{-}x}B_xPSi_3$ (blue) and $Al_{1\text{-}x}B_xPSi_{2.7}$ (green) are compared to pure $AlPSi_3$ (red). The peak positions indicate an increase in vertical lattice constant with decreasing Si fraction (shift to smaller Bragg angles). By adjustment of the Si and B contents in the samples, the lattice dimensions are systematically varied above and below bulk Si using this approach.

low-pressure conditions employed.

$$HAl(BH_4)_2\text{-}P(SiH_3)_3 \rightarrow (BH_4)_2Al\text{-}P(SiH_3)_2 + SiH_4 \tag{3.3}$$

In this connection note that prior work targeting $AlMe_3$-$P(SiH_3)_3$ adducts via reactions of $P(SiH_3)_3$ and $Al(Me)_3$ yielded the $(SiH_3)_2PAlMe_2$ compound as the main product via elimination of $MeSiH_3$, in analogy with the process described in Equation 3.3.[65] To further explore the likelihood of the prededing reaction mechanism, controlled experiments were performed in which equimolar amounts of pure $Al(BH_4)_3$ and $P(SiH_3)_3$ were combined at -78 °C without solvent. Although these conditions do not mimic the low-pressure molecular flow regime of the CVD experiment, it nevertheless provides fundamental insights into condensed phase reactivity of the molecules at equilibrium. A gaseous product was immediately formed under these conditions and was readily identified by infrared spectroscopy to be a mixture of B_2H_6 and SiH_4. The reaction was then allowed to warm to room temperature and proceed to completion for several hours after which the B_2H_6 and SiH_4 products were removed under vacuum leaving behind a viscous liquid. The combined volume of the gaseous species was collected and measured to be nearly equal to the sum of their stoichiometric volumes expected in accordance to the reaction pathway described by Equation 3.2 and 3.3. The IR spectrum of the viscous liquid was found to be similar to that calculated for the proposed monomeric $(BH_4)_2Al\text{-}P(SiH_3)_3$ product whose DFT calculated structure is depicted in Figure 23. The optimized ground state was generated using the Gaussian03[50] package with the B3LYP functional and 6-311G++(3df,3pd) basis set for all atoms. Thermochemistry simulations gave a slightly negative Gibbs free energy of formation (-4.20 kJ/mol) indicating the compound is stable and potentially accessible by experiment. As seen in Figure 23 the molecular structure shows significant steric crowding about the Al center imposed by the bulky BH_4 groups and the $P(SiH_3)_2$ ligand, and thus likely to be monomeric, in contrast to prototypical metal organic analogues with dimeric Al_2P_2 core structures. The calculated Al-P bond length in $(BH_4)_2Al\text{-}P(SiH_3)_2$ (2.3005 Å) is shorter than in the aforementioned dimers and in cubic AlP with zincblende structure (2.3614 Å) suggesting P atoms are likely 3-fold coordinated as a consequence of the steric hindrance. The top panel of Figure 23 illustrates a side view of the equilibrium $(BH_4)_2Al\text{-}P(SiH_3)_2$ structure showing the trigonal planar geometry of $PAlB_2$ fragment and the pseudotetrahedral (pyramidal) environment of the $\text{-}P(SiH_3)_2$ ligand. Figure 23 (bottom panel) shows a top-down projection emphasizing the planar arrangement of the Al center with bond angles ranging from 121° to 118°, as expected due to the C_s symmetry of the molecule.

The bond angles about the P atoms vary slightly from 101° to 99.9° and deviate significantly from the experimental 95° value of $P(SiH_3)_3$. This opening of the bond angles may be attributed to back-donation of electron charge from the electron-rich P atom to the electrophilic Al site. This notion is supported by molecular electrostatic potential (ESP) isodensity surfaces (not shown here) which show the nucleophilic character at P in this molecule is significantly reduced relative to $P(SiH_3)_3$.

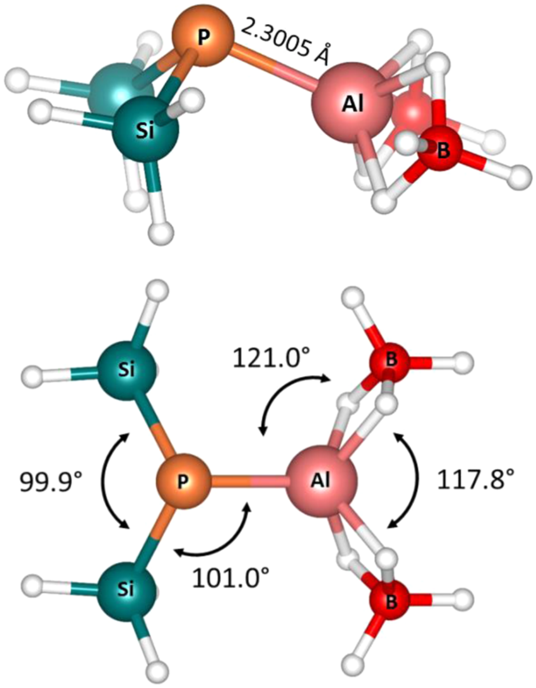

Figure 23: Equilibrium structure of $(BH_4)_2Al\text{-}P(SiH_3)_2$. The top model shows a side view of the molecule emphasizing the planar and pyramidal geometries about the Al and P centers, respectively. The bond angles corroborating these geometries are shown at the bottom orientation of the molecule. The structures here were generated using the program VESTA.[57]

The main conclusion of the preceding theoretical and experimental results is that $Al(BH_4)_3$ readily reacts with $P(SiH_3)_3$ via elimination of B_2H_6, opening a straightforward path to the production of crystalline solids containing tetrahedral aluminum and boron as required for the fabrication of Si-based semiconductors. Under the deposition conditions any unimolecular decomposition tendencies of $Al(BH_4)_3$ that might lead to amorphous aluminum borides are suppressed,[66] making the compound an authentic carbon-free source for this application. However, when mixtures of $Al(BH_4)_3$ and $P(SiH_3)_3$ are kept on the time scale of 24-48 hours prior to growth, they produce Si deficient $Al_{1-x}B_xPSi_{(2.8-2.5)}$ films presumably due to side reactions which alter the optimal gas phase concentrations of the stock mixture.

3.3.4 Bonding Properties of $Al_{1-x}B_xPSi_3$ Using Raman Scattering

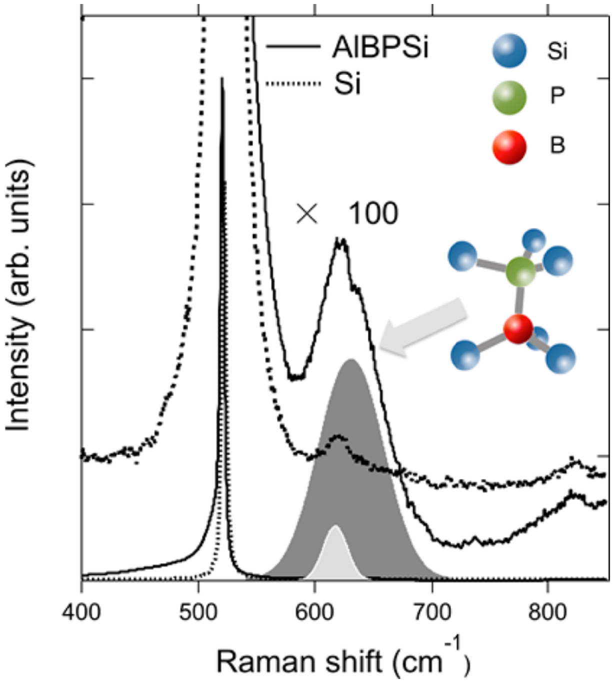

Figure 24: Raman spectrum of an $Al_{1-x}B_xPSi_3$ sample (solid lines) compared with bulk Si (dotted lines). The shaded curves correspond to a two-Gaussian fit of the spectrum in the 550-750 cm^{-1} range. The lower energy, weaker peak (light gray) is likely due to two-phonon Raman scattering. The stronger peak centered at 631 cm^{-1} (dark gray) is assigned to B-P vibrations. The peaks at 620 and 823 cm^{-1} in bulk Si are two-phonon features.

As mentioned earlier, Raman scattering was used to investigate the local bonding environment of the B atoms in the alloys. The Raman spectra were collected at room temperature using up to 10 mW of 532 nm radiation in the backscattering $z(x,y)\bar{z}$ configuration (using the standard Porto notation, where x,y, and z refer to the crystallographic cubic axes). Figure 24 shows a typical spectrum for an alloy sample and compares with measurements from a pure Si crystal. The alloy spectrum is dominated by a Si-like peak that is slightly down-shifted from the Raman frequency of pure Si, as expected. The two spectra have been normalized to the same integrated intensity of the main peaks. In the 550-850 cm^{-1} range, which is magnified 100 times, the pure Si spectrum shows two distinct peaks at 620 and 823 cm^{-1}. These peaks are consistent with published second-order Raman spectra of Si and in perfect agreement with the second-order Raman spectrum of Si predicted from ab initio calculations by Windl et al.[67,68] Accordingly, these peaks are assigned to phonon combinations. The same features appear in the Raman spectrum of the alloy sample, but in addition there is a strong feature centered at 631 cm^{-1}. This is up-shifted by about 10 cm^{-1} from the frequency of the main local mode of B in Si but is in much better agreement with the reported frequency of 628-629 cm^{-1} for the axial mode of B-P pairs in Si.[69,70] A similarly shaped peak, but centered at 650 cm^{-1}, was reported by Fujii et al. for Si nanocrystals co-doped with B and P.[71] The up-shift in frequency was interpreted in terms of B-P cluster formation, but it is worth noticing the zone center TO-LO frequencies in zincblende BP are 799 and 829 cm^{-1} respectively, thus the formation of B-P clusters should be expected to increase the frequency from the value found for isolated B-P pairs.[72] On the other hand, in these samples the B-P pairs are expected to be isolated, and therefore the peak at 631 cm^{-1} is assigned to B-P vibrations. The peak is broad (FWHM = 63 cm^{-1}), which may be due to the presence of second-neighbor

P atoms and to the mixing of the axial and perpendicular modes predicted for an isolated B-P pair in Si.[69]

The intensity of the B-P band should provide a measurement of the B concentration in the sample, but unfortunately no standards are available and the polarizability derivatives for the B-P bond remain unknown. From measurements of the local mode of C in Si, Meléndez-Lira et al. found the intensity ratio between the localized C-mode and the main Si Raman peak is 3.7 times the C concentration in the sample.[73] In this case, $I_{\text{B-P}}/I_{\text{Si-Si}} = 0.10$. Applying the same expression to the data (essentially assuming the Si-C bond is similar to the B-P bond), a B concentration of 2.7% is obtained. Since the mode eigenvector is mostly localized on the B atom, a more realistic comparison might be with the Raman intensity of the local mode of B in Si. Engstrom and Bates have reported Raman measurements of boron-implanted, laser-annealed Si samples.[74] For a sample implanted with a peak B concentration of 3.28×10^{20} atoms/cm^{-3}, they find the ratio between the local mode of B and the Si main peak is about 0.02, which implies the found ratio $I_{\text{B-P}}/I_{\text{Si-Si}} = 0.10$ corresponds to a B concentration of 3.3%, in good agreement with the previous estimate based on Si:C data. However, that the measurement of the Raman intensity of the local mode of B in Si is complicated by the fortuitous overlap of the mode frequency with the second-order feature at 620 cm^{-1}. A survey of the literature shows in many cases the assumption was made that using the $z(x,y)\bar{z}$ scattering configuration all second-order Raman scattering is suppressed. This is clearly not the case, which may lead to systematic errors in the B concentration estimates. Moreover, the strong Fano-like interferences in highly doped Si affect very strongly the intensity of the local B modes, to the extreme that for certain dopant concentrations and excitation wavelengths the Raman peaks reverse sign.[27] In spite of these uncertainties, however, the Raman data strongly support the presence of substitutional boron in amounts on the order of ∼3%. The observed frequency of this band provides strong evidence that the boron found in these samples is bonded to P.

3.3.5 Spectroscopic Ellipsometry Studies of $Al_{1\text{-}x}B_xPSi_3$ Optical Response

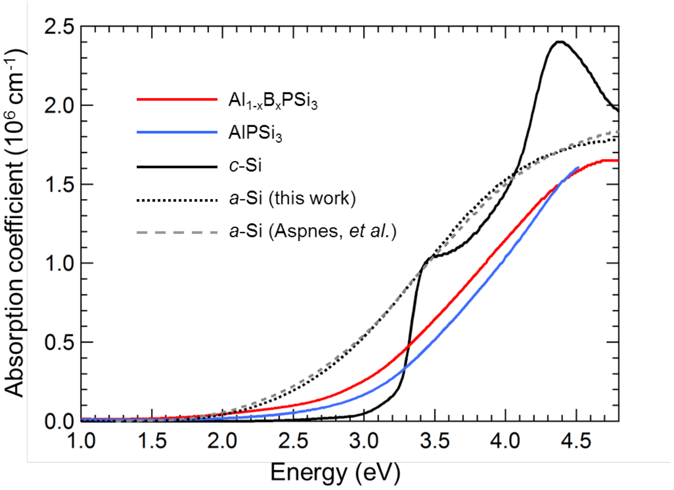

Figure 25: Comparison of absorption coefficients for crystalline c-Si, amorphous a-Si, $Al_{1\text{-}x}B_xPSi_3$, and $AlPSi_3$ (reprinted with permission from Jiang et al.[58] Copyright 2014 American Chemical Society) The a-Si sample was grown using Si_4H_{10}, and its absorption properties agree well with literature data.[75] $Al_{1\text{-}x}B_xPSi_3$ exhibits higher absorption than $AlPSi_3$ from 1.0 to 4.2 eV. Both alloys show stronger absorption than c-Si below 3.3 eV across the visible range of the spectrum

A major objective in developing $Al_{1\text{-}x}B_xPSi_3$ alloys is to study the photon absorption relative to Si and $AlPSi_3$, for potential applications in photovoltaics. For this purpose room-temperature spectroscopic ellipsometry measurements were carried out to obtain the dielectric function of the alloys. The spectra were collected using a variable-angle spectroscopic ellipsometer (VASE from J.A. Woollam Co.) over an energy range of 0.6-5.0 eV, with multiple incident angles at 65°, 70°, and 75°. Excellent fits were achieved by modeling the pseudodielectric functions of multiple samples with a four-layer model, which includes the Si substrate, an $Al_{1-x}B_xPSi_3$ bulk material layer, a thin SiO_2 oxide layer, and a surface roughness layer. The latter is modeled to have 50% voids and 50% SiO_2 in the Bruggeman approximation, with a thickness given by $2\sqrt{2}\ \sigma_{\mathrm{AFM}}$, where σ_{AFM} is the RMS roughness value from the AFM measurement. The dielectric functions of the $Al_{1-x}B_xPSi_3$ layer are fitted with two Tauc-Lorentz oscillators. The absorption coefficient of a representative sample is plotted in Figure 25 and compared to corresponding coefficients of crystalline Si and $AlPSi_3$, which have been obtained previously with similar methods.[58] The absorption of $Al_{1-x}B_xPSi_3$ is broader than $AlPSi_3$, probably reflecting the increased bond-length disorder due to the presence of B in the film. An important practical consequence of this additional broadening is a significantly enhanced absorption relative to Si and $AlPSi_3$ for $E <$ 3.3 eV. Figure 25 compares the absorption of $Al_{1-x}B_xPSi_3$ with that of an amorphous silicon (a-Si) sample grown via decomposition of tetrasilane (Si_4H_{10}) at 500 °C. This material exhibits a thickness similar to the $Al_{1-x}B_xPSi_3$ sample, and its absorption coefficient agrees very well with a-Si values found in the literature.[75] The a-Si shows a higher absorption into the visible but the crystalline nature of $Al_{1-x}B_xPSi_3$ suggests the alloy should have much longer minority recombination lifetimes, which bodes well for PV applications.

3.3.6 Growth and Analysis of $Al_{1-x}B_xAsSi_3$ Alloys

The work described previously provides a conceptual path potentially addressing the lattice matching problem of the known $AlAsSi_3$ phase with Si.[27] This material exhibits a structure analogous to $AlPSi_3$ and a cubic parameter a = 5.52 Å which is intermediate to Si ($a = 5.431$ Å) and Ge ($a = 5.657$ Å). Accordingly, substitution of Al by B is envisioned to produce $Al_{1-x}B_xAsSi_3$ alloys with lattice dimensions more compatible with Si. These materials should be obtained via reactions of $Al(BH_4)_3$ with $As(SiH_3)_3$. In contrast to $P(SiH_3)_3$, when $As(SiH_3)_3$ was combined with $Al(BH_4)_3$ in a glass container at the same 2:1 ratio there was no visible reaction between the two chemicals, neither in the gas phase nor on the container walls. In fact, mixture of $As(SiH_3)_3$ and $Al(BH_4)_3$ remained stable with no sign of any decomposition on a time scale of weeks. This is an expected outcome on the basis of prior work which indicated $As(SiH_3)_3$ is a weaker Lewis base than $P(SiH_3)_3$ and therefore does not readily combine with $Al(BH_4)_3$ at room temperature due to its lower reactivity toward nucleophilic attack.[28]

The depositions of $Al(BH_4)_3$ with $As(SiH_3)_3$ were conducted at 580 °C and 1.0×10^{-5} Torr following protocols similar to those employed for the $Al_{1-x}B_xPSi_3$ samples. SIMS was initially used to characterize the elemental content in the films, as illustrated in Figure 26 which shows flat and uniform spectral profiles for all atoms, Al, B, As, and Si. The B content was estimated in the range of $2\text{-}3\times10^{20}$ atoms/cm^3 using B-doped Si standards. The result indicates the B uptake in these samples is less than that observed in $Al_{1-x}B_xPSi_3$ analogues and reflect typical concentrations of acceptor atoms in commercial *p*-type Si wafers doped with B. The full elemental content of the samples was then corroborated by RBS which revealed an average $AlAsSi_3$ composition and also yielded film thicknesses of 70-220 nm (Figure 26, bottom). The channeled RBS spectra showed that the layers are crystalline and expitaxial with the substrate. All elements exhibited the same degree of channeling as expected for single phase materials in which all the atoms occupy substitutional lattice sites. XRD (224) reciprocal space maps and (004) on-axis reflections revealed significant compressive strains due to the difference

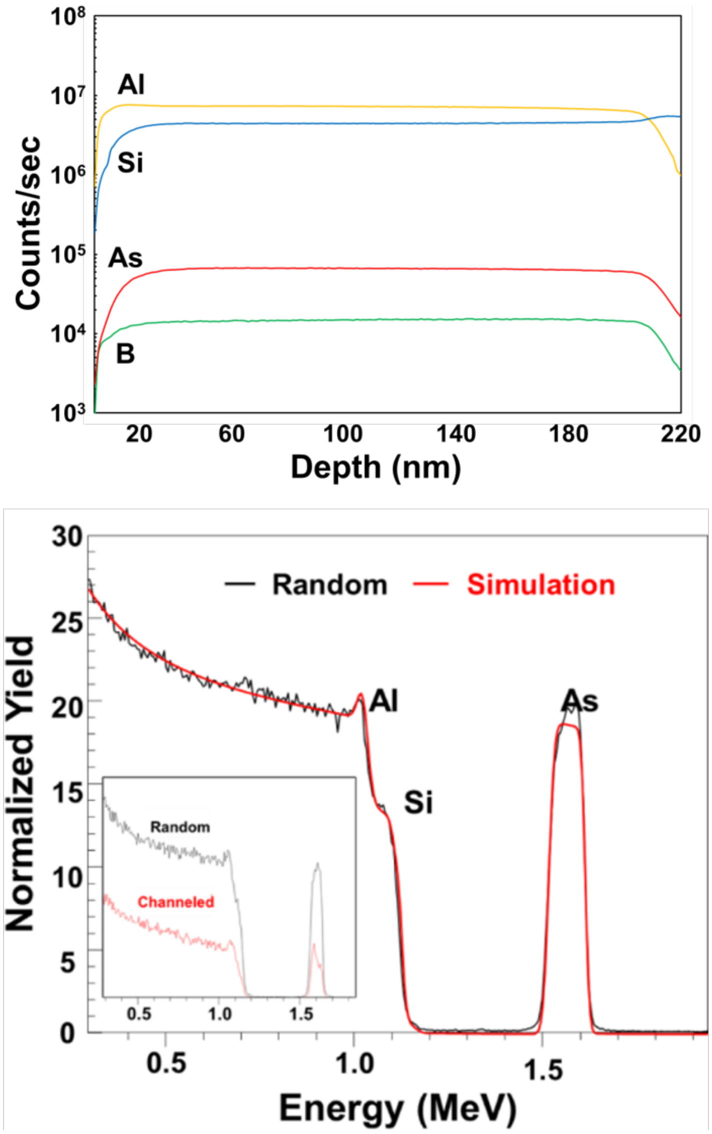

Figure 26: (top) SIMS profile of $AlAsSi_3$/Si(100) sample showing uniform elemental distribution of all atoms in the alloy. (bottom) RBS spectral fits of the same sample (red line) yielding $AlAsSi_3$ composition. Inset compares aligned and random spectra featuring the same degree of channeling in all elements as expected for a single phase material.

in lattice dimensions with Si. Representative lateral and perpendicular parameters are measured to be $a = 5.4924$ Å and $c = 5.5446$ Å, respectively. The cubic parameter is determined to be $a_0 = 5.5217$ Å in close agreement with the Vegard's law average of

5.5226 Å and with measured values of typical $AlAsSi_3$/Si(100) films grown in prior work using Al fluxes. XTEM micrographs corroborated the single phase monocrystalline nature of the alloys. However, the microstructures were found to be highly defective, containing multiple domains of stacking faults and dislocations dispersed over the entire film thickness. Collectively the results demonstrate the viability of $Al(BH_4)_3$ as a facile Al source to synthesize stoichiometric $AlAsSi_3$. The lack of significant B incorporation is surprising considering the relatively high deposition temperatures employed in the experiments. The unimolecular decomposition of $Al(BH_4)_3$ under similar conditions is known to yield amorphous products exhibiting a nominal AlB_2 composition.[66] The lack of B in the $AlAsSi_3$ films supports the notion that the $As(SiH_3)_3$ reactant facilitates the expulsion of B_2H_6, which is then pumped away and does not participate in the growth process. The initial step in the reaction mechanism may involve binding of the electropositive $Al(BH_4)_3$ with the electron-rich $As(SiH_3)_3$ to form intermediate complexes that deliver Al-As-Si_3 building blocks exhibiting near perfect tetrahedral symmetry in the crystalline state.

As in the case of the $Al_{1-x}B_xPSi_3$ alloys, Raman scattering was used to investigate the bonding environment of the B atoms in the As material. Interestingly, the relatively strong peak seen at 630 cm^{-1} in $Al_{1-x}B_xPSi_3$ samples corresponding to isolated B-P is not present for analogous B-As, in agreement with the SIMS data indicating a much lower B concentration for these samples.

3.4 Summary

For the first time the application of $Al(BH_4)_3$ as a viable CVD source to fabricate $Al_{1-x}B_xPSi_3$ semiconductors with Si-like cubic structures comprising interlinked $AlPSi_3$

and $BPSi_3$ tetrahedral units has been shown. The reaction of the compound with $P(SiH_3)_3$ produces single phase layers that grow tensile strained to the Si substrate. Similarly strained crystals were grown on GaP platforms. A significant outcome of the study is that the boron atoms are incorporated as isolated B-P pairs and their molar amount remains fairly constant within a narrow range. The boron uptake is slightly higher than needed to perfectly lattice-match bulk silicon, and no additional boron beyond this threshold was possible in spite of efforts to achieve higher levels under widely varying conditions. The band gaps of these materials are expected to be higher than Si as needed for applications in tandem Si-based photovoltaic devices with enhanced efficiencies. The approach was extended using reactions of $Al(BH_4)_3$ with $As(SiH_3)_3$ to produce stoichiometric $AlAsSi_3$ crystals incorporating doping levels of boron. The new synthetic strategy based on $Al(BH_4)_3$ may provide access to a broad range of light-element materials, including compounds that contain tetrahedral Al, B, and N atoms for applications in the light-emitting wide gap semiconductor technology space.

Chapter 4

SYNTHESIS AND CHARACTERIZATION OF MONOCRYSTALLINE $GaPSi_3$ AND $(GaP)_Y(Si)_{5-2Y}$ PHASES WITH DIAMOND-LIKE STRUCTURES VIA EPITAXY DRIVEN REACTIONS OF MOLECULAR HYDRIDES

Figures and text in this chapter were reprinted with permission from Sims, P. E.; Xu, C.; Poweleit, C. D.; Menéndez, J.; Kouvetakis, J. *Chem. Mater.* **Just Accpeted Manuscript**, DOI:10.1021/acs.chemmater.7b00347. Copyright 2017 American Chemical Society.[76]

Synopsis

This chapter presents an extension of purely chemical CVD routes to the formation and synthesis of hybrid (III-V)-IV_3 alloys. Through directed precursor development the hitherto unknown $GaPSi_3$ alloy was synthesized, and grown directly on Si(100) substrates. The realization and subsequent studies of $GaPSi_3$ were achieved through the use of $[D_2GaN(CH_3)_2]_2$, an effective molecular source of Ga. This molecule was found to cleanly deliver Ga atoms, which possess the necessary reactivity to react with $P(SiH_3)_3$, in contrast to the less reactive Ga atomic beams afforded by solid sources. Reactions between $[D_2GaN(CH_3)_2]_2$ and $P(SiH_3)_3$ on the substrate surface generate crystalline $GaPSi_3$ films devoid of C and N impurities via elimination of D_2/H_2 and $HN(CH_3)_2$, both of which are unreactive under the employed growth conditions.

Employing the CVD compatible Ga source, $[D_2GaN(CH_3)_2]_2$, the synthetic paradigm shift away from solid sources of group-III atoms is bolstered. $GaPSi_3$

alloys are an attractive synthetic target as a material which may exhibit direct-gap behavior, and be directly integrated on Si platforms. Early tight-binding calculations on one-dimensional GaP/Si_2 superlattices predict strong optical transitions in this system, three-dimensional arrangement offer more degrees of freedom possibly leading to direct-gap materials fully compatible with Si. Additionally, by replacing Al with Ga on the group-III sublattice the optical response of (III-V)-IV_3 alloys commensurate with Si is again extended, in this case, further into the IR.

4.1 Introduction

We have recently introduced molecular based synthetic approaches to prepare new families of semiconductor materials involving combinations of III-V and group-IV constituents which cannot be synthesized using conventional routes such as molecular beam epitaxy (MBE). These materials can be described with the general formula (III-V)-$(IV)_3$, and are specifically designed to extend the optoelectronic capabilities of Si based, group-IV, technologies including photovoltaics. With regard to the latter, recent theoretical studies have indicated the prototypical $AlPSi_3$ compound with lattice constant virtually equal to Si has a higher absorption in the visible range of the spectrum, making it a promising candidate for high efficiency solar cell applications.[40] Viewed from a broader context, the basic idea of the work is to explore the possibility for rational design of new crystalline solids with complex unit cells by using molecular building blocks which make it possible to manipulate the atomic-level structure of these individual crystal cells. Initial syntheses utilized a hybrid chemical vapor deposition (CVD) and MBE strategy where the group-IV and -V atoms were supplied by the single source molecular compounds $P(SiH_3)_3$ and

$As(SiH_3)_3$.[25,27] These reacted with Al atoms to produce $Al{\cdot}P(SiH_3)_3$ and $Al{\cdot}As(SiH_3)_3$ reactive intermediates which thermally decomposed via loss of H_2 to generate $AlPSi_3$ and $AlAsSi_3$ building blocks with tetrahedral structures comprising a central P/As atom surrounded by three Si and one Al atom. Interlinking of these tetrahedral blocks produced the corresponding $AlPSi_3$ and $AlAsSi_3$ extended solids directly on Si substrates as single-phase, monocrystalline layers with average diamond-like structures. The latter incorporate isolated Al-P and Al-As pairs embedded within the Si framework in a manner which prevented phase separation and III-V precipitation, ensuring single phase integrity of the resultant metastable phases. The synthesis of $AlPSi_3$ was later extended to form $(AlP)_y(Si)_{5\text{-}2y}$ derivatives with tunable Si concentrations beyond the 60% threshold of the parent structure.[26] Quaternary analogues with compositions $Al(As_{1\text{-}x}P_x)Si_3$, $Al(As_{1\text{-}x}N_x)Si_3$, and $[Al(P_{1\text{-}x}N_x)]_y(Si)_{5\text{-}2y}$ were also produced using the $N(SiH_3)_3$ compound as the source of $AlNSi_3$ building blocks.[28,29]

An important aspect of the research was to develop purely CVD routes which do not rely on solid sources. This is because this technique is far more attractive for large-scale, high-throughput fabrication of technologically relevant materials and provides more degrees of freedom in the pursuit of novel phases with specifically designed bonding configurations. The first breakthrough in this effort was based on the use of the gaseous $Al(BH_4)_3$ precursor as the source of Al and B atoms.[55] Reaction of the compound with $P(SiH_3)_3$ led to the creation of a new class of $Al_{1\text{-}x}B_xPSi_3$ alloys comprising combinations of earth abundant elements that lattice match the parent Si structure. Furthermore, the band gaps in these materials are wider than in Si, portending possible applications in dual-junction solar cells with enhanced efficiencies.[40] The next logical step in the development of practical CVD methods to grow $(III\text{-}V)\text{-}(IV)_3$ alloys is to replace the Al and B atoms in the group-III sub-lattice with Ga atoms. In this case the formation of the previously unknown $GaPSi_3$ phase analogous to $Al_{1-x}B_xPSi_3$ is an immediate target from a fundamental perspective due to the possibility that it may exhibit direct gap behavior. This is in view of the earlier calculations by Lazzouni and Sham that optical transitions arising from zone-folding in GaP/Si one-dimensional superlattices have an unusually large oscillator strength.[77] If the same property transfers over to the three-dimensional arrangements of $(III\text{-}V)\text{-}(IV)_3$ tetrahedra, further tuning may become possible, leading to direct gap materials lattice-matched with Si, or at least to materials with strong optical absorption that are fully compatible with Si substrates. On the other hand, if the optical properties are very strongly dependent on the arrangement of $(III\text{-}V)\text{-}(IV)_3$ tetrahedra, optical spectroscopy may become a powerful tool to determine which of the many possible geometrical arrangements are promoted by this synthetic approach.

This study pursues the synthesis of new alloys in the GaP-Si system using $[D_2GaN(CH_3)_2]_2$ and $[H_2GaN(CH_3)_2]_2$ delivery sources to enable incorporation of Ga in the structure. It was found that Ga atomic beams, generated from solid-source effusion cells, did not exhibit the necessary reactivity to effectively bond with $P(SiH_3)_3$, leading to the formation of samples that lacked crystallinity and compositional homogeneity. This was a consistent outcome in spite of persistent attempts under widely varied conditions of temperature, pressure and reactant flux, rendering the combined CVD/MBE strategy ineffective for the synthesis of $GaPSi_3$ and related alloys. In contrast, reactions of $[D_2GaN(CH_3)_2]_2$ with $P(SiH_3)_3$ between 525 °C and 540 °C produced crystalline $GaPSi_3$ with a fixed Si content of $\sim$60%, while reactions of $[H_2GaN(CH_3)_2]_2$ at $T > 590$ °C yielded Si-rich analogues with tunable Si contents in the 75-95% range. The compounds cleanly deliver Ga atoms via elimination of volatile and stable D_2/H_2 and $HN(CH_3)_3$ byproducts. The Ga atoms then combine with $P(SiH_3)_3$ to deposit monocrystalline films which grow lattice matched on Si(100) wafers, allowing straightforward characterization of the structural, bonding and optical properties as described in detail below.

4.2 Experimental

4.2.1 Synthetic Considerations and Precursor Development

The initial strategy for the synthesis of $GaPSi_3$ involved development of the $GaD_3{\cdot}NH(CH_3)_2$ and $GaH_3{\cdot}NH(CH_3)_2$ molecular adducts as the sources of Ga atoms. It is envisioned that these would thermally dissociate by releasing $NH(CH_3)_2$ to yield $Ga(D/H)_3$, which would then combine with $P(SiH_3)_3$ to produce $Ga(D/H)_3{\cdot}P(SiH_3)_3$ intermediate complexes en route to $GaPSi_3$. However, it was observed that the adducts were not stable and steadily decomposed in their storage container at room temperature via elimination of D_2 or H_2 over several days to produce the $[D_2GaN(CH_3)_2]_2$ and $[H_2GaN(CH_3)_2]_2$ derivatives in the gas-phase. The latter are known to adopt dimeric structures in which the N atoms bridge the $Ga(D/H)_2$ units to form four-membered rings, as illustrated in Figure 27.[78] The starting materials are prepared as indicated in Tang et al. using standard inert atmosphere techniques and purified through a series of traps kept at -20 °C, -78 °C, and -196 °C.[78] The pure compounds were collected in the -20 °C trap as colorless liquids and then stored ay -25 °C in a drybox. They are not pyrophorhic and decompose in air to form white residues. As indicated in Tang et al. both molecules are volatile with ~1 Torr vapor pressure and remain thermally stable at room temperature for several weeks without further decomposition, making them viable CVD sources of Ga atoms.[78] Prior to growth the precursors were examined by gas-phase IR and the spectra were consistent with those of the above dimeric materials as described in Baxter and Downs.[79] To test the feasibility of $[D_2GaN(CH_3)_2]_2$ as a Ga delivery vehicle controlled decomposition experiments were performed between 450 and 550 °C, and the results indicated formation of mostly amorphous Ga deposits on the substrate surface, indicating the compound is a suitable reagent for the synthesis objectives. The proposed decomposition mechanism involves elimination of $DN(CH_3)_3$ and D_2 byproducts as illustrated by the equation:

$$[D_2GaN(CH_3)_2]_2 \rightarrow 2\ Ga + D_2 + 2\ DN(CH_3)_2 \tag{4.1}$$

The dimethylamine is thermally robust under low temperature and pressure conditions, and is pumped away from the growth front, leaving behind pure Ga. In subsequent reactions with $P(SiH_3)_3$, the Ga atoms then combine to form $Ga{\cdot}P(SiH_3)_3$ intermediates which decompose by eliminating H_2, finally producing the desired $GaPSi_3$ building blocks of the target solid structure as described below.

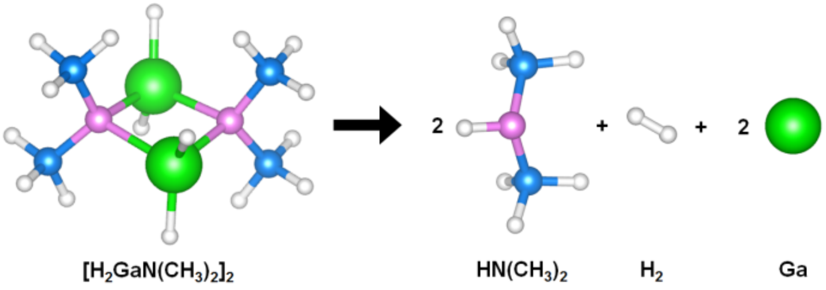

Figure 27: Decomposition reaction of $[H_2GaN(CH_3)_2]_2$ showing structural models of reactants and products.

To gain insight into the mechanism involved in the thermal dissociation of $[D_2GaN(CH_3)_2]_2$ and $[H_2GaN(CH_3)_2]_2$ precursors to yield free Ga atoms, theoretical calculations of the reaction thermochemistry were done. A series of density functional theory simulations were first carried out to determine the structural and ground state electronic properties of reactants and products depicted in Equation 4.1. The Gaussian09 package was applied at the PBE (Perdew, Burke, Ernzerhof) level using the 6-311++(3pd,3df) basis set in all cases.[80,81] Using the ground state energies the reaction is found to have a positive ΔE. However, upon consideration of the reaction thermochemistry the Gibbs free energy (ΔG) becomes negative above 180 °C and 1.0×10^{-5} Torr, indicating that the dissociation process in Equation 4.1 is thermodynamically favorable under the conditions employed in the growth experiments, further validating the results of the control trials described above.

Previous studies have reported the use of the $GaH_3{\cdot}NH(CH_3)_2$ parent adduct to deposit device quality GaAs using metal-organic CVD methods.[82–85] In these experiments the compound was dispensed from conventional bubblers and was transported into the reaction zone using a carrier gas. The films were found to be devoid of carbon and nitrogen impurities, indicating the molecule had decomposed cleanly at the low temperatures employed. While these studies do not mention the formation of $[H_2GaN(CH_3)_2]_2$ intermediates in the course of the experiment, the thermal dissociation of $GaH_3{\cdot}NH(CH_3)_2$ observed suggests that the presence of these species in the reaction mixtures plays a role in the formation of the final product.

During the course of this study that the dominant gas-phase component of the precursor samples is the $[H_2GaN(CH_3)_2]_2$ dimer, as demonstrated by gas-phase IR spectroscopy of each sample prior to every growth experiment, as indicated previously. This conclusion is corroborated by prior reports of gas electron diffraction of $GaH_3{\cdot}NH(CH_3)_2$ adduct, which showed that the vapor phase comprised the $[H_2GaN(CH_3)_2]_2$ dimer rather than the $GaH_3{\cdot}NH(CH_3)_2$ monomer.[78]

As indicated in the introduction section the samples in this study are grown by low pressure CVD on Si-buffered silicon wafers via reactions of $[D_2GaN(CH_3)_2]_2$,

$[H_2GaN(CH_3)_2]_2$, and $P(SiH_3)_3$. The latter was prepared by directly combining Li_3P and $BrSiH_3$ in diethyl ether. This generates a reasonable yield approaching 50%, making the compound a viable reagent for large scale applications. All co-reactants were thoroughly distilled to achieve semiconductor-grade purity suitable for deposition of device-quality layers. From a thermal stability perspective, $[D_2GaN(CH_3)_2]_2$ is slightly more robust than $[H_2GaN(CH_3)_2]_2$ due to the enhanced kinetic stability of the Ga-D bonds, allowing better control of the reaction rate with $P(SiH_3)_3$ under the growth conditions employed, which lead to stoichiometric $GaPSi_3$. It is envisioned that the synthesis in this case proceeds through the formation of $Ga{\cdot}P(SiH_3)_3$ transient adducts generated by combining the Ga atoms furbished by the precursor and $P(SiH_3)_3$. These adducts are highly reactive and readily eliminate the Si-H bonds as H_2 to form $GaPSi_3$ building units, which then interconnect to produce the extended lattice akin to the $AlPSi_3$ phase described in Watkins et al.[25] This process follows the reaction pathway:

$$\mathrm{Ga} + \mathrm{P(SiH_3)_3} \rightarrow \text{"}\mathrm{Ga{\cdot}P(SiH_3)_3}\text{"} \rightarrow \tfrac{9}{2}\mathrm{H_2} + \mathrm{GaPSi_3} \tag{4.2}$$

4.2.2 Materials Growth

The reactor utilized in this study is a single-wafer deposition system described elsewhere.[55] The substrates were rectangular segments cut from a double sided Si(100) wafer (ρ = 1-10 $\Omega{\cdot}$cm) with approximate size of 1 cm × 1.5 cm to fit onto the heating stage of the ultra-high vacuum (UHV) CVD reactor. The samples were first dipped in a 5% HF/methanol solution and then dried using a nitrogen nozzle. They were clamped onto the stage using metal clips and inserted into the chamber under UHV conditions via a turbo-pumped load lock system. The substrates were initially heated inside the chamber on the sample stage at 650 °C and 10^{-9} Torr for several hours by passing current through the wafer to desorb the hydrogen passivation and any other volatile contaminants. Note that a chamber base pressure of 10^{-9} Torr was obtained using an ion- and turbo-pump assembly. To remove the surface oxide and other volatile impurities, the samples were flashed to 1050 °C under vacuum for ten seconds a total of ten times. The chamber pressure during the flashing cycles did not exceed 1.0×10^{-8} Torr, ensuring optimal vacuum conditions for generating a clean surface for subsequent epitaxy. Immediately thereafter, a 50 nm thick silicon buffer layer was grown on the wafer using Si_4H_{10} (tetrasilane) as the source of Si at 540 °C and 1.0×10^{-5} Torr. The purpose of the Si layer was to generate a pure growth surface devoid of carbon or other types of residues that the flashing step does not fully remove. The formation of the buffer was immediately followed by deposition of $GaPSi_3$ epilayers achieved by admitting the $[D_2GaN(CH_3)_2]_2$ and $P(SiH_3)_3$ gases separately into the reactor using a differentially-pumped gas manifold and high-precision UHV-compatible needle-valves. The compounds were directed to the substrate using individual delivery nozzles and allowed to combine over the growth surface to commence crystal growth. This arrangement prevented premixing of the chemicals to avoid side reactions. In a typical experiment, a four-fold excess of $P(SiH_3)_3$ gas was used relative to $[D_2GaN(CH_3)_2]_2$ in order to attain stoichiometric 1:1 Ga to P ratio in the films. Typical deposition temperatures and pressure were 525-545 °C and 1.0×10^{-5} Torr, respectively, yielding layers with thickness of $\sim$90-100 nm at a growth rate of 6-10 nm/minute. Under these conditions, the samples exhibited an a average $GaPSi_3$ stoichiometry with slight deviations, up to 5%, of the Si content from the ideal 60% (Si_3) limit in some cases. The key to the successful synthesis of the expected phase is the excess $P(SiH_3)_3$ at the growth front that serves to achieve maximal activation of the Ga atoms furnished by the $[D_2GaN(CH_3)_2]_2$ precursor. Growths utilizing less than optimal $P(SiH_3)_3$ partial pressures produced Ga rich samples with inferior crystallinity and dubious phase purity. Furthermore, control experiments involving the unimolecular deposition of $P(SiH_3)_3$ showed that the compound remains intact under the conditions employed, indicating no side reactions due to its thermal dissociation occur in this case that can adversely affect the outcome of the process.

In contrast to $[D_2GaN(CH_3)_2]_2$, the $[H_2GaN(CH_3)_2]_2$ analogue did not react with $P(SiH_3)_3$ as expected under the same temperature conditions. Instead, the compound decomposed to form volatile byproducts which were pumped away leaving behind no discernible film growth. Therefore, a different approach was pursued, which combined gaseous aliquots of $[H_2GaN(CH_3)_2]_2$ with $P(SiH_3)_3$ at a 1:2 ratio into a 1.0 L container to prepare stock mixtures where the reactants are intimately dispersed to ensure a uniform flux density over the substrate surface. In this case, crystalline films were obtained between 590-605 °C with compositions ranging from $GaPSi_6$ to $GaPSi_{24}$. Under these conditions, the Si content in the films increased above the 60% limit expected on the basis of intact incorporation of the $GaPSi_3$ building blocks. This can be attributed to side reactions in the mixture generating volatile Si-rich intermediates which incorporate additional Si at the higher temperatures employed. The resultant materials are analogous to the previously reported $(AlP)_y(Si)_{5-2y}$ alloys, in which the Si content was varied from 60-90% as a function of temperature.[26] As in the case of $(AlP)_y(Si)_{5-2y}$, the $(GaP)_y(Si)_{5-2y}$ materials also adopt tetrahedral structures containing orientationally disordered GaP pairs randomly embedded within the Si-like framework structure described in subsequent sections.

4.3 Results and Discussion

4.3.1 Structural and Compositional Characterizations of $GaPSi_3$ Samples

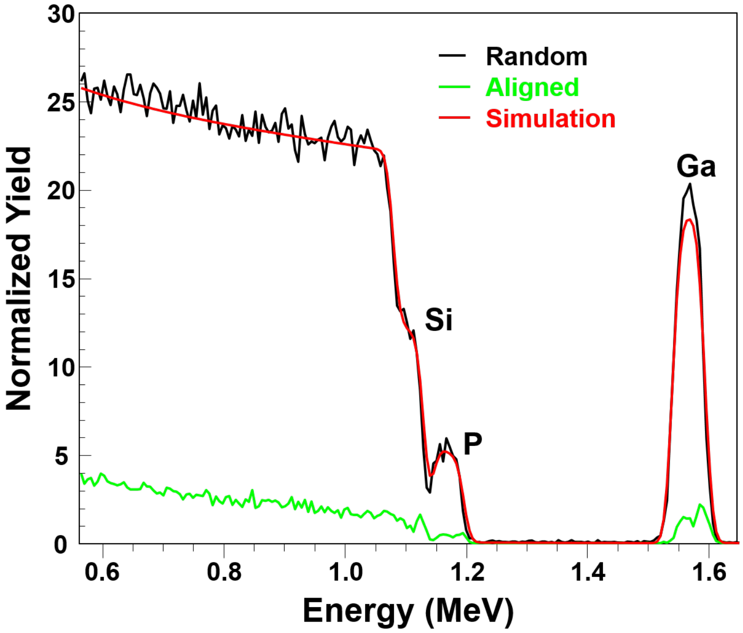

Figure 28: Random RBS spectrum (black) of a $GaPSi_3$ sample showing distinct signals for the Ga, P, and Si atoms in the film. Simulated spectrum (red) using the program RUMP provides a $GaPSi_3$ composition and thickness of 105 nm. The channeled spectrum (green) reveals a high level of epitaxial alignment between the epilayer and the Si substrate.

The films were characterized for composition and structure using Rutherford Backscattering (RBS), high-resolution X-ray diffraction (HR-XRD), and aberration-corrected transmission electron microscopy (TEM). Figure 28 shows random and channeled RBS spectra (black), and (green) lines, respectively, of a representative $GaPSi_3$ sample measured at 2.0 MeV, illustrating a high degree of alignment between the epilayers and the Si substrate. This behavior is consistent with a monocrystalline material exhibiting a diamond-like structure with fully substitutional Ga, P, and Si atoms. Quantitative fits of the random spectrum (red line) yields an average $GaPSi_3$ stoichiometry and a thickness of 105 nm. The structure of the samples was initially investigated using HR-XRD. The data was collected on a PANalyitical X'Pert PRO diffractometer equipped with a monochromator and a triple-axis detector. Figure 29(a) shows ω-2θ plots of a $GaPSi_3$ film (blue line) and a reference GaP(100) wafer (dashed black line) in the vicinity of the Si wafer (004) reflection, which serves as an internal standard. As expected, the position of the $GaPSi_3$ peak is situated in between those of GaP and Si end members, indicating the material is a single phase alloy, not a mixture between the two constituents. The vertical lattice constant (c) of $GaPSi_3$, determined from the d-spacing of the (004) peak, was found to be 5.441 Å, which is intermediate to those of bulk GaP (5.4509 Å) and Si (5.4309 Å) reference materials. The in-plane lattice parameter (a) was measured using off-axis reciprocal space maps of the (224) and (135) reflections shown in panels (b) and (c) respectively. The plots show the material is pseudomorphic to Si and it is compressively strained. The tetragonal lattice constants were measured to be $c_{224} = 5.4417$ Å, $a_{224} = 5.4306$ Å, $c_{135} = 5.4416$ Å, and $a_{135} = 5.4311$ Å. The corresponding relaxed (cubic) lattice constants were determined to be $a_{0,(224)} = 5.4359$ Å and $a_{0,(135)} = 5.4361$ Å indicating close agreement from (224) and (135) reflections. The XRD data collectively showed the material is minimally larger than Si by 0.10%, ensuring the critical thickness of fully coherent films may be well in excess of 1 μm, as required for applications as a viable defect-free solar cell component integrated upon Si. Overall, a series of 9 $GaPSi_3$ samples were measured in detail by XRD and the data indicated the lattice parameter remains fairly constant, at about 5.4365 Å, irrespective of growth temperature between 525 and 540 °C. Another point to make with respect to the on axis spectrum of $GaPSi_3$ in panel (a) is that the plots show thickness fringes due to interference of the x-ray beam reflected from the film surface and interface. This indicates the presence of a sharp and uniform growth plane, as corroborated by cross-sectional TEM (XTEM) presented in Figure 30.

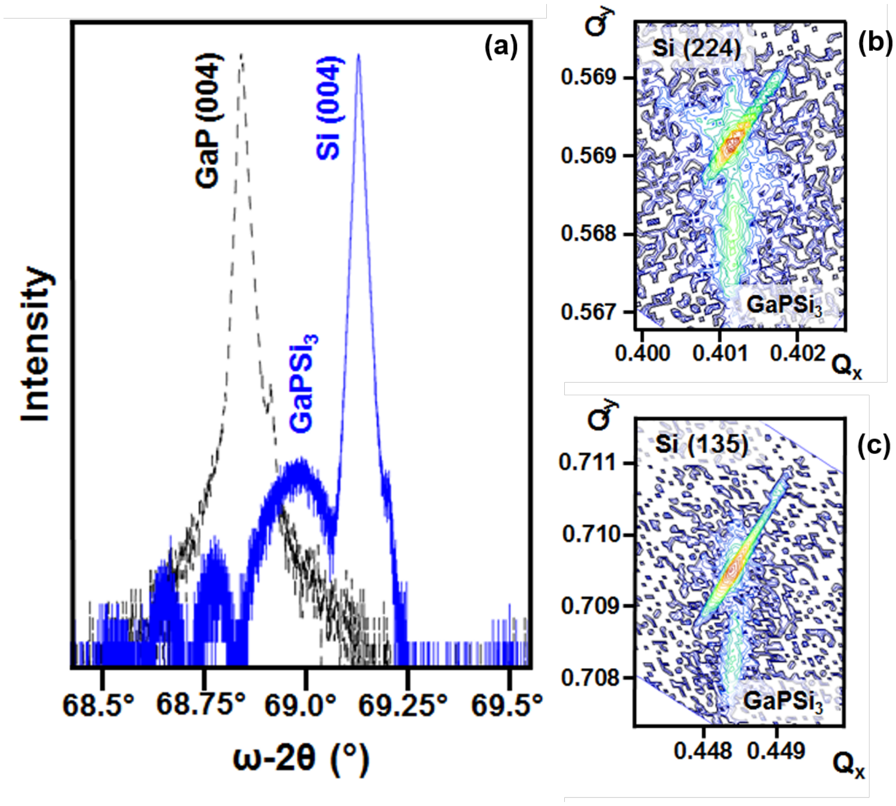

Figure 29: (a) ω-2θ XRD plots showing a full profile of the $GaPSi_3$ (004) peak at slightly lower angle than the Si (blue line) with thickness fringes on one side. The full width at half maxima of the alloy and Si peaks are 99 and 19 arc-seconds, respectively. The spectrum is compared with that of a GaP(100) wafer (dashed line). The data indicate that the $GaPSi_3$ lattice parameter is larger than Si and smaller than GaP as expected. Panels (b) and (c) show (224) and (135) reciprocal space maps of the $GaPSi_3$/Si sample, respectively, indicating that the layer is pseudomorphically strained as evidenced by the alignment of the Si and $GaPSi_3$ peaks along the pseudomorphic line in both cases.

The top panel in Figure 30 is a diffraction contrast micrograph of the entire sample featuring the epilayer, the buffer, and the Si wafer. The data was acquired at 300 kV using an FEI Titan 80-300 electron microscope. A uniform contrast is seen throughout, indicating the material is a single phase alloy with no evidence of GaP and Si separation, or compositional inhomogeneity due to phase segregation. The latter is typically manifested as striations originating at the interface and propagating through the bulk to the top surface in these types of (III-V)-(IV) materials. The bottom interface between the buffer and the wafer is defective, likely due to residual impurities remaining on the Si wafer after flashing. By contrast, the upper interface between the epilayer and buffer is smooth, uniform, and defect-free, thereby providing a suitable platform for nucleation and growth of high quality $GaPSi_3$ crystals. The surface profile of the epilayer is relatively flat within the field of view with no discernible flaws or large scale undulations. The film thickness determined by TEM is 100 nm and in agreement with the RBS-measured 105 nm value, well within the critical limit for strain relaxation due to the close lattice matching between Si and $GaPSi_3$. The lower panel of Figure 30 is a high-resolution micrograph of the buffer–epilayer interface showing a close alignment of the $\{111\}$ lattice fringes due to the structural similarity between the Si-like film and the Si substrate. The results collectively demonstrate formation of crystalline materials with long range microstructural homogeneity devoid of dislocations, despite the difference in bonding character between the polar and non-polar components of the alloy.

To further investigate the single phase character of the material, a complementary characterization was conducted by annular dark-field microscopy using a JEOL ARM200F aberration-corrected scanning transmission electron microscope (STEM). Figure 31(a) shows a medium-angle annular dark-field (MAADF) image of $GaPSi_3$ and Si layers. The intensity difference is mostly due to the difference in the atomic mass

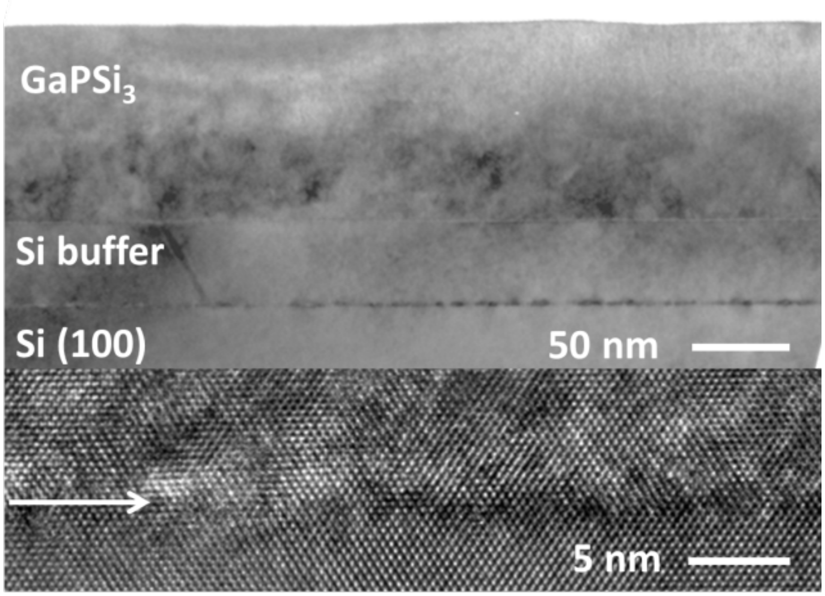

Figure 30: (Top) Diffraction contrast XTEM micrograph of a GaPSi$_3$ film shows planar morphology and monocrystalline structure. The uniform contrast indicates that the material is a single-phase alloy rather than a mixture of GaP and Si end members. (Bottom) High-resolution micrograph, showing a sharp, uniform, and defect-free buffer–epilayer interface due to the close lattice matching between the two materials.

between the two materials. The contrast is highly uniform and featureless throughout the top layer, corroborating the existence of a homogeneous phase. The image is free of columnar defects caused by compositional segregation as indicated above. This observation supports the notion that the low temperature employed prevents stoichiometry and structure variations that may arise due to slight fluctuations in deposition parameters owing to the complexity of the reaction pathway and the intricate crystal assembly mechanism. Figure 31(b) is a high-resolution high-angle annular dark-field (HAADF) image of the interface between the alloy (bright region) and Si-buffer (dark region) indicating a uniform transition between the two materials. The image is taken in [110] projection and features elongated bright spots corresponding to pairs of atoms or “dumbbells”. The data corroborates the absence of chemical inhomogeneities at the nanometer scale and further demonstrates the high structural quality of the layers with no sign of misfit dislocations or threading defects.

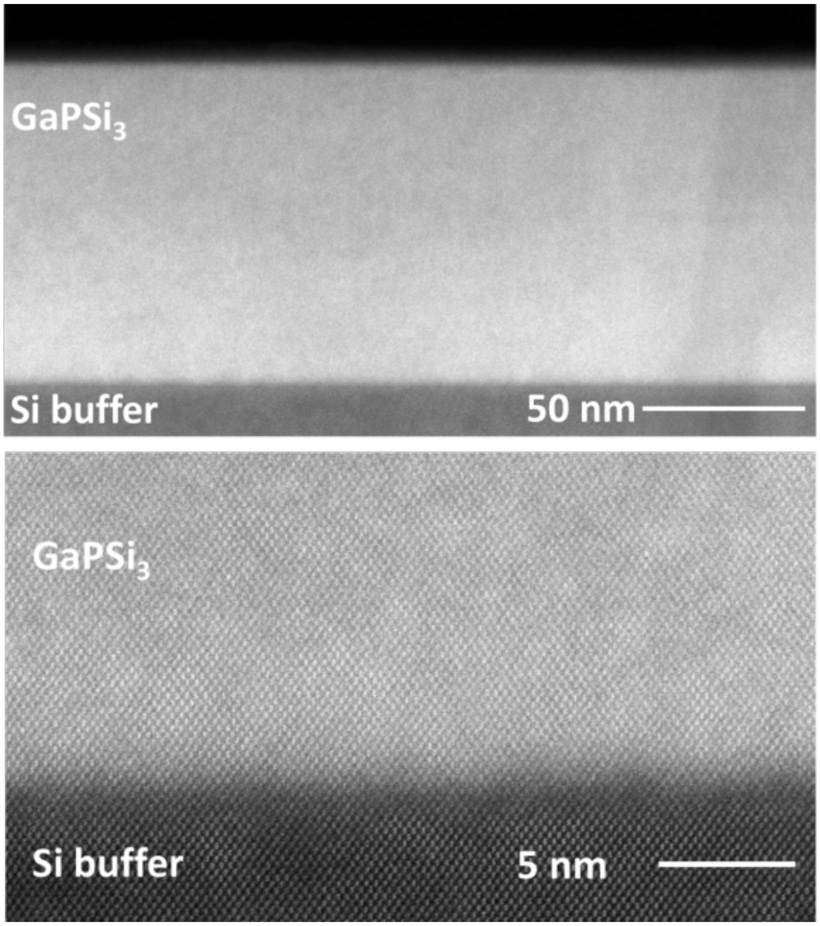

Figure 31: (a) STEM-MAADF image showing the GaPSi$_3$ epilayer, and the Si-buffer as dark and light contrast regions, respectively. The uniform contrast indicates compositional homogeneity. (b) High-resolution HAADF image of the interface showing a defect-free microstructure.

Finally, note that additional GaPSi$_3$ samples grown at the lower end of the temperature range, near 525 °C, exhibited similar RBS and HR-XRD spectra to those grown at 540-545 °C. The growth rates were similar irrespective of temperature, and the compositions were readily reproduced under the optimized conditions of flux ratio and deposition pressure. Also note that the best quality AlPSi$_3$ samples reported in prior work were also deposited between 525-550 °C with growth rates of ~4 nm/minute. Despite the fact the latter material was grown using atomic beams, while the former was produced via bimolecular reactions of neutral precursors. This further supports the proposed formation of intermediate building blocks with tetrahedral geometries facilitating the crystal assembly in both cases.

4.3.2 Insights into Bonding and Structure of $GaPSi_3$ Using Quantum Chemical Simulations

To further elucidate the reaction mechanism of $GaPSi_3$ and gain insights into the assembly of the proposed structure via interlinking $GaPSi_3$ building blocks, the molecular reactant and solid state product involved in the process described by Equation 4.2 above: $Ga{\cdot}P(SiH_3)_3 \rightarrow \frac{9}{2}\ H_2 + GaPSi_3$ are calculated. An important objective was to characterize structural distortions and bonding strains that may occur when the molecular cores, furnished by $Ga{\cdot}P(SiH_3)_3$, are incorporated intact into the $GaPSi_3$ lattice, and determine if the conditions are favorable for forming a regular diamond-like lattice. For this purpose, the bonding parameters of the $Ga{\cdot}P(SiH_3)_3$ monomeric unit with those of discrete $GaPSi_3$ units extracted from the equilibrium crystal structure of the solid material are compared. To determine the bonding properties of $Ga{\cdot}P(SiH_3)_3$, quantum chemical calculations of the molecular and electronic structure were performed. To make the calculations tractable, the Ga atom was terminated with H atoms to form the hypothetical adduct $GaH_3{\cdot}P(SiH_3)_3$, that closely resesmbles the molecular geometry of $Ga{\cdot}P(SiH_3)_3$. To obtain the bonding parameters of a single $GaPSi_3$ unit, the equilibrium structure of the $GaPSi_3$ solid material analogous to the $AlPSi_3$ prototype was calculated (details are described later in this chapter). The results are summarized in Figure 32, which illustrates the predicted model structure of $GaH_3{\cdot}P(SiH_3)_3$ in panel (a), showing longer Ga-P bond distances of 2.55 Å than the average Si-P counterparts of 2.26 Å, as expected. The latter is similar to the experimental 2.25 Å value of the $P(SiH_3)_3$ compound obtained from gas electron diffraction analysis of the structure.[86] This variation in bond lengths is reflected in the unequal edge lengths of the tetrahedral core of the $GaH_3{\cdot}P(SiH_3)_3$ molecule shown in panel (b). Here, the basal edges between the Si atoms of the PSi_3 fragment are shorter (3.54 Å) than the apical counterparts along the Ga-P direction (4.07 Å), generating a significant deviation from a regular tetrahedron in the molecular core. Panels (c) and (d) show the tetrahedral unit in the crystal, indicating that the Ga-P bond is compressed relative to the free molecule from 2.55 Å to 2.42 Å, while the Si-P bond is stretched from 2.26 Å to 2.31 Å. The net effect is to remove the edge length distortions along the Ga-Si (3.85 Å) and Si-Si (3.80 Å) edges going from molecule to crystal, and produce a more regular tetrahedron with average bond angles of $\sim 110 \pm 3°$, approaching the expected value of 109.47°. These results suggest the deviations from tetrahedral geometry in the $GaPSi_3$ core of the model molecule must be mitigated upon incorporation of the $GaPSi_3$ unit into the crystal lattice, allowing the formation of a diamond-like tetrahedral lattice.

As discussed above, the level of $GaPSi_3$ accommodation in the lattice is elucidated by comparing the structure of the $GaH_3{\cdot}P(SiH_3)_3$ molecular core and the $GaPSi_3$ fragment extracted from the crystalline solid. The latter was calculated using the Quantum ESPRESSO software package following procedures similar to those described in prior work for $AlPSi_3$ and described below.[87] Structural and electronic optimizations of $GaPSi_3$ were performed using a 20-atom unit cell. The calculations were carried out under the generalized gradient approximation for exchange and correlation described

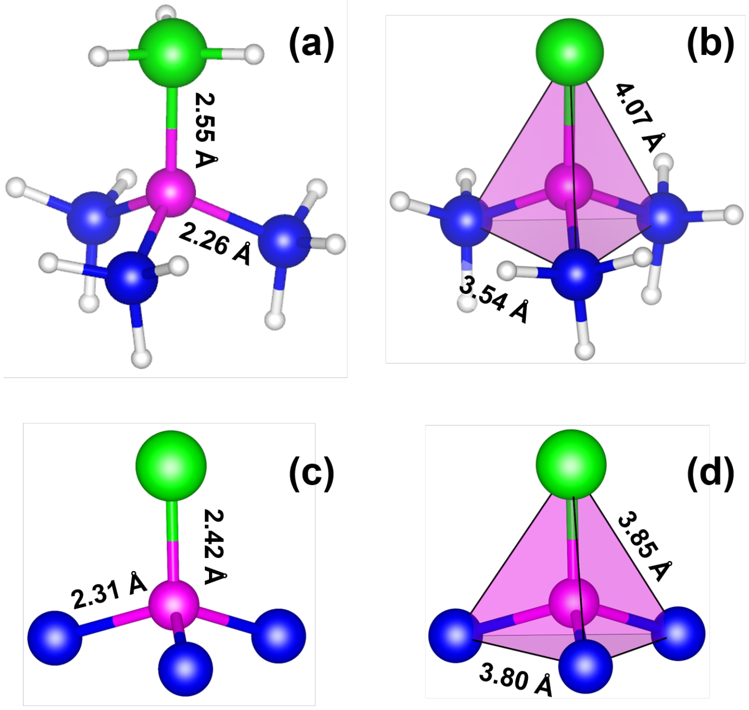

Figure 32: Calculated molecular model of $GaH_3{\cdot}P(SiH_3)_3$ (a) and its tetrahedral core (b) show slight deviations from regular tetrahedral geometry. Building unit (c,d) extracted from the equilibrium $GaPSi_3$ structure indicate the molecular core (b) regularizes upon incorporation into the crystal as evidenced by the adjustments of bonding parameters between the molecule (a,b) and the solid (c,d).

by PBE.[81] The structures were converged with residual forces < 0.001 eV/Å and stresses $< 2.0\times10\text{-}4$ eV/Å^3. As indicated above, the unit cell chosen for this study is based on previously reported structures of $AlPSi_3$ and $AlAsSi_3$ in which III-V atomic pairs are isolated within the group-IV matrix.[25,27] The group-III atoms occupy a sub-lattice on which they are third nearest neighbors, eliminating energetically unfavorable III-III atom interactions. In the case of the $GaPSi_3$ system, the ground state structure is monoclinic, C1c1 (space group 9) and can be described with a unit cell containing four ordered tetrahedral units, as shown in Figure 33. The atomic positions only deviate slightly from the ideal diamond-cubic positions, corroborating

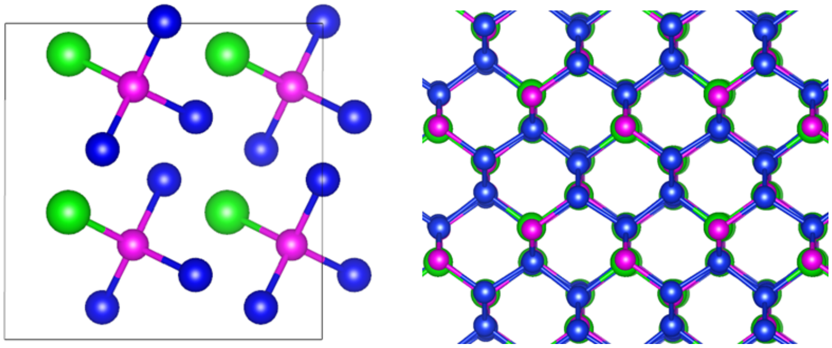

Figure 33: (left) 20-atom cell of $GaPSi_3$ showing the four ordered tetrahedral units. (right) Structural model of $GaPSi_3$ in [110] projection. No obvious distortion of the atomic positions within the tetrahedral environment of the alloy are visible in this orientation, indicating a virtually ideal diamond-like lattice.

the assembly of a regular tetrahedral network. This is illustrated in the right panel of Figure 33, showing the relaxed $GaPSi_3$ structure projected along [110] equivalent directions revealing a diamond-like pattern with close alignment of the dimers or "dumbbells" of the constituent atoms.

Additionally, optimized structures were obtained for GaP, Si, and $AlPSi_3$ using the same computational parameters. The ground state structural data of $GaPSi_3$, $AlPSi_3$, and Si are listed in Table 3. The cubic lattice parameters $\langle a_0 \rangle$ show reasonable agreement between experiment and theory, taking into account the known PBE overestimation of unit cell dimensions. The $\langle a_0 \rangle$ of $GaPSi_3$ is determined to be 5.4766 Å using $a_0 = (8\Omega)^{1/3}$, where Ω is the atomic volume calculated by dividing the cell volume by the number of atoms. A comparison with the calculated Si value 5.495 Å, obtained using the same method, yields a 0.13% lattice mismatch, which is remarkably close to the observed 0.10%, indicating an excellent agreement between theory and experiment. The lattice parameter values of the conventional monoclinic cell (a, b, c, and γ) for $GaPSi_3$ are also listed in the table, showing a close agreement with the $AlPSi_3$ prototype, further validating the observed experimental trends.

Table 3: Structural and thermodynamic properties of $GaPSi_3$, along with Si and $AlPSi_3$ reference materials. The data in the table includes the number of formula units (Z) per cell, the formation energy (E_a) and the experimental/calculated lattice parameters of the above materials.

	Z	a (Å)	b (Å)	c (Å)	α (°)	β (°)	γ (°)	$\langle a_0 \rangle_{\text{calc.}}$ (Å)	$\langle a_0 \rangle_{\text{exp.}}$ (Å)	E_a (eV)
$GaPSi_3$	4	8.6621	8.6241	5.4975	90	90	90.12	5.4766	5.4365^{a}	1.8156
$AlPSi_3$	4	8.6957	8.6723	5.5301	90	90	90.28	5.5048	$5.43090^{a,\,25}$	0.8239
Si	8	5.4695	5.4695	5.4695	90	90	90	5.4695	5.4309^{a}	—

Note: Experimental lattice parameters were determined in this work using identical experimental setup for consistency and denoted by ^{a}.

The ground-state energy for $GaPSi_3$ has also been calculated relative to the binary compound GaP and elemental Si, and is determined to be slightly unstable with respect to the formation of the alloy from these end-members. This outcome offers a persuasive explanation to the experimental observation that low temperature conditions are required to secure the formation of these metastable materials as single phase alloys. High temperature growths above 570 °C invariably produced segregated samples as evidenced by XTEM analysis. This is in contrast to $AlPSi_3$, which can be obtained as a single phase at higher temperatures, up to 600 °C with no sign of Si segregation. This observation is corroborated by the two-fold increase in the formation energy, E_a, of $GaPSi_3$ relative to $AlPSi_3$ obtained by the thermochemistry calculations as illustrated in Table 3.

4.3.3 Characterization of Si-rich $(GaP)_y(Si)_{5-2y}$, $y > 1$ Samples

As indicated above, the reactions of $[H_2GaN(CH_3)_2]_2$ with $P(SiH_3)_3$ produced Si-rich alloys exceeding the 60% Si threshold of $GaPSi_3$. These materials were also fully characterized for composition, structure and phase purity using RBS, XRD, and TEM. The data collectively showed the presence of fully crystalline and completely homogeneous materials. This is illustrated in Figure 34 which shows a diffraction contrast micrograph of a material with $GaPSi_5$ composition grown on Si. The epilayer is over 200 nm thick and exhibits a flat surface profile and a uniform contrast throughout the image, as expected due to the absence of phase segregation. Note that the dark and bright bands visible along the horizontal direction correspond to thickness variations in the electron transparent TEM specimen. Occasional defects are visible within the interface region in spite of the close lattice matching of $GaPSi_6$ with the Si-buffer.

These may originate from impurity sites on the Si surface and propagate along {111} planes for a short distance into the film, about 20 nm. The top segment of the crystal is free of dislocations and other defects including vertical striations, which have been previously observed in analogous alloys containing Al in place of Ga.

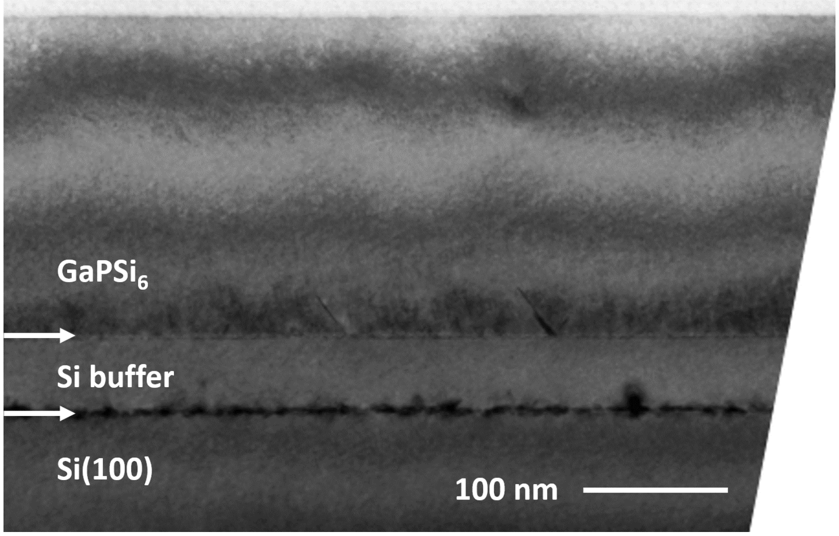

Figure 34: Diffraction contrast XTEM micrograph of $GaPSi_6$ grown on Si-buffered wafers via reactions of $[H_2GaN(CH_3)_2]_2$ and $P(SiH_3)_3$.

To further investigate the structural and compositional uniformity of $GaPSi_6$ and rule out separation of Si-rich domains, element-selective STEM-EELS (electron energy loss spectroscopy) mapping was performed using a Nion UltraSTEM100 equipped with a Gatan Enfinium^{TM} EELS spectrometer. This allowed both atomic-resolution imaging and chemical composition mapping simultaneously using STEM and EELS. Figure 35(a) shows a high-resolution STEM-HAADF image of the region of the sample analyzed in this experiment illustrating the atomic columns of the cubic lattice depicted as pairs of bright spots in [110] projection. EELS spectra were collected from this area which is also identified by the STEM image in panel (b). This image is acquired concurrently and represents a live scan of the actual lattice columns being

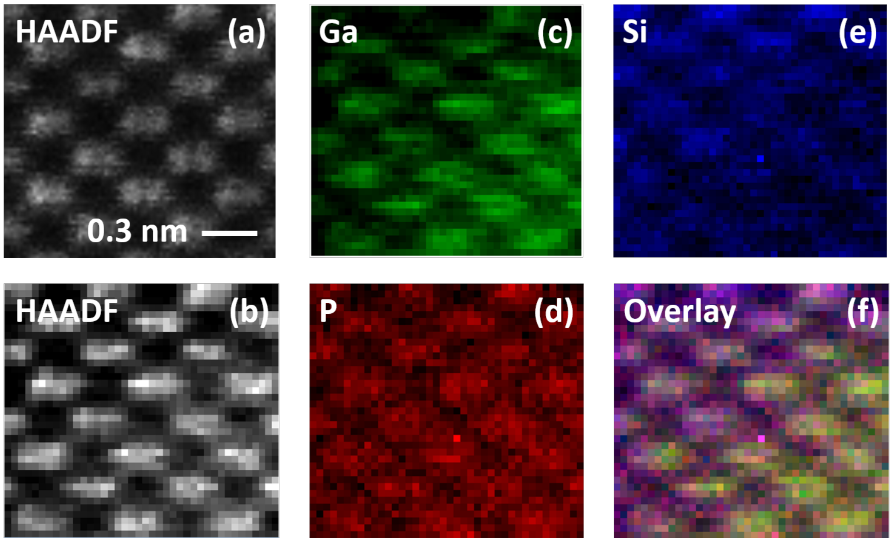

Figure 35: STEM-EELS maps of $GaPSi_6/Si(100)$ sample showing the atomic columns of the diamond-like lattice; (a) STEM-HAADF image of the atomic columns in [110] projection; (b) "live" image of the area probed by EELS; (c) Gallium K-edge map; (d) Phosphorus K-edge map; (e) Silicon K-edge map; (f) Overlay of Ga, P and Si maps indicating a fairly uniform distributions of the atoms down each atomic column.

analyzed. The EELS spectra showed distinct signals corresponding to Ga, P, and Si ionization edges (not shown) which were then used to generate elemental maps for each of the three elemental components illustrated in panels (c), (d) and (e), respectively. The maps show distinct dimers throughout each map, indicating that the projected columns contain all three elements and each element is uniformly arranged throughout individual crystal columns, consistent with a diamond-like average lattice. Figure 35(f) is an overlay of the three atomic maps illustrating the atoms are well distributed within the volume faction of the sample probed in this case. This observation provides strong evidence that Ga, P, and Si occupy the same lattice at the nanoscale, further corroborating the conclusion that the bulk material is a single phase alloy. The slightly stronger green signal on the right corner of panel (c) is attributed to beam damage due to the higher sensitivity of gallium to the electron beam.

4.3.4 Raman and Ellipsometry Studies

Support for the above interpretation can also be obtained from Raman scattering experiments. Figure 36 shows the Raman spectrum from a $GaPSi_3$ sample after subtraction of the Si Raman peak from the substrate. The spectrum is similar to the previously reported $AlPSi_3$ alloy. The main Raman peak at 513 cm^{-1} is considerably downshifted from the pure Si Raman peak at 521 cm^{-1}.[25] This frequency shift is consistent with the Ga and P atoms being uniformly distributed in the Si matrix. The second feature of interest occurs in the 350-400 cm^{-1} range and overlaps in frequency with strong peaks in the optical phonon density of states (DOS) in pure GaP between the transverse optic (TO) and longitudinal optic (LO) frequencies.[88] The 350-400 cm^{-1} structure is broad and inconsistent with pure GaP inclusions, which should produce much sharper peaks at the TO and LO frequencies. Note that the phonon DOS in AlP peaks at a higher frequency $\sim$450 cm^{-1}, and therefore the secondary structure seen here for $GaPSi_3$, which appears as a distinct broad structure in Figure 36, becomes a shoulder of the main peak in the $AlPSi_3$ spectra.[25]

The dielectric function of $GaPSi_3$ and its Si-rich analogues $(GaP)_y(Si)_{5-2y}$ with $y > 1$ were investigated using spectroscopic ellipsometry. The spectra of the samples were collected using a variable-angle spectroscopic ellipsometer (VASE from J. A. Woolam Co.) with photon energies between 0.6-4.6 eV with a step size of 10 meV and an incident angle of 70 degrees. The data were first fitted using a 3-layer model which includes a Si substrate layer, a parameterized GaP-Si layer, and a surface layer whose roughness parameter was determined from AFM measurements to be approximately 5 nm. The other parameters in the model were adjusted to achieve a best fit that adequately agrees with the raw data. After this initial fit, the layer thicknesses were

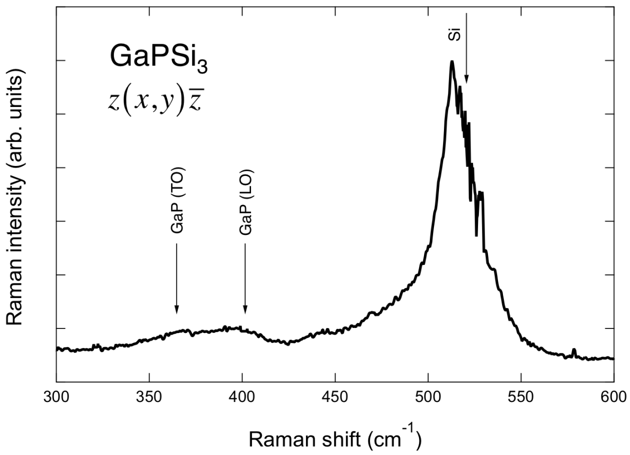

Figure 36: Raman spectrum of a GaPSi$_3$ sample at room temperature, excited with a 532 nm laser line. The Raman peak from the Si-substrate has been subtracted, and the noisy features near 521 cm^{-1} are numerical artifacts related to this subtraction. The scattering configuration is indicated in the Porto notation, with x, y, z being the Cartesian axes directions in the average cubic unit cell.

kept fixed and the data were refit at each wavelength with the values of the real and imaginary dielectric functions, ϵ_1 and ϵ_2, of the GaP-Si layers as adjustable parameters. Figure 37 compares the absorption coefficient, α, calculated from ϵ_1 and ϵ_2 for samples GaPSi$_3$ (green), GaPSi$_6$ (cyan), and GaPSi$_{24}$ (purple) with the absorption coefficients of GaP, crystalline Si, and amorphous Si. The ϵ_1 and ϵ_2 curves from 1.0 to 6.2 eV for a representative GaPSi$_6$ sample are shown inset in the figure. For photon energies below 4 eV, the absorption coefficients are generally within the range defined by GaP and amorphous Si. For photon energies above 4 eV, the GaP-Si samples show enhanced absorption, approaching or even surpassing that of amorphous Si. In the visible region, note the GaP-Si samples show greater absorption than crystalline Si, but lower than amorphous Si. In general the absorption profiles are relatively featureless and akin to amorphous Si, in contrast to crystalline Si and GaP. This is consistent with the notion that the Si lattice in the alloys is perturbed by the substitution of isolated GaP pairs randomly distributed within the crystalline tetrahedral network.

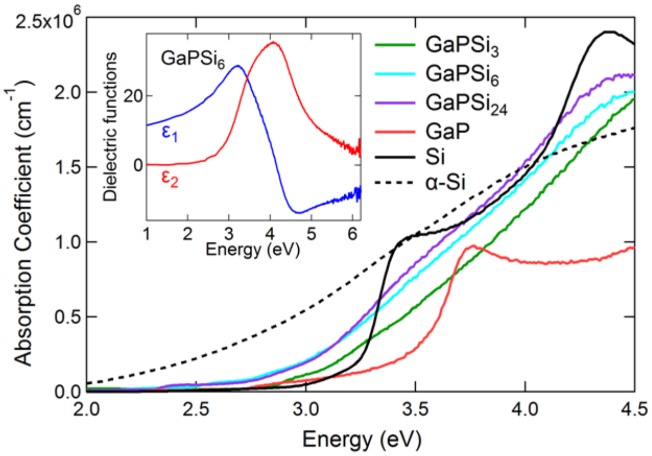

Figure 37: Absorption Coefficients of GaPSi$_3$ (green) GaPSi$_6$ (cyan) and GaPSi$_{24}$ (purple) are compared with those of GaP (red), crystalline Si (black), amorphous Si (dashed) reference. GaPSi$_3$ exhibits intermediate absorption coefficients to GaP and Si in the UV region, as expected. The Si-rich derivatives show stronger absorption with increasing Si content across much of the energy range extending into the visible portion of the spectrum. Inset shows a point-by-point fit of the dielectric function for GaPSi$_6$

4.4 Conclusions

A new series of (III-V)-(IV) semiconductors in the Ga-P-Si system have been synthesized and the crystal growth process theoretically studied using quantum chemical simulations. The materials are grown as epitaxial films using reactions of molecular hydrides $[(D/H)_2GaN(CH_3)_2]_2$ and $P(SiH_3)_3$ as the sources of Ga and P-Si building blocks, respectively. These compounds enable low temperature growth of metastable compositions and structures which cannot be obtained by conventional routes including molecular beam epitaxy. The experiments in this study produced stoichiometric $GaPSi_3$ films and Si-rich derivatives with tunable Si contents spanning the $GaPSi_6$ to $GaPSi_{24}$ range depending on the reaction conditions. All films were found to be almost perfectly lattice-matched to Si substrates. Spectroscopic ellipsometry measurements of the films showed strong absorption in the visible portion of the spectrum, indicating possible applications as solar cell absorbers for high efficiency Si-based photovoltaic devices.

Chapter 5

SYNTHESIS OF $(GaAs)_YGe_{5\text{-}2Y}$ ALLOYS GROWN ON $Ge_{1\text{-}X}Si_X$ BUFFERED Si(100) PLATFORMS

This chapter represents a manuscript draft prepared to be submitted to a peer-reviewed journal with co-authors: Wallace, P. M.; Xu, C.;Menéndez, J.; Kouvetakis, J. with Sims, P. E. as first author. Permission has been obtained to use the content of the manuscript in this dissertation. The author would like to acknowledge Dr. Charutha Lasitha Senaratne for his help with literature review and writing part of this introduction.

Synopsis

In this chapter, the growth of high quality $(GaAs)_yGe_{5\text{-}2y}$ alloys upon $Ge_{1\text{-}x}Si_x$ buffered Si substrates is described. Alloys within this system were grown via reactions of $[D_2GaN(CH_3)_2]_2$, described previously, and highly reactive $As(GeH_3)_3$ serving as the source of As and Ge atoms. This strategy has led to the directed synthesis of alloys containing isolated GaAs pairs embedded in a Ge matrix. The similar lattice parameters between GaAs and Ge allowed for bandgap engineering of systems at a fixed lattice dimension.

The success of this system is based on the availability of highly reactive Ga atoms which readily react with the group-V coreactant, forming the desired III-V-IV_3 tetrahedral core. The molecular gallane approach was first employed in the synthesis of the $GaPSi_3$ prototype described in Chapter 4. The generation of reactive Ga atoms, which subsequently react with $As(GeH_3)_3$ has allowed for the targeted synthesis of $(\mathrm{GaAs})_y\mathrm{Ge}_{5\text{-}2y}$ alloys. Ga-As-Ge systems exhibit a large negative bowing of the bandgap, granting access to applications in the, increasingly topical, mid-IR for civilian and military use. This synthetic approach has yielded optical materials lattice matched to Ge, showing strong PL with wavelengths in the vicinity of 2 μm.

5.1 Introduction

Alloys between elemental semiconductors and compound semiconductors have been investigated for several decades as a route to obtaining new materials with useful optical and electrical properties.[89] One particular area of interest is combining the group-IV and III-V materials on the same row of the periodic table to achieve band gap engineering as a function of composition while maintaining a constant lattice parameter.

An example of such a material is the $(\mathrm{GaAs})_{1\text{-}x}\mathrm{Ge}_{2x}$ alloy, which has been investigated as a candidate material for four-junction solar cells fabricated on Ge. These devices can surpass the efficiency of state-of-the art three-junction solar cells by the addition of a subcell with a band gap near 1 eV, intermediate between the band gaps of Ge and GaAs.[23] Since the alloy has essentially the same lattice constant as the Ge substrate, it can be grown without generating mismatch-induced dislocations, while the composition can be independently tuned to obtain the desired band gap.[13,22] In addition, $(\mathrm{Ge}_2)_{1\text{-}x}(\mathrm{GaAs})_x$ is of interest in understanding the fundamental physics of heterovalent semiconductor alloys. For instance, this system exhibits a significant negative bowing in the band gap, which drops precipitously from 1.4 eV ($x = 0$) to 0.5 eV at $x \sim 0.3$ and then rises more slowly to reach the Ge value 0.8 eV at $x = 1$.[13,22]

This unusual asymmetry has been attributed by Newman et al. to the existence of an order-disorder phase transition arising from the arrangements of the diamond cubic and zincblende constituents in the crystal.[12,13] However, Holloway and Davis contend that much of the bowing calculated by Newman et al. is due from the presence of "wrong" As-As and Ga-Ga bonds in their model, which are unlikely to exist.[15] Holloway and Davis propose an alternative model in which Ga and As atoms are incorporated exclusively as Ga-As dimers, and that As-As and Ga-Ga bonds are forbidden. This model also predicts an asymmetric negative bowing, albeit not as "V-shaped" as calculated by Newman et al. More recent ab initio work has shed some light into the origin of the bowing at its asymmetry. Kawai et al. show that the band gap decrease relative to a linear interpolation between the end compounds is proportional to the concentration of "bad" Ga-Ge and As-Ge bonds. However, the introduction of Ge clusters in GaAs matrices has a larger effect than the introduction of GaAs clusters in Ge matrices, leading to the bowing asymmetry.[90] In addition the indirect gap becomes negative within this range, indicating the emergence of a unique electronic structure that may enable new optical functionalities.

The growth of high quality $(\mathrm{Ge_2})_{1\text{-}x}(\mathrm{GaAs})_x$ alloys is necessary to investigate the practical applications of this system, and to better understand the theoretical aspects. However, achieving this objective is complicated by the fact $(\mathrm{Ge_2})_{1\text{-}x}(\mathrm{GaAs})_x$ alloys are metastable, and show a tendency to phase segregate into the Ge and GaAs constituents during deposition.[23] Furthermore, anti-phase domains have been observed in epitaxial films grown on GaAs wafers.[91] Despite these difficulties, a variety of techniques including molecular beam epitaxy (MBE), metal-organic chemical vapor deposition (MOCVD), and sputtering of solid sources, have been used for the synthesis of these materials.[22,23,31,91–93] These methods have allowed the preliminary investigation of the properties of $(\mathrm{Ge_2})_{1\text{-}x}(\mathrm{GaAs})_x$ including the band gaps using absorption measurements.

Interestingly, no light emission has been reported to date in the (GaAs)1-xGe2x system in spite of efforts to optimize structural design and refine materials quality. This indicates that a fresh synthetic strategy is warranted that would allow precise control of bonding arrangements at the atomic scale to obtain structures and compositions that show photoluminescence. This would ensure that the new materials are viable semiconductors for practical applications in optoelectronics.

Recently a new approach was introduced for synthesizing (III-V)-IV alloys which makes use of precursors of the type $M(LH_3)_3$ (M = P, As, Sb; L = Si, Ge) which have preformed V-IV bonds. The initial prototype synthesized in this manner was $AlPSi_3$, which was assembled using gas phase reactions of molecular $P(SiH_3)_3$ and an Al atomic beams which furnish the constituent elements of the alloys.[25] The unique feature of this approach is that the reactions produce $AlPSi_3$ building-blocks with tetrahedral structures which are then incorporated intact into the crystal in a manner that introduces isolated Al-P pairs within the Si lattice. This arrangement prevents AlP and Si separation leading to homogeneous single phase materials with an average diamond-like structure. The same concept was used thereafter to synthesize entire new families of (III-V)-IV alloys such as $Al(As_{1-x}P_x)Si_3$, $(InP)_xGe_{5-2x}$, etc.[27–30] More recently, gas-source precursors were used for the delivery of group-III atoms, resulting in the synthesis of alloys in the $(Al_{1-x}B_x)PSi_3$ and $(Al_{1-x}B_x)AsSi_3$ systems.[55] Overall, the use of $M(LH_3)_3$ precursors has proven to be a versatile method for the synthesis of hybrid (III-V)-IV alloys yielding a wide range of potentially practical semiconductors that cannot be obtained by conventional routes.

This chapter is description of the use of $As(GeH_3)_3$ in combination with the $[D_2GaN(CH_3)_2]_2$ molecular source of Ga to synthesize epitaxial $GaAsGe_3$ films. These were produced using $Ge_{1-x}Si_x$ buffer layers (x = 0.12-0.15) which closely lattice match the alloy epilayers allowing the formation of single-phase monocrystalline layers exhibiting strong PL with emission wavelengths close to the absorption edges detected in prior work on the $(Ge_2)_{1-x}(GaAs)_x$ system.

5.2 Experimental

5.2.1 Precursor Selection

Conventional gas-source precursors used for MOCVD of Ga based III-V semiconductors are the classic trimethyl- and thiethyl-gallium metalorganics and related trialkyl derivatives.[94–96] Gallium hydride analogues containing multiple Ga-H bonds in place of Ga-C are more desirable for low temperature processing. The higher reactivity and facile elimination of stable byproducts, which do not participate in the reaction process, lead to the formation of high purity materials. Dimethylamido-gallane $[D_2GaN(CH_3)_2]_2$ was previously used to deposit Ga-P-Si alloys, devoid of N and C impurities, under metastable conditions as required for the current application. The compound is a volatile liquid, with approximately 1 Torr vapor pressure at room temperature, and remains stable for extended periods, making it an attractive candidate for low-pressure epitaxy-driven synthesis. Furthermore, the thermal dissociation proceeds via formation of thermally robust $DN(CH_3)_2$ and D_2 byproducts yielding pure Ga atoms, which readily react on the substrate surface under MBE-like conditions, to produce crystalline films. The compound was produced and purified by distillation using literature methods.[78,79] The $As(GeH_3)_3$ co-reactant was prepared by direct combination Li_3As and $ClGeH_3$ in diethyl ether and purified to obtain semiconductor grade reagent as described by Xu et al.[97] $As(GeH_3)_3$ is a volatile liquid exhibiting a comparable vapor pressure, ~1 Torr and a similar reactivity to $[D_2GaN(CH_3)_2]_2$. Thus enabling direct combinations; leading to stoichiometric Ga-As moieties in the final product. $[D_2GaN(CH_3)_2]_2$ was chosen rather than the more conventional isotopic analogue $[H_2GaN(CH_3)_2]_2$ because it is more robust, this is due to the higher kinetic stability of Ga-D bonds. This added stability ensures equivalent reactivity with $As(GeH_3)_3$, as mentioned above, and better control of the reaction rate under the low-pressure and low-temperature growth conditions employed. It is envisioned the reaction mechanism involves the formation of $Ga{\cdot}As(GeH_3)_3$ intermediates which eliminate H_2 yielding the desired $GaAsGe_3$ building-blocks. These building-blocks are comprised of a central As atom surrounded by one Ga and three Ge atoms. Subsequently, these interlink to generate an extended diamond-like structure similar to that described in Watkins et al for $AlPSi_3$.[25] This synthesis mechanism is described by the following reaction scheme:

$$\mathrm{Ga} + \mathrm{As(GeH_3)_3} \rightarrow \text{"}\mathrm{Ga{\cdot}As(GeH_3)_3}\text{"} \rightarrow \tfrac{9}{2}\mathrm{H_2} + \mathrm{GaAsGe_3} \tag{5.1}$$

While the ideal buffer for this application is pure Ge due to near perfect lattice matching with Ga-As-Ge, here $Ge_{0.87}Si_{0.13}$ was used with a slightly smaller lattice constant. This allows clear separation of the XRD peaks between the epilayer and the buffer which in turn ensures unambiguous measurement of the lattice dimensions and strain states of the films. The $Ge_{0.87}Si_{0.13}$ buffers are grown on 4” Si(100) wafers via reactions of Si_4H_{10} and Ge_4H_{10}, using gas source molecular epitaxy at 380 °C. The resultant films exhibited flat surfaces and large thicknesses, up to ~1500 nm, making them suitable platforms for subsequent epitaxy. The Ga-As-Ge samples were grown in a separate single-wafer chamber described elsewhere in detail.[55] The $Ge_{0.87}Si_{0.13}$/Si substrates are 1.0×1.5 cm^2 segments cleaved from the 4” buffered wafers to fit the wafer stage in the chamber. Prior to growth the substrates were dipped in an aqueous

HF (5%) bath for three minutes to remove the surface oxide and then rinsed with methanol/water and dried under a stream of UHP nitrogen. Immediately thereafter the substrates were mounted on the sample stage using molybdenum clips and inserted into the reactor through a load-lock kept at 10^{-8} Torr. They were heated to 650 °C on the sample stage under dynamic pumping to degas the material and remove the hydrogen passivation from the surface. As indicated above bare silicon substrates were also used for direct deposition of the films. These were flashed on the sample stage at 1050°C ten times for 10 seconds each time to remove the oxide layer and generate an epi-ready surface. Prior to growth a thin silicon buffer layer was grown on the wafer surface at 540 °C using 10% tetrasilane (Si_4H_{10}) in UHP hydrogen.

5.2.2 Materials Growth

The $[D_2GaN(CH_3)_2]_2$ and $As(GeH_3)_3$ gaseous sources were fed separately into the chamber using UHV-compatible needle valves to regulate the flow; the precursors were delivered onto the growth surface through a nozzle positioned 1 inch away from the substrate. This arrangement prevents premixing of the gases, an effective strategy to avoid side reactions that may adversely effect the stoichiometry of the films. Initially a 3-fold excess of $As(GeH_3)_3$ relative to $[D_2GaN(CH_3)_2]_2$ was used to ensure the entire Ga flux was consumed, leading to stoichiometric Ga:As amounts into the films. Nevertheless, exact GaAs compositions could also be produced using stoichiometric reactions involving 1:1 combinations of the co-reactants. Although a reduction in the growth rate was observed the resultant materials exhibited comparable crystallinity and optical properties to the analogues produced using an excess of $As(GeH_3)_3$, indicating the reaction pathway is reproducible and tractable. The total deposition pressure, in all experiments, was kept at 1.0×10^{-5} Torr using dynamic pumping provided by a process turbo-pump. Under the above conditions a series of samples were produced using substrate temperatures from 400 °C-600 °C.

5.3 Results and Discussion

5.3.1 Compositional and Structural Analysis

The films initially produced at 400 °C on $Ge_{0.87}Si_{0.13}$ buffer layers were thin and lacked long range crystallinity, indicating the temperature is too low for viable crystal assembly. In contrast, monocrystalline layers with significant thicknesses, above 200 nm, were deposited at 450 °C with a growth rate of ~14 nm/minute. The film thickness was determined by ellipsometry and RBS measurements. A representative RBS spectrum, collected at 2.0 MeV can be seen in Figure 38 showing the thick buffer layer and the GaAsGe overlayer. The experimental spectrum is shown in black, the data modeled, using the RUMP software package, as $GaAsGe_3/Ge_{0.87}Si_{0.13}/Si(100)$ is shown in red, and the channeled spectrum is shown in blue. However, the RBS signals of Ga, Ge, and As overlap with each other due to the similarity in atomic number. This renders RBS as a technique suitable for determination of thickness and assessment of the epitaxial alignment. This sample has a thickness of 210 nm and the buffer layer is found to be 1290 nm. The channeling spectrum shown in blue indicates all of the elements occupy a common diamond-like lattice and are fully coherent with the underlying template. Since the determination of exact composition is non-trivial in this case, proton induced X-ray emisssion (PiXE) was used to ensure all three elements were present in the films. In all of the samples examined the Ga:As ratio was found to be ~1:1 as expected, but due to the presence of Ge in the buffer layer quantification was impossible. Secondary ion mass spectrometry (SIMS) depth profiles confirmed the presence of all the constituent elements and showed uniform profiles throughout the layers.

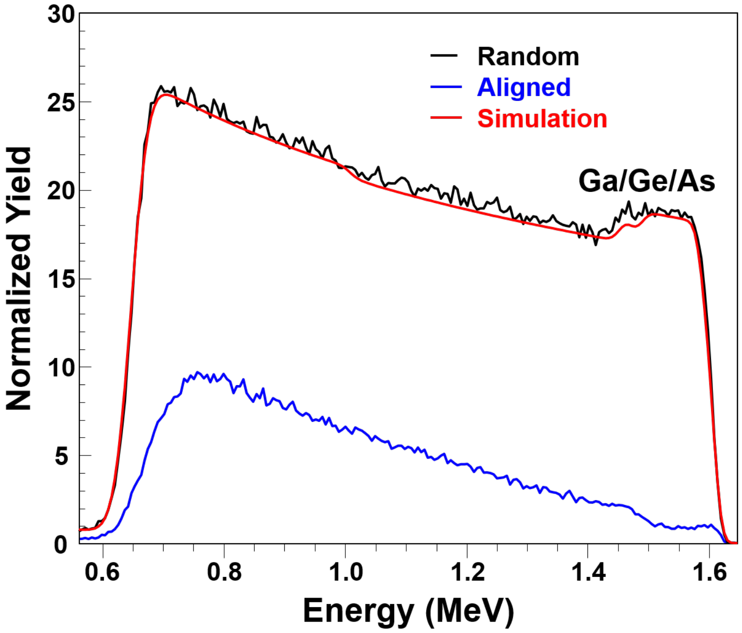

Figure 38: Random RBS spectrum (black) of a typical Ga-As-Ge alloy grown on $Ge_{0.87}Si_{0.13}$ buffered Si showing the close proximity of the signals for Ga, As, and Ge. A simulated spectrum is shown (red) and was used to determine a thickness of 210 nm. The channeled spectrum (blue) shows a high level of epitaxial alignment between the epilayer and buffer–substrate template and indicates that all of the elements occupy a common lattice.

Further efforts to determine the absolute concentration utilized EDX analysis of cross sectional TEM samples. In this configuration the epilayer and the buffer are clearly delineated allowing an unambiguous determination of the film composition. An FEI Titan 80-300 transmission electron microscope (TEM) operated at 300 kV was used to collect the spectra from various nanoscale regions across the epilayer. These regions ranged in size from 20-200 nm in diameter in the lateral direction. A typical spectrum shows the characteristic k-lines for the three elements allowing fitting of the data using ES-Vision software incorporating known parameters of the emission lines. The analysis consistently yielded an approximate composition of $GaAsGe_4$ (66% Ge). Given the uncertainty in the measurement this is close to the $GaAsGe_3$ (60% Ge) stoichiometry on the basis of intact incorporation of the $GaAsGe_3$ molecular cores in the crystal.

An objective of the work is to study the dependence of the Ge content on the band gap which as indicated above is predicted to remain constant over a broad range of compositions. In the case of $AlPSi_3$ the Si content could be systematically increased above the 60% threshold by increasing the growth temperature yielding alloys with compositions up to 90% Si.[26] This was attributed to the independent decomposition of the $P(SiH_3)_3$ compound at higher temperatures leading to Si rich films. It is expected the more reactive $As(GeH_3)_3$ should exhibit a similar behavior. Accordingly a series of samples were then grown at 500 °C, 550 °C 600 °C to investigate the influence of the deposition temperature on the Ge content. The growth rate increased from 15-18 nm/minute as a function of temperature. These growths yielded monocrystalline films with thicknesses up to 300 nm and beyond allowing facile determination of their bulk properties. These materials were subjected to analysis by RBS, SIMS, PiXE, and EDX; the results revealed the Ge content increased systematically with temperature while the GaAs content remained stoichiometric. A thorough analysis of cross sectional TEM specimens using EDX for the 600 °C sample gave an approximate composition of $GaAsGe_8$ which corresponds to 80% Ge, 10% As and 10% Ga. Collectively the analysis trends across the series of samples from 450 °C-600 °C indicate the Ge content increases monotonically from 60-80%.

XRD experiments were performed to measure the lattice constants and determine

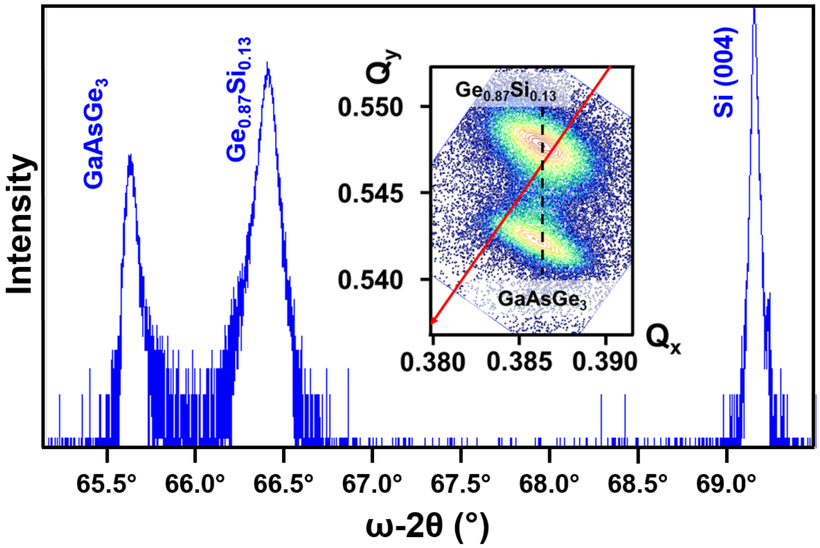

Figure 39: High-resolution XRD spectra from a GaAsGe$_3$ sample grown on a Ge$_{0.87}$Si$_{0.13}$ buffered Si substrate at 450 °C. The ω-2θ plot shows the (004) peaks of the alloy, buffer layer, and substrate indicating a common diamond-cubic structure in all materials. Inset: corresponding (224) reciprocal space map illustrating pseudomorphically strained (GaAs)$_y$Ge$_{5\text{-}2y}$ epilayer on Ge$_{1\text{-}x}$Si$_x$ buffer as evidenced by the vertical alignment of the peak maxima along the dotted line.

the strain states of the films as a function of composition and growth conditions. The samples were found to be monocrystalline and epitaxial as evidenced by the presence of sharp on-axis (004) peaks and well-defined reciprocal space maps. Figure 39 shows high-resolution XRD measurements of a 450 °C film showing distinct peaks corresponding to the GaAsGe$_3$ epilayer, Ge$_{0.87}$Si$_{0.13}$ buffer layer and Si wafer as expected for a crystalline heterostructure aligned with the Si wafer. The (224) reciprocal space maps show a close vertical correspondence of the epilayer maximum with that of the buffer along the pseudomorphic line indicating that the two materials are fully strained. The in-plane and vertical lattice dimensions were measured to be $a = 5.6416$ Å and $c = 5.6836$ Å. Using these values and linear elasticity theory the cubic lattice constant was determined to be $a_0 = 5.6652$Å which is slightly larger that those of bulk GaAs (5.653 Å) and Ge (5.658 Å). The XRD data of the 500 °C alloy showed partial relaxation with the in plane compressive strain decreasing to -0.3287% from -0.4095% for the 450 °C analogue. Using the measured $a = 5.6440$ Å and $c = 5.6772$ Å for this material, the cubic parameter was determined to be 5.662 Å. A similar $a_0 = 5.6628$ Å value was determined for the 550 °C sample using the measured $a = 5.6559$ Å and $c = 5.6684$ Å lattice constants. As expected the strain in this case is further reduced to a residual level of -0.1219% indicating that the material is mostly relaxed. Finally the 600 °C film was found to be virtually relaxed exhibiting negligible strain, as illustrated in Figure 40 inset which shows the alloy peak maximum coinciding with the relaxation line (red arrow). The cubic parameter for this material was measured to be $a_0 = 5.6616$ Å which is slightly larger than Ge and GaAs as in all the above samples. The overall trend is that the compressive strains of the films decrease with increasing temperature culminating with full relaxation as expected at the high temperature end.

The close similarity in a_0 for all the above four samples with varying Ge contents from ~64-80% indicated that the dependence of concentration on the lattice constant vs. temperature could not be unambiguously established due to the very close correspondence of the GaAs and Ge cell dimensions. In particular, the parameters of several Ge samples with 64% to 66% Ge content fall within the narrow range of 5.6652-5.6682 Å. The latter are slightly larger than the 5.660 Å to 5.662 Å values of Ge-rich analogues with Ge compositions of 70% and 80%, respectively.

As indicated above, the lattice constants of all samples irrespective of Ge content are larger than both Ge and GaAs indicating a definite positive deviation from linear interpolation between the end members. This trend may be attributed to differences of the short range structures and the local bonding arrangements associated with the

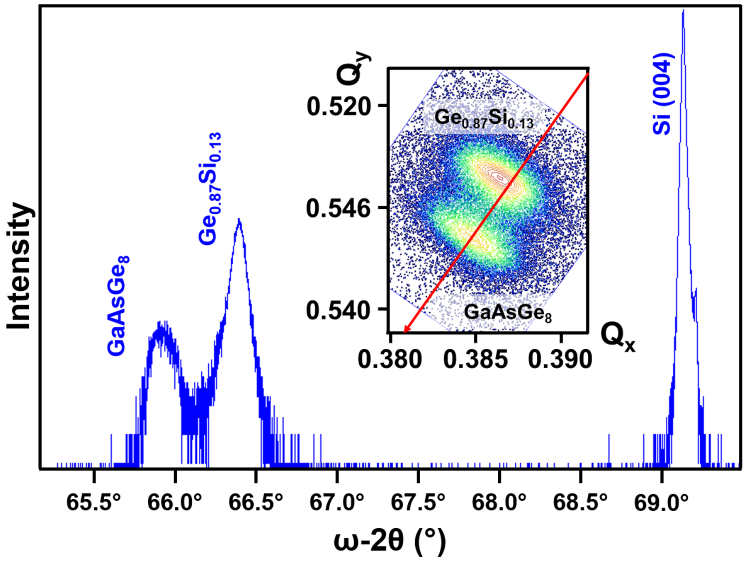

Figure 40: High-resolution XRD spectra from a $GaAsGe_8$ sample grown on a $Ge_{0.87}Si_{0.13}$ buffered Si substrate at 600 °C. The ω-2θ plot shows distinct (004) alloy peaks for both the $GaAsGe_8$ system and the buffer layer, both are in the vicinity of the Si(004) reflection. Inset: the (224) reciprocal space map reveal a strain-free epilayer (relaxation line passing through the center of the alloy peak), and a slightly tensile strained buffer.

incorporation of the $GaAsGe_3$ units into the parent Ge matrix. A similar explanation is provided in theoretical studies of the various $(Ge_2)_{1\text{-}x}(GeAs)_x$ alloys described in Giorgi et al. and Kawai et al. where significant positive bowing is found depending on the specific structural motifs used in the calculations.[17,90]

5.3.2 Structural Description and Thermodynamic Considerations from Theoretical Simulations

To gain insights into the proposed mechanism for the assembly of $GaAsGe_3$ via interlinking $GaAsGe_3$ building-blocks and further elucidate the diffraction trends described above, the crystal structure of the stoichiometric $GaAsGe_3$ material using density functional theory (DFT) was calculated. The Quantum ESPRESSO (QE) package was employeed and performed geometric optimizations and total energy calculations of the ground state structure akin to that of the $AlPSi_3$ phase reported in prior work.[25,87] The generalized gradient approximation (GGA) optimized for solids (PBEsol) was applied in this case along with ultrasoft pseudopotentials.[98] The structural parameters were optimized until the atomic forces and stresses were reduced below 0.02 eV/Å and 1.0×10-4 eV/Å^3, respectively.

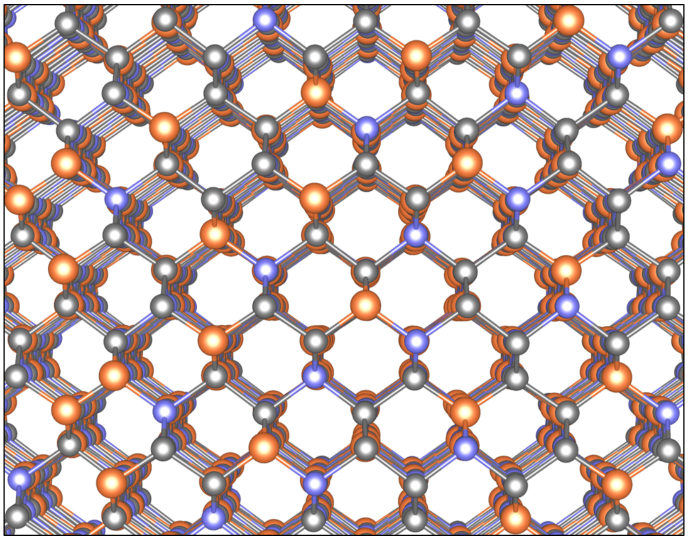

Figure 41: Structural model of the $GaAsGe_3$ lattice in [110] projection showing the dimers or "dumbbells" of the diamond-like structure.

The main outcome of the simulations is that the typical perturbation induced by the insertion of periodic III-V pairs into the group-IV matrix is negligible for this material. Figure 41 shows the fully relaxed, structure with 10-atom unit cell description in which the Ga-As pairs are orientationally aligned to form the ground state ordered phase. The figure illustrates the [110] equivalent direction containing the “dumbbell” pattern of the average diamond cubic lattice. No visible deviations or distortions from normal tetrahedral geometry are seen along this projection due to the close similarity of Ga-As and Ge-Ge bond lengths.

The ground state structure for this system is found to be monoclinic with C1c1 symmetry. The cell parameters are $a = b = 8.9898$ Å, $c = 5.7063$ Å, $\alpha = \beta = 90°$, and $\gamma = 90.04°$ indicating near orthogonal geometry. The atomic positions are given in Table 4. Using these structural parameters the cubic equivalent lattice constant of the monoclinic structure is calculated to be 5.6925 Å which is slightly larger by 0.45% than the average experimental value 5.6667 Å of $GaAsGe_3$ determined by XRD. The lattice constants for the GaAs and Ge end members were also calculated and found to be 5.6720 Å and 5.6797 Å using the same theoretical framework. These values are also slightly larger than the experimental counterparts by 0.34% and 0.38%, respectively. These trends are consistent with the XRD finding above for the Ga-As-Ge samples indicating close agreement between theory and experiment.

Table 4: Ground state atomic positions for $GaAsGe_3$ determined using DFT.

$GaAsGe_3$	
	Atomic Positions
Ga (4a)	-0.82409, 0.02815,0.37878
As (4a)	-0.52592,-0.57355,0.13043
Ge1 (4a)	-0.13041, 0.63161,0.13196
Ge2 (4a)	0.07254, 0.22123,0.12421
Ge3 (4a)	-0.73023,-0.16930,0.11894

The regularity of the $GaAsGe_3$ phase is further demonstrated in Figure 42 which shows a representative Ga-As-Ge_3 tetrahedral unit extracted from the ground-state structure of the material. The difference between the Ga-As (2.488 Å) and As-Ge (2.479±0.001 Å) bond lengths, shown in the annotated models, are small, as expected. This leads to the creation of a near regular tetrahedron exhibiting virtually identical apical and basal edges of 4.051±0.018 Å and 4.047±0.069 Å, respectively, indicating the creation of a spontaneously organized lattice devoid of destabilizing bonding strains. This is corroborated by thermodynamics considerations using the calculated static lattice energies. The latter show that $GaAsGe_3$ crystal is stable with respect to the constituent elements Ga, As, and Ge by ΔE/atom = -44 meV and only slightly metastable by +81 meV/atom relative to GaAs and Ge components and in excellent agreement with prior DFT work by Chizmeshya et al.[99] Collectively these results reveal that the formation of crystalline single-phase alloys is feasible under the kinetically favored conditions afforded by this epitaxy driven synthesis method. The use of preformed bonding configurations in the starting materials alleviates phase segregation issues associated with prior synthetic efforts based on conventional MBE and MOCVD routes.

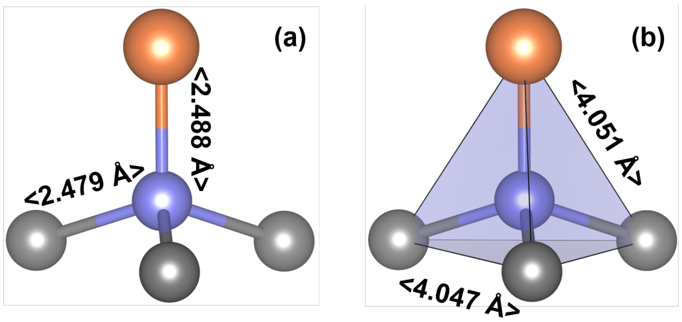

Figure 42: (a) Tetrahedral unit extracted from the calculated structure showing the average bond lengths. (c) Polyhedral representation of the extracted tetrahedron showing the apical and basal edge lengths.

5.3.3 Microstructure of $GaAsGe_3$ and Ge-rich Analogues

Further structural investigations were performed by XTEM using the same FEI Titan electron microscope desribed above, again operated at 300 kV. Figure 43 shows representative images of the $GaAsGe_3$ alloy grown on $Ge_{0.87}Si_{0.13}$ at 450 °C. The diffraction contrast representation in the top panel shows the full heterostructure illustrating a flat surface and a uniform interface marked by the arrow. The homogeneous contrast corroborates the monocrystalline character of the film and further illustrates the phase purity of the crystal. The phase inhomogeneities in this class of hybrid alloys are typically manifested in the form of vertical striations arising from compositional variations in the crystal. The images in the figure also reveal the defect microstructure. While the upper segment of the epilayer is mostly defect-free occasional dislocations are observed in the lower portion. These originate from the originally defected buffer and cross a short distance into the epilayer. The bottom panel is a high resolution view of the interface illustrating complete alignment of the $\{111\}$ lattice planes as expected for a fully coherent stack devoid of dislocations within the field of view.

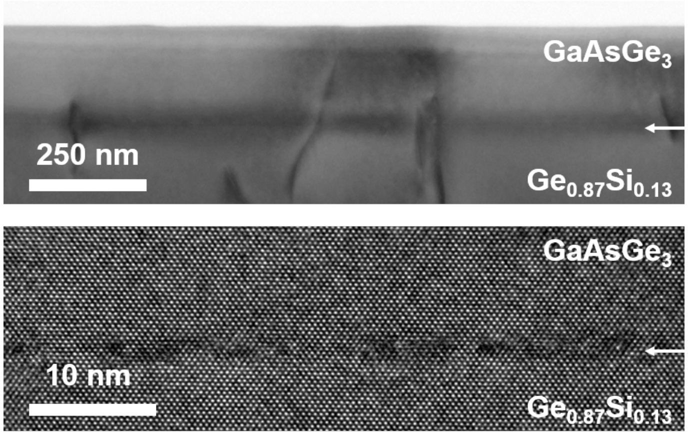

Figure 43: XTEM images of $GaAsGe_3$ grown on $Ge_{0.87}Si_{0.13}$ buffer at 450 °C. (top) Low-magnification image of $GaAsGe_3$ film and buffer layer revealing a single phase material with several defects penetrating through the common interface. (bottom) High-resolution view of the interface illustrating the epitaxial nature of the growth.

Figure 44 (top) shows a diffraction contrast image of the $GaAsGe_8$ alloy grown at

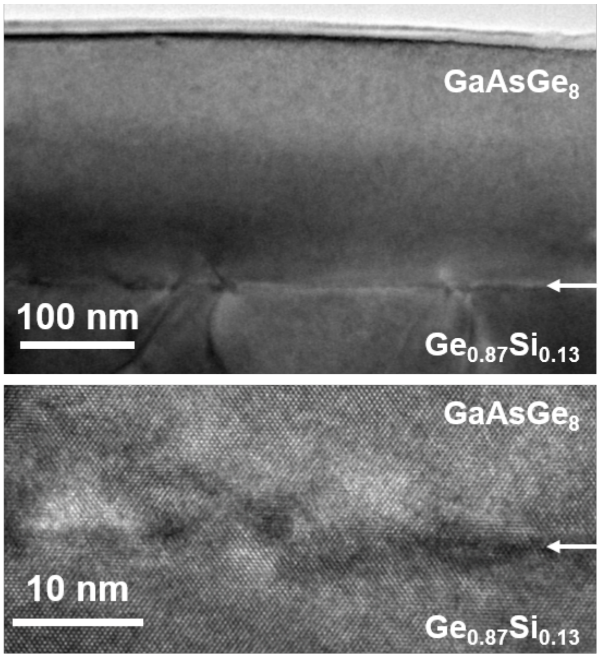

Figure 44: XTEM images of GaAsGe$_8$ grown on Ge$_{0.87}$Si$_{0.13}$ buffers at 600 °C. (top) Low magnification diffraction contrast image of the GaAsGe$_8$ sample showing the epilayer and the buffer. Defects in this material are confined to the interface region indicating the strain relaxation occurs through generation of edge dislocations. (bottom) High magnification image of the interface showing the registry between the Ga-As-Ge alloy and the underlying buffer layer.

600 °C corroborating the Ge-like character of the Ge-rich material. The bulk layer is uniform and featureless due to the single-phase nature of the crystal. The bulk material is defect free and devoid of features associated with phase segregation and related structural flaws within the field of view. However, several defects are visible near the interface region. These also originate from the buffer and penetrate into the GaAsGe$_8$ film indicating that the quality of the film can be further optimized by improving the buffers grown on Si. High resolution images of this sample (Figure 44 bottom) reveal relaxation induced dislocations confined to the interface plane. These accommodate the lattice mismatch between the alloy and the buffer, consistent with

the full relaxation seen in the XRD plots of this material. Collectively the electron microscopy and XRD data provide strong proof that the films are homogeneous alloys and not mixtures of impurity phases. This is a testament to the new synthetic approach based on specifically designed reactions that allow control of composition and bonding at the atomic scale leading to the fabrication of homogeneous phases that exhibit photoluminescence for the first time. As indicated above this conclusion is supported by the lack of striations and related features such as domains and ribbons exhibiting contrast variation due to phase separation issues described in Norman et al.[23]

5.3.4 Bonding Properties Using Raman

Figure 45 shows representative Raman spectra obtained from the $GaAsGe_n$ samples compared with Raman spectra from bulk Ge and GaAs. Pure Ge has a single Raman mode with a shift of 300.3 cm^{-1} at room temperature, whereas the Raman spectrum of GaAs, depending on the scattering geometry, shows has a longitudinal optic (LO) mode at 291.6 cm^{-1} and a transverse optic (TO) mode at 268.7 cm^{-1}.[100] The close proximity of the Ge- and GaAs frequencies, as a result of the very similar masses and lattice parameters, suggests that the $GaAsGe_x$ alloy system will not display a clear segregation into Ge-like and GaAs-like modes, as observed for example in $Ge_{1-x}Si_x$ and $Ga_{1-x}Al_xAs$ alloys.[101] This has already been confirmed in previous work, which shows a mode compositional behavior akin to "one-mode" alloys: a single peak in Ge-rich systems that approaches the bulk Ge frequency in the limit of vanishing GaAs concentration, and two peaks in GaAs-rich systems that approach the bulk GaAs LO and TO modes for vanishing Ge concentration. A significant observation

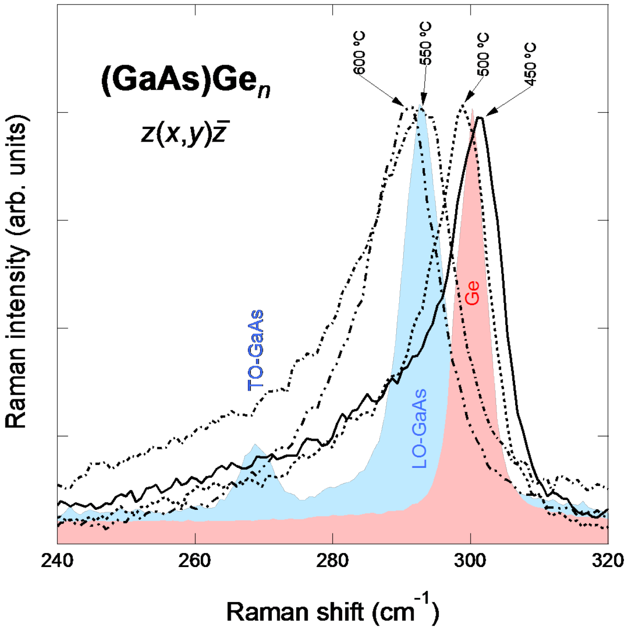

Figure 45: Room temperature Raman spectra of selected GaAsGe$_{\mathrm{n}}$ samples obtained with 532 nm excitation. The blue (red) profile show the corresponding spectra from bulk GaAs (Ge). The scattering configuration is indicated using the Porto notation, with x, y, z being the Cartesian axes in the cubic lattice. For this configuration TO Raman scattering is forbidden in GaAs, and the observed peak is due to polarization leakage.

from prior work is that the frequency of the Ge-like Raman peak in Ge-rich alloys is lower than that of bulk Ge. This is easy to understand if one takes into account that the optical phonon density of states peaks well below the Raman frequency in Ge and the LO-Raman frequency in GaAs.[102] To the extent that the alloy modes are viewed as mixing of optical modes in the end constituents, a frequency lowering is expected, and it also explains the asymmetric broadening to low-energies, which is also clearly noticeable in Figure 45. However, there is a significant difference between prior results and those reported here: the mode frequency decreases as a function of the Ge concentration, as evidenced by the monotonic shift of the peak frequency as a function of the growth temperature in Figure 45. Furthermore, the Raman frequency of the alloys closest to the stoichiometric compound $GaAsGe_3$ are very close to that of bulk Ge, whereas the reported Raman frequency of the compositionally equivalent x = 0.6 $(GaAs)_{1-x}Ge_x$ alloy is about 10 cm^{-1} below that of bulk Ge.[22,103] Furthermore, the full width at half maximum of the Raman peak in the literature is about 20 cm^{-1}, about a factor of 2 higher than the FWHM for the samples grown at 450 °C and 500 °C. Note, on the other hand, that the samples grown at higher temperatures do show a broader, downshifted Raman spectrum in closer agreement with previous experimental work. A possible explanation for these results is that these samples with compositions closest to the stoichiometric $GaAsGe_3$ composition adopt preferentially one or a few of the many possible orderered structures that can be assembled with Ga-As-Ge_3 tetrahedra. In this case, the microscopic atomic arrangement might lead to Raman-active modes with frequencies as high as that of pure Ge. At higher growth temperatures, on the other hand, either the tetrahedra decompose, or they are further and further apart from each other in a predominantly Ge matrix, and therefore any correlation between them is lost. Other optical studies are consistent with this interpretation.

5.3.5 Spectroscopic Ellipsometry and Photoluminescence

Photoluminescence (PL) measurements were performed using a 980 nm, 400 mW light source and an InGaAs mid-IR detector with an absorption cut off at 2300 nm (0.54 eV). The excitation source was modulated using an optical chopper at 191 Hz for lock-in detection (which cuts the incident power in half). A 1400 nm long pass filter was used to remove higher energy peaks from the Si substrate. The spectra were collected using a Horiba micro HR spectrometer and a grating optimized for 2000 nm. An extended InGaAs detector with cutoff wavelength at 2500 nm was used to cover the relevant spectral range allows the entire peak profile of the PL spectrum of the samples to be visible. No PL signal was observed from the samples grown at the higher 550 °C and 600 °C temperatures. This is consistent with the lack of prior PL reports for $(GaAs)_{1-x}Ge_{2x}$ alloys. On the other hand, the samples with the "anomalous" Raman spectrum in Figure 45 do show a PL signal peaking below 0.6 eV. These emission energies are well below any linear interpolation between the direct gaps of Ge ($E_0 = 0.80$ eV) and GaAs ($E_0 = 1.4$ eV) but close to the direct band gaps of $(GaAs)_{1-x}Ge_{2x}$ alloys of similar compositions observed in absorption experiments. As indicated above, recent calculations show that the band gap reduction is directly proportional to the concentration of bad bonds, but with a stronger dependence for Ge clusters in GaAs as opposed to GaAs clusters in Ge.[90] Since the proposed structure for $GaAsGe_3$ consists exclusively of isolated Ga-As dimers, it is then possible that the direct band gap may be somewhat higher for this structure, and represented by the high-energy tail. The presence of two PL peaks could then be do presence of more disorder regions to accommodate the slight Ge excess relative to $GaAsGe_3$, as found experimentally.

The real (ϵ_1) and imaginary (ϵ_2) parts of the film dielectric functions were determined using a JA Woollam™ UV-Vis variable angle spectroscopic ellipsometer using an incident angle of 70° and energy steps of 0.010 eV. The measurements yield the ellipsometric angles $\Psi(E)$ and $\Delta(E)$, which are modeled as a multiple-layer system that includes the substrate, the buffer layer, the doped film itself, and a roughened ($\sim$1-2 nm) GeO_2 layer at the surface. The dielectric function was first adjusted to the data using a parametric model.[104] For this fit the dielectric function for the remaining layers were taken either from ellipsometer manufacturer's database or from prior measurements. In the case of GeO_2 data from Hu et al. was used.[105] The

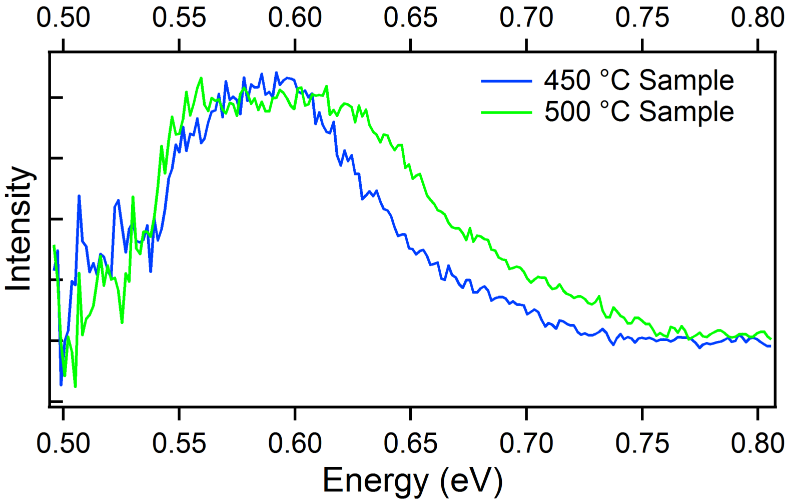

Figure 46: Photoluminescence of GaAsGe$_n$ alloys grown at 450 °C and 500 °C showing a signal which peaks below 0.6 eV. PL data collected and processed by Patrick Wallace.

adjustable parameters of this fit are the layer thicknesses and all constants in the parametric model for the GaAsGe layer. In a subsequent fit stage, the thicknesses from the initial fit is "frozen" and new fits of the dielectric function of the GaAsGe are carried out without assuming any theoretical model. Instead, simply the real (ϵ_1) and imaginary (ϵ_2) parts of the dielectric function are used at each energy as adjustable parameters. The fit values are used as seed parameters for the next energy values, and by following this “point-by-point” procedure, the dielectric function is obtained over the entire energy range. Figure 47 compares the imaginary parts of the dielectric function in the spectral range of the so-called E$_1$ and E$_1$+Δ_1 transitions, which are shown as for Ge and GaAs as shaded profiles. The features are clearly broadened for the GaAsGe samples, without a clear distinction between the two transitions. For all samples, independent of growth temperature, the average energy of the structure does not interpolate between those of Ge and GaAs, and is in fact slightly lower than the Ge energy. Therefore there is also a large negative bowing in the compositional

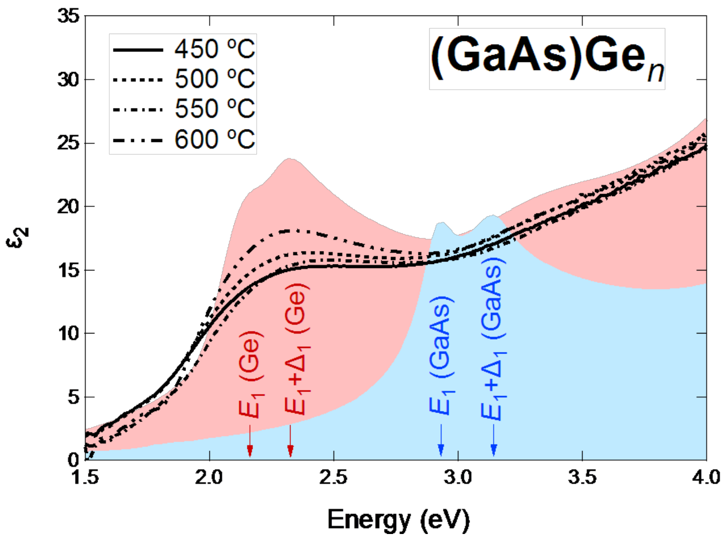

Figure 47: Imaginary part of the dielectric function for selected GaAsGe$_n$ alloys, compared with the corresponding dielectric functions for Ge (red) and GaAs (blue). The dominant features in this energy range are the E1 and E1+Δ1 transitions. It is apparent from the spectra that these transitions also display a strong negative bowing in their compositional dependence.

dependence of these transitions, similar to the one observed for the direct gap. This is in agreement with theoretical calculations.[17] Ellipsometric measurements in the IR range were also performed (not shown). The data can be reasonably well modeled with a Drude expression, indicating the presence of free charges. Unfortunately, the carrier concentration cannot be determined from the experimental data because there is a lack of information about the relevant effective masses. A natural candidate for these excess charges is unintentional doping due to a slight difference in the Ga and As concentrations. However, some calculated band structures for these alloys predict negative indirect band gaps, so that the system might have an intrinsic metallic character that explains the Drude behavior without invoking unintentional doping.[17]

5.4 Conclusions

A new series of heterovalent semiconductor alloys were grown in the GaAs-Ge system using reactions of molecular hydrides, $[D_2GaN(CH_3)_2]_2$ and $As(GeH_3)_3$. Low temperature growth using these compounds allowed the direct integration of these alloys as epitaxial films upon $Ge_{1\text{-}x}Ge_x$ buffered Si platforms generating compositions and structures which are not accessible via traditional synthetic routes. The alloys within this study have tunable Ge contents, depending on the growth temperature employed, from stoichiometric $GaAsGe_3$ to $GaAsGe_8$. In addition to temperature controlled compositions the strain state can be monotonically decreased to achieve a fully relaxed material, also as a function of growth temperature. Raman studies of these alloy films indicates the inherent nature of the building block assembly produces alloys which are distinctly different than those described in the literature and may possess a unique ordered structure. Strong photoluminescence is observed from samples grown at lower temperatures with signals peaking below 0.6 eV external to any linear interpolation between the gaps of GaAs and Ge end-members. The strong bowing observed in the PL measuremnts is corroborated by the bowing seen in the higher energy gaps, E_1 and $E_1+\Delta_1$, as determined by spectroscopic ellipsometry, and in agreement with theoretical predictions.

This Page Intentionally Blank

Chapter 6

STRUCTURAL PROPERTIES OF (III-V)-IV_3 ALLOYS FROM QUANTUM CHEMICAL SIMULATIONS

6.1 Introduction

Materials science is an interdisciplinary field, and no area more so than exploratory synthesis. Directed design of materials is an interplay between experiment and theory. Experimental exploration of hybrid (III-V)-IV_3 alloys can be complimented through the use of quantum chemical simulations. Though there has been success in light of the synthetic strategies developed, these results are just the beginning. The number of phases realized since the advent of the tetrahedral building-block approach developed by Watkins et al. pales in comparison to those possible.[25] The first part of this chapter focuses on the structural and thermodynamic properties of the lattice matched $AlPSi_3$, $GaPSi_3$, and $GaAsGe_3$ systems which have been previously synthesized and described in Chapters 3, 4, and 5, respectively. To explore how structural changes affect materials properties, alloys containing boron have also been considered. The boron containing (III-V)-IV_3 systems discussed in the latter portion of this chapter include a lattice matched BNC_3 alloy, and alloys in which the III-V pair causes a large perturbation to the lattice: $BNSi_3$, BPC_3, and $BPSi_3$. The $BNSi_3$ and $BPSi_3$ systems demonstrate the effects of incorporating a small III-V unit within the group-IV matrix. In contrast, the BPC_3 system was considered to study the opposite regime where the III-V component is much larger than the replaced IV-IV pair. Additionally, the data serve as a guide to aide in the realization of small atom (III-V)-IV_3 analogues which may have interesting properties. In particular, the latter four phases may have application as superhard materials, exhibit high thermal conductivity, and the incorporation of significant amounts of boron portends application in neutron detection.

6.2 Computational Methodology

Within the framework of DFT the Quantum ESPRESSO (QE) package was used for all geometry optimization, total energy calculations, and determination of energy-volume (E-V) relationships.[87] Structural parameters were converged to achieve atomic forces less than 1.0×10^{-3} eV/Å, and cell stresses less than 1.0×10^{-4} eV/Å^3 with respect to k-point integration, and kinetic energy cutoffs for wavefunctions, potentials, and densities. All calculations were done using ultrasoft pseudopotentials in the local density approximation (LDA) described by Perdew and Zunger.[106] The bulk moduli of the following: C-diamond, Si, cubic-BN, BP, BNC_3, $BNSi_3$, BPC_3, and $BPSi_3$ were determined. This was achieved by fitting the E-V data using the 3rd-order Birch-Murnaghan equation of state (BM-EOS):

$$E(V) = E_0 + \frac{9}{8}B_0V_0\left[\left(\frac{V_0}{V}\right)^{\frac{2}{3}} - 1\right]^2 + \frac{9}{16}B_0\left(B_0' - 4\right)V_0\left[\left(\frac{V_0}{V}\right)^{\frac{2}{3}} - 1\right]^3 \qquad (6.1)$$

where B_0, B_0', E_0, and V_0 are the bulk modulus, pressure derivative of the bulk modulus, equilibrium energy, and equilibrium volume, respectively.

All of the systems were considered using primitive unit cells. For the (III-V)-IV_3 alloy systems these are 10-atom unit cells described by Grzybowski et al. and based on a 20-atom representation which was first described in Watkins et al.[25,27] Each 10-atom cell contains two tetrahedral (III-V)-IV_3 building blocks. This structure is based, originally, on a supercell of silicon containing 20 atoms, in which Si-Si pairs were replaced with Al-P dimer pairs. The replacement was done in a manner such that the Al-P pairs are completely isolated from one another. More generally this is a replacement of a IV-IV dimer with a III-V dimer in an extended group-IV matrix. This type of replacement can lead to several orientations of the (III-V)-IV_3 units, the one considered here contains the most highly ordered placement of III-V pairs. In [100] projection the group-V atoms form a sublattice such that the occupied columns are separated by a knights move from chess. The resulting unit cell is monoclinic, space group 9, with C1c1 symmetry, and the structure type is identical to that devised for Ge_3SnC by Zhang et al.[107]

6.3 Semiconductor Alloy Systems

6.3.1 Structural Description

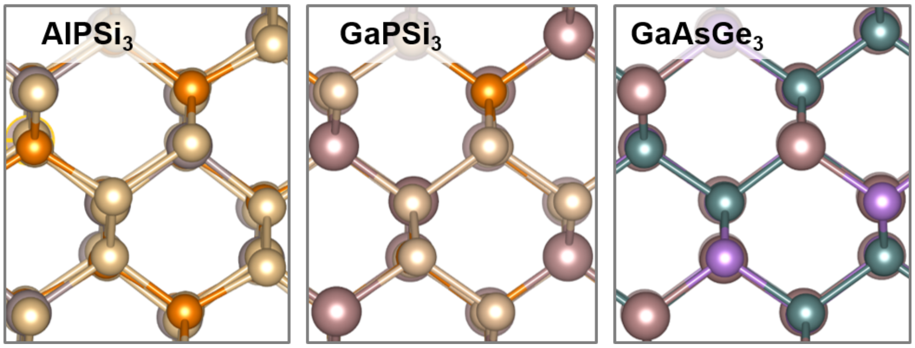

Figure 48: Ground state structures of $AlPSi_3$, $GaPSi_3$, and $GaAsGe_3$ viewed along [110] directions. This projection shows the typical dimer or "dumbbell" associated with diamond-like semiconductors, and illustrates the distortions due to the differing bond parameters of the III-V pair and the group-IV host matrix.

To augment previous chapters covering the experimental realization of $Al_{1-x}B_xPSi_3$, $GaPSi_3$, and $(GaAs)_{1-x}(Ge_2)_x$, optimized structures of the target system and parent alloys were calculated. Here $AlPSi_3$ is considered rather than the B-containing alloy to simplify the calculations interpretation. From these structures the level of reconciliation between the end-members to form a diamond-like solid can be seen in Figure 48. The ground state lattices are viewed along the [110] equivalent direction which clearly shows the minimal deviations from a diamond-like lattice. In this projection the perturbation to the ideal lattice is exemplified by a misalignment of the "dumbbell" feature. In these three systems, $AlPSi_3$, $GaPSi_3$, and $GaAsGe_3$, distortions provoked by the embedded III-V pair remain minor due to the similarity in size between the III-V pair and the IV-IV pair it replaces. This trend is exemplified in the Ga-As-Ge system where the lattice parameters of the end-members are most similar, consequently the perturbation is least striking. The degree of accommodation achieved in any particular system can be examined more closely by considering the individual building blocks, or tetrahedral $(III\text{-}V)\text{-}IV_3$ cores that interlink to form the solid.

From the relaxed ground-state structures, of the three semiconducting systems described above, tetrahedral cores have been extracted and are seen in Figure 49, where relevant atomic distances are shown. This figure emphasizes the deviations from an ideal tetrahedron, in which all the bond lengths should be equal and the edge lengths, basal and apical, should be equivalent. In the case of the $AlPSi_3$ system the Al-P bond is found to be 2.385 Å, 4.6% longer than the P-Si bond length. This difference leads to the inequality seen in the edge lengths, 3.775 Å and 3.754 Å, apical and basal respectively. Substitution of GaP for AlP to form $GaPSi_3$ provides a system in which the lattice parameters of the end-members, GaP and Si are closer than the previous system, $AlPSi_3$. This results in Ga-P and P-Si bond lengths of 2.372 Å and 2.278 Å, respectively, a difference of 4.1%. The discrepancy between the edge lengths is lessened to 1.3%, with an apical length of 3.782 Å and basal edge length of 3.734 Å.

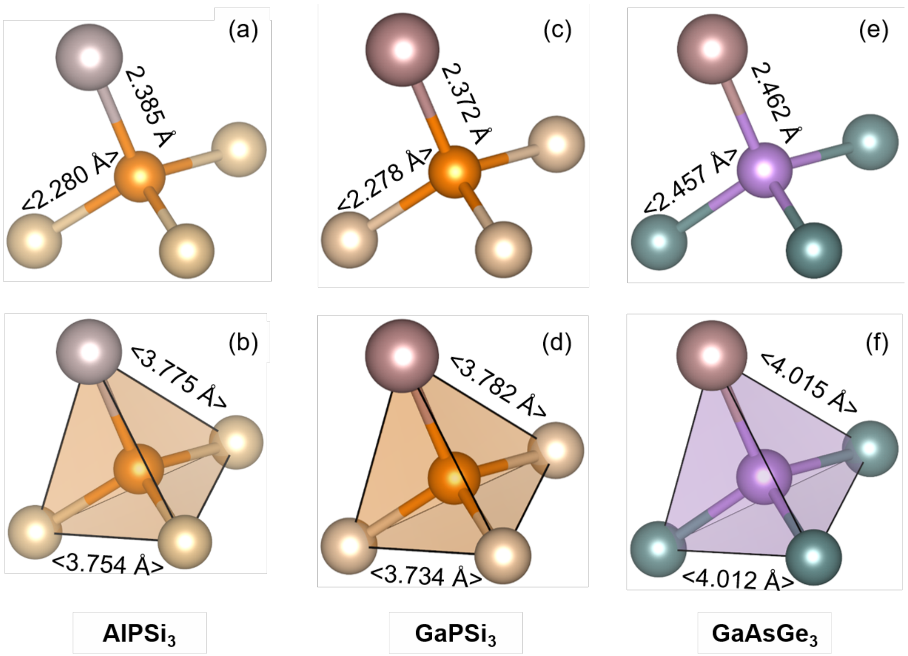

Figure 49: Tetrahedral (III-V)-IV_3 building-blocks extracted from the ground state structures of $AlPSi_3$, $GaPSi_3$, and $GaAsGe_3$. The top set of panels: (a), (c), and (e) contain the bond length information for each phase showing the III-V distance and average V-IV distance. The lower set: (b), (d), and (f) indicate how the basal and apical edges of each tetrahedral unit differ, illustrating the minor deviations from ideality.

Finally, considering the Ga-As-Ge alloy system, all the elements belong to the same period, akin to the Al-P-Si system, where the lattice parameters of the III-V and group-IV materials are expected to be similar. The difference in lattice parameter between GaAs and Ge, 0.1%, is so small it results in a nearly tetrahedral Ga-As-Ge_3 building-block. The Ga-As bond is 2.462 Å, only 2.0% longer than the As-Ge bond at 2.457 Å. The non-ideality of the Ga-As-Ge_3 tetrahedron is so minimal that the apical and basal edges are found to be $<$0.8% different at 4.015 Å and 4.012 Å.

Edge lengths are not the only variable on which the regularity of a tetrahedron can be assessed. The internal angles of a regular tetrahedron are 109.47°. In these systems there are two distinct types of bond angles, $\angle$III-V-IV and $\angle$IV-V-IV. For the $AlPSi_3$ system these angles are: ∠Si-P-Si = $\langle 110.85^\circ \rangle$ and ∠Al-P-Si = $\langle 108.01^\circ \rangle$. Both of these types of angles are within 1.4% of the optimal 109.47° tetrahedral angle, again corroborating the near ideality these building blocks possess. Though both of these sets of values may be used to evaluate the regularity of the tetrahedron, they are redundant. The geometric relationship between the dihedral angles of a general tetrahedron and edge length is well documented.[108]

The structural parameters of these alloys and their pseudo-binary end members are detailed in Table 6 at the end of this chapter. In this table the typical crystallographic parameters: a, b, c, α, β, and γ are shown for the conventional cell. In addition to these, the cubic lattice parameter, $\langle a_0 \rangle = (8\Omega)^{1/3}$, where Ω is volume per atom, is also shown allowing a more direct comparison to the cubic systems. Appendix A contains the crystallographic information for the aforementioned phases including atomic positions.

6.3.2 Thermodynamic Stability of $AlPSi_3$, $GaPSi_3$, and $GaAsGe_3$

Experimental realization of these hybrid alloys also depends on their thermodynamic stability. The regularization of tetrahedral building blocks to facilitate the crystal formation process is likely to be heuristic at this level. By considering the formation energies of these alloys from both standard states and from their pseudobinary end-members a more quantitative evaluation is attained. Using total energies obtained from the LDA calculations of the alloys, pseudobinary end-members, and constituent elements in standard states, two formation energies are calculated. The typical formation energy is calculated based on the formation of the (III-V)-IV_3 alloy from the constituent elements in standard state. For comparison the formation energies have also been calculated in relation to the pseudobinary end-members, III-V compound and group-IV components.

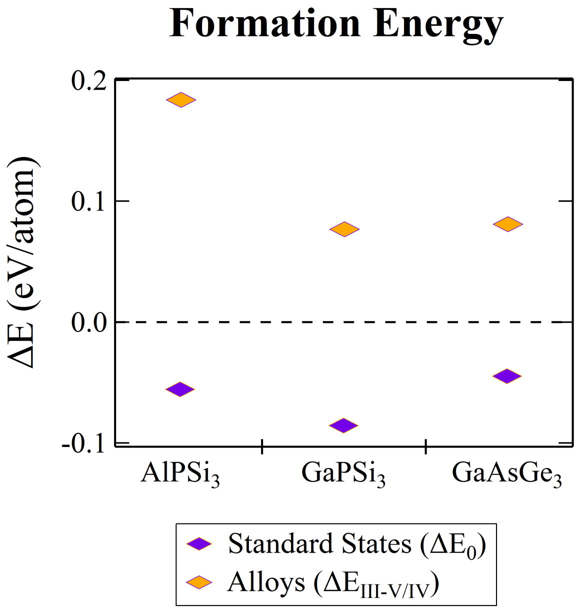

Figure 50: Formation energies in terms of ΔE_0/atom for formation from both the standard state (elements) shown with purple diamonds and from the pseudobinary end-members (alloys and group-IV) with orange diamonds. The systems with low purple diamonds at lower energies and small distance between the purple and orange diamonds are more favored.

The AlPSi$_3$, GaPSi$_3$, and GaAsGe$_3$ systems are expected to be stable with respect to the elements, but metastable with respect to the binary III-V and group-IV end members. To interpret a plot such as the one depicted in Figure 50, the absolute position of the purple diamond, representing the formation energy from the elements, ΔE_0, and the relative position of the orange diamond, $\Delta E_{\text{III-V/IV}}$, are needed. When considering the formation energy from the elements, ΔE_0, the more negative the number is, the more favorable the formation is. The interpretation associated with $\Delta E_{\text{III-V/IV}}$ is less intuitive, in this case the relative distance from the ΔE_0 is the relevant parameter. The most favorable system is one in which the $\Delta E_{\text{III-V/IV}}$ - ΔE_0 distance is minimized. Using these guidelines synthetic targets become more directed, and with that in mind theoretical efforts can be further focused to determine materials properties. From the above guidelines it is clear all three phases are stable with respect to the elements. The $GaPSi_3$ phase is the most stable, and the $GaAsGe_3$ phase is the least. The values obtained for $\Delta E_{\text{III-V/IV}}$ are all above zero, indicating the (III-V)-IV_3 alloys are metastable with respect to the pseudobinary end-members, $GaPSi_3$ being the least metastable. Additionally, this system has the smallest difference between ΔE_0 and $\Delta E_{\text{III-V/IV}}$, this is a good indication this is the most experimentally feasible system. Using this same logic, $AlPSi_3$ would be the "least" attainable synthetic target, even though all these alloys have been synthesized. The trends seen in these data agree with those previously published for $AlPSi_3$ and $GaAsGe_3$.[99]

6.4 Superhard Materials

Just as with semiconductors the demand for superhard materials is constantly rising in an effort to keep industrial activities in line with global needs. Superhards are indispensable in the areas of high-performance cutting, drilling, and grinding of ferrous and non-ferrous materials during manufacturing. For a material to be considered superhard it must possess a Vickers hardness over 40 GPa.[109] This means the material is resistant to deformation, a property that is desirable in manufacturing. This level of hardness among other physical properties make them invaluable in the industrial setting. These materials are used as abrasives for polishing, cutting, and drilling amidst more esoteric applications. Diamond and cubic boron nitride (c-BN) are the two most renowned superhards; diamond is the harder of the two materials with a Vickers hardness of 60-80 GPa, c-BN is second with a hardness of 30-45 GPa.[110] Though these materials have found use, they are far from perfect. Diamond cannot be used in processes involving iron and it has poor thermal stability.[111,112] c-BN, though only having half the hardness of diamond, has a higher thermal stability and can be used in ferrous applications due to it's low reactivity towards iron.

As with the semiconductors described previously, computational insights can be invaluable in the design of new materials. Predicting the hardness of a material alleviates some of the pressure on synthetic materials scientists by providing synthetic targets with some level of vetting. The typical figure of merit for a superhard material, Vickers hardness, is difficult to predict as it is governed by a large number of factors. However, materials which have a high Vickers hardness tend to have a high bulk modulus, a parameter which is more tractable for computational methods.[113] Through the use of the BM-EOS, bulk moduli of materials can be estimated and used as a litmus test for the design of superhard materials. The remainder of this chapter explores four (III-V)-IV$_3$ alloy systems as possible hard and superhard materials.

6.4.1 Structural Description

Ground state lattices of BNC$_3$, BNSi$_3$, BPC$_3$, and BPSi$_3$ were calculated using the computational methods described in previous sections. The extended structures are shown in Figure 51 along a direction equivalent to a diamond-like [110] direction. Deviations from the ideal tetrahedral structure expected from the covalent network bonding are clearly seen in this projection. Structural and crystallographic parameters of these phases and relevant end-members are shown in Table 7 and Appendix A. As the differences between lattice parameters of the end-members increases, larger

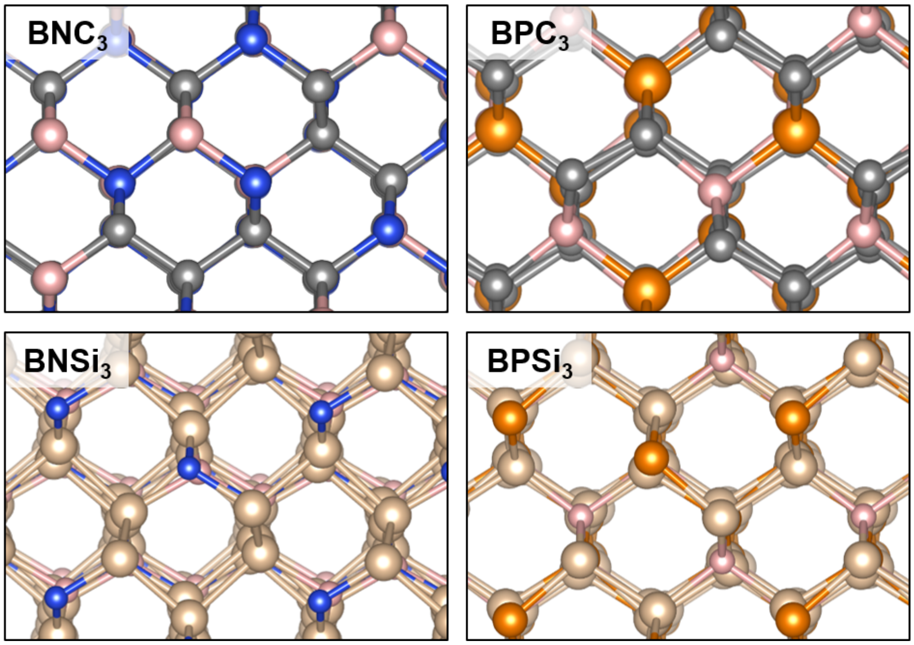

Figure 51: Ground state structures of BNC$_3$, BPC$_3$, BNSi$_3$, and BPSi$_3$ viewed along [110] directions.

distortions are seen; this trend parallels those observed for the AlPSi$_3$, GaPSi$_3$, and GaAsGe$_3$ semiconductor systems. In the case of these systems this is expected to have an effect on the materials properties, disruptions from ideal tetrahedral bonding likely leads to a decreased hardness. The tetrahedral building blocks have been extracted from the static ground state structures and subsequently analyzed for regularity.

Figure 52 shows the extracted pseudo-tetrahedral units for the four materials mentioned previously. The lattice parameter differences between the group-IV and III-V end-members for the alloy systems are 1.4%, 50.2%, 27.2%, and 19.7% for BNC$_3$, BNSi$_3$, BPC$_3$, and BPSi$_3$, respectively. These differences are clearly seen in the building blocks. Though the bond length between B-N (1.576 Å) differs from the N-C bond (1.517 Å) by nearly 4%, the level accommodation afforded via interlinking of the B-N-C$_3$ is impressive, and leads to a building block whose differences in edge length vary by approximately 0.3%. At the other extreme, the BNSi$_3$ case, the B-N bond

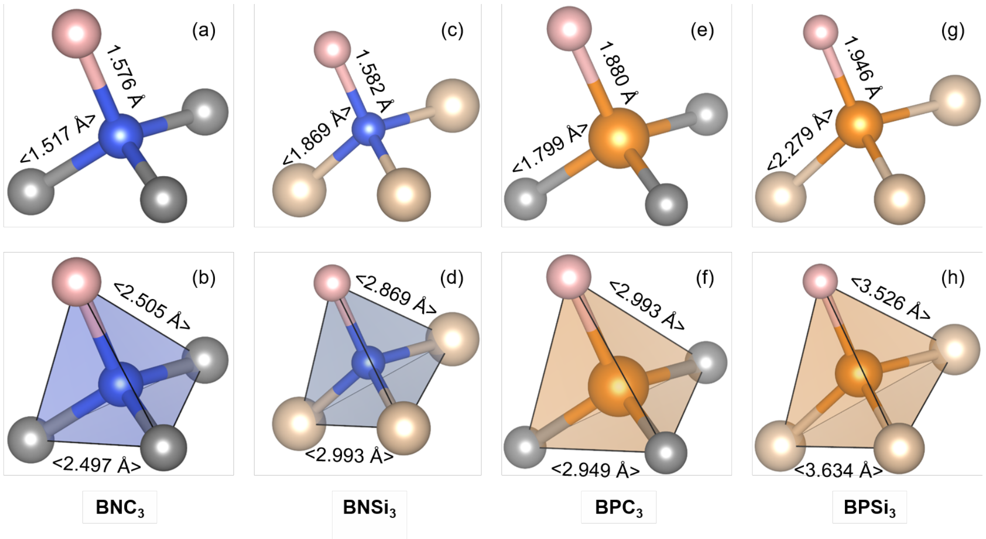

Figure 52: Tetrahedral building blocks of BNC_3, $BNSi_3$, BPC_3, and $BPSi_3$ extracted from the ground state structures showing relevant atomic distances. Images (a), (c), (e), and (g) illustrate the bond lengths between the III-V pair and the average bond length for the V-IV atoms. The lower images, (b), (d), (f), and (h) show the edge lengths of the tetrahedral building blocks.

length is found to be 1.582 Å, not surprisingly this distance is 18.1% smaller than the N-Si bond length. However, the degree of regularization achieved in the crystal assembly is very noteworthy: the edge length distortions are reduced to 4.3%. In parallel to the observations from the BN containing systems the BP systems achieve compromise that is comparable based on the lattice parameter differences. BPC_3 shows a bond length difference of 4.50%, B-P is 1.880 Å and P-Si is shorter at 1.799 Å. Upon substitution of silicon for carbon in creating the $BPSi_3$ system the difference in bond length increases significantly. The B-P bond length dilates to 1.946 Å because of the inherently longer P-Si bond, in this case, 2.279 Å. This dissimilarity leads to a variation in edge lengths of 3.1% where the apical edge is 3.526 Å and the basal edge measures 3.634 Å. These deviations may be a worst case scenario; it is likely the highly ordered arrangement of III-V pairs induces a structural bias. Larger cells which allow for a more varied arrangement of the isolated III-V pairs and symmetry reduction provide a route to eliminate bias and more closely approximate the real alloy.

6.4.2 Thermodynamic Stability of BNC_3, $BNSi_3$, BPC_3, and $BPSi_3$

In a similar fashion to what was done for the energetic study of the semiconducting systems, these systems have again been considered. Within these four systems, BNC_3, BPC_3, and $BPSi_3$ were considered in a prior DFT study in which the formation energies were calculated; the data presented in this chapter are consistent qualitatively and quantitatively.[99] The interpretation of the data is exactly as described above. One interesting thing to note within this set of alloys is the BPC_3 case, which is metastable with respect to both the elements and the pseudobinary end-members. From a synthetic perspective that is discouraging, but by no means does it preclude this material from being realized at some point; experimentalists are clever, and metastable does not mean impossible.

The remaining three systems are stable with respect to the elements. However, it is clear for the BNC_3 and $BNSi_3$ systems the large discrepancies between ΔE_0 and $\Delta E_{\text{III-V/IV}}$ make the systems much more unfavorable than $BPSi_3$. In comparison $BPSi_3$ has a very small ΔE_0-$\Delta E_{\text{III-V/IV}}$ gap. This places $BPSi_3$ as a very good candidate, the best of these four, as a target for synthetic and computational consideration. With diligent work $BPSi_3$ may be for hard materials in this class what $AlPSi_3$ was for the (III-V)-IV_3 semiconductors.

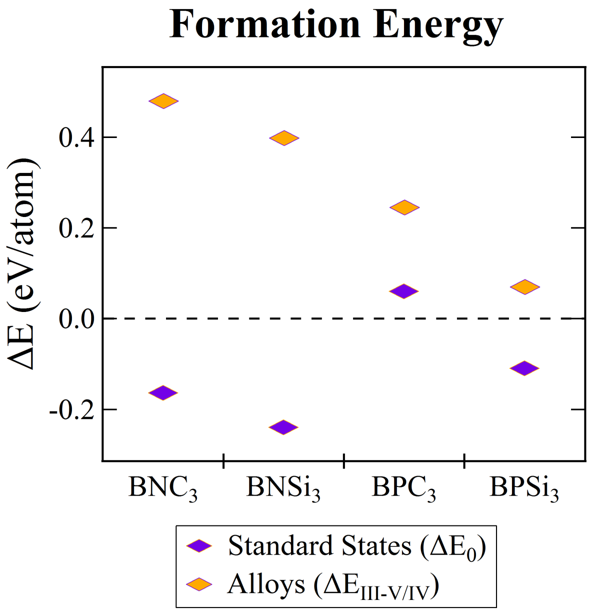

Figure 53: Formation energies in terms of ΔE_0/atom for formation from both the standard state (elements) shown with purple diamonds and from the pseudobinary end-members (alloys and group-IV) with orange diamonds. The systems with purple diamonds at lower energy and small distance between the purple and orange diamonds are more favored.

6.4.2.1 Special Considerations for N_2

The total free energy of elemental nitrogen was calculated by considering dinitrogen in a box with dimensions 15×15×15 Å^3. The structure was optimized using the same criteria as the extended systems, yielding a bond length of 1.119 Å. The computed value is less than 2% larger than the experimental bond length, 1.098 Å.[114] To further validate this approximation, the vibrational frequency was calculated and found to be 2400.7 cm^{-1}, in good agreement with the experimental value, 2358.6 cm^{-1}.[114]

6.4.3 Energy-Volume Equation of State: Bulk Moduli

The interesting properties of these alloys are not limited to the compositions and atomic arrangements within. As discussed earlier there are problems with using either pure diamond or c-BN as tooling materials; alloys between the two may be an effective solution to these industrial problems. The predictive power of computational chemistry is likely to aide in the design of new materials within this class. High quality calculations allow for the prediction of interesting properties, even physical ones. Using this computational methodology, trends and selected experimental observables are in good accordance with reported values. The fidelity of the data is high enough that the extraction of the bulk modulus has been attempted for the four (III-V)-IV_3 alloy systems and their end-members considered in this section.

The bulk modulus, B_0 can be determined using the energy volume equation of state and is related to the curvature of E(V). E-V curves were generated by varying the volume of the ground state, zero-pressure, unit cell isotropically, and conducting a self-consistent energy calculation. The E-V curves were then fit using the BM-EOS shown in Equation 6.1. The values of B_0, B_0', E_0, and V_0 are the bulk modulus, pressure derivative of the bulk modulus, equilibrium energy, and equilibrium volume, respectively; the results are summarized in Table 5. The final four rows of this table show both computed and experimental values of B_0 and V_0 for known systems, and in all cases they agree quite well. The excellent correspondence may portend the ability to observe a trend in materials properties of these alloys. Figure 54 shows the E-V data for BNC_3 along with the fit line for the BM-EOS. The fitted data correspond to a bulk modulus of 412 GPa and is intermediate to the alloy end-members of diamond and c-BN. This places this material well within the limits for what is considered a

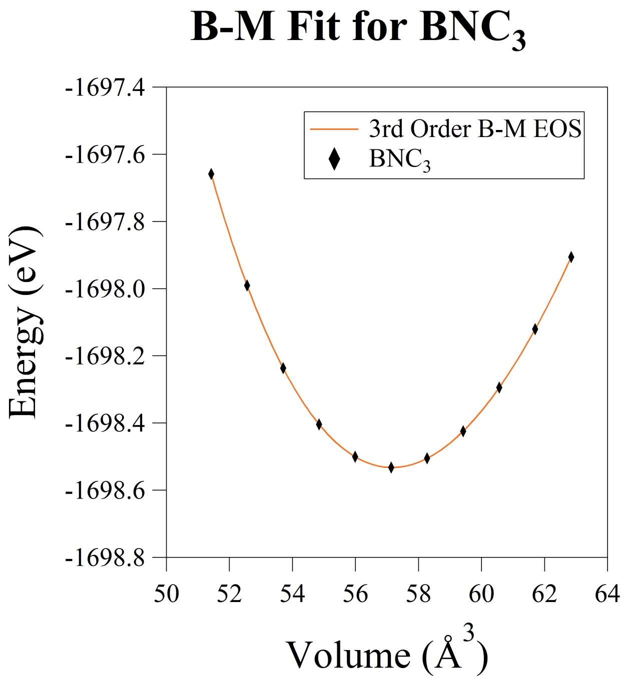

Figure 54: Energy-volume curve for BNC_3 and BM-EOS fitted line (orange) showing the close correspondence of the fit to the computational data (black diamonds).

very hard material, and may indicate that such a phase would possess a high Vickers hardness. Considering the remaining phases, BPC_3 has a high bulk modulus and may be an interesting candidate material. However, $BNSi_3$ and $BPSi_3$ are rather soft materials with values that are nearly three-times less, or more, than diamond.

As an added precaution, the differential with respect to volume of Equation 6.1 was used to determine the pressure associated with each volume. In this scheme a negative pressure corresponds to a cell with a volume higher than the ground state, while positive pressure corresponds to a cell being compressed into a smaller volume. In addition to the determination of the total energy at every self-consistent step the pressure was also output from the QE package. This value of pressure was then

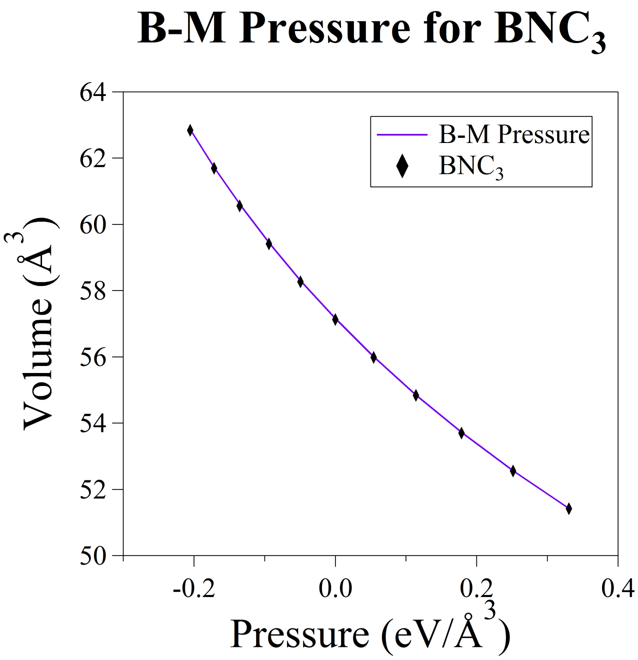

Figure 55: Data fitted to the Birch-Murnaghan equation of state using the parameters determined from the E-V relationships to ensure the data were consistent with computational results. There are no observed deviations from the predicted values.

compared to the volume derivative of E(V) giving P(V):

$$P(V) = \frac{3}{2}B_0\left[\left(\frac{V_0}{V}\right)^{\frac{7}{3}} - \left(\frac{V_0}{V}\right)^{\frac{5}{3}}\right]\left\{1 + \frac{3}{4} + (B_0' - 4)\left[\left(\frac{V_0}{V}\right)^{\frac{2}{3}} - 1\right]\right\} \tag{6.2}$$

Figure 55 shows the pressure-volume relationship for the BNC_3 system plotted against the Birch-Murnaghan pressure calculated using Equation 6.2. The data from this check are again in line with the calculations, further validating the predictive power of the data obtained for the various systems.

Table 5: Bulk moduli of selected (III-V)-IV_3 systems and their parent alloy systems for reference. These were all calculated using the 3rd order Birch-Murnaghan equation of state (see Equation 6.1), and χ^2 indicates the goodness of fit.

	B_0 (GPa)	$B_{0,\mathrm{exp}}$ (GPa)	B'	B'_{exp}	V_0 ($\mathrm{\AA}^3$)	$V_{0,\mathrm{exp}}$ ($\mathrm{\AA}^3$)	χ^2
BNC_3	412	–	3.70	–	57.16	–	2.2×10^{-7}
$BNSi_3$	160	–	4.02	–	123.80	–	8.3×10^{-8}
BPC_3	311	–	3.79	–	74.53	–	4.6×10^{-8}
$BPSi_3$	121	–	4.08	–	158.03	–	8.6×10^{-8}
c-BN	401	401[a]	3.63	3.06[a]	11.50	11.81[g]	1.0×10^{-9}
BP	175	174[b]	3.75	3.22[b]	22.67	23.36[g]	2.9×10^{-9}
Si	96	99[c]	4.24	4.24[e]	39.36	40.04[g]	1.6×10^{-8}
d-C	465	446[d]	3.64	3.00[f]	11.03	11.34[g]	7.9×10^{-9}

Refs: [a] Nagakubo et al.[115], [b] Solozhenko et al.[116], [c] Yin and Cohen[117], [d] Gillet et al.[118], [e] Lam et al.[119], [f] Occelli et al.[120], [g] Wyckoff[121]

6.5 Conclusion

DFT has been used as an effective tool to enhance the understanding of the materials within the class of lattice matched (III-V)-IV_3 semiconductors and boron containing alloys. Using structural optimizations, insights into how the perturbations to the group-IV host matrix reacts to the insertion of the III-V pair have been shown through geometric means. The surprising realization is that even with large variations in bond parameters in the end-members, the host matrix accommodates the guest dimer pairs very well and undergoes a significant amount of regularization. This bodes well for the fabrication of (III-V)-IV_3 materials comprised of end-members with very different lattice parameters, and the major hurdle from this perspective then becomes one of finding a suitable platform for epitaxy. The energetics of formation have been used to determine the relative stability of the phases, as well commentary on the synthetic likelihood based on the differences between the ΔE_0 and $\Delta E_{\text{III-V/IV}}$ values. In regards to the superhard materials, though three of the materials were found to be on the softer end of the scale, one new material, BNC_3, was found to be a superhard material candidate with a bulk modulus of 412 GPa. The seven systems discussed here are a small subset of all possible (III-V)-IV_3 materials. Collectively this analysis indicates the synthetic strategy used to realize the systems discussed in this dissertation can be used to extend even further from those explored and experimentally realized.

Table 6: Structural parameters for $AlPSi_3$, $GaPSi_3$, $GaAsGe_3$, aluminum phosphide, gallium phosphide, aallium arsenide, silicon, and germanium

	Z	a (Å)	b (Å)	c (Å)	α (°)	β (°)	γ (°)	$\langle a_0 \rangle_{\text{calc.}}$ (Å)	Space Group
$AlPSi_3$	4	8.5759	8.5453	5.4601	90	90	90.33	5.4294	C1c1 (9)
$GaPSi_3$	4	8.5220	8.4879	5.4090	90	90	90.00	5.3890	C1c1 (9)
$GaAsGe_3$	4	8.9045	8.9045	5.6511	90	90	90.04	5.6382	C1c1 (9)
AlP	4	5.4291	5.4291	5.4291	90	90	90	5.4291	F$\bar{4}$3m (216)
GaP	4	5.3873	5.3873	5.3873	90	90	90	5.3873	F$\bar{4}$3m (216)
GaAs	4	5.6021	5.6021	5.6021	90	90	90	5.6021	F$\bar{4}$3m (216)
Si	8	5.3995	5.3995	5.3995	90	90	90	5.3995	Fd$\bar{3}$m (216)
Ge	8	5.6074	5.6074	5.6074	90	90	90	5.6074	Fd$\bar{3}$m (216)

Note: $\langle a_0 \rangle_{\text{calc}} = (8\Omega)^{1/3}$. Where Ω is the atomic volume for the given system, calculated by taking the volume of the conventional unit cell and dividing by the number of atoms.

Table 7: Structural parameters for BNC_3, $BNSi_3$, BPC_3, $BPSi_3$, cubic BN, BP, silicon, and diamond

	Z	a (Å)	b (Å)	c (Å)	α (°)	β (°)	γ (°)	$\langle a_0 \rangle_{\text{calc.}}$ (Å)	Space Group
BNC_3	4	5.6476	5.6476	3.5823	90	90	90.24	3.5753	C1c1 (9)
$BNSi_3$	4	7.3731	7.1663	4.6875	90	90	91.81	4.6264	C1c1 (9)
BPC_3	4	6.1881	6.1578	3.9103	90	90	90.52	3.9061	C1c1 (9)
$BPSi_3$	4	7.9400	7.9220	5.0243	90	90	90.27	5.0187	C1c1 (9)
c-BN	4	3.5826	3.5826	3.5826	90	90	90	3.5826	F$\bar{4}$3m (216)
BP	4	4.4927	4.4927	4.4927	90	90	90	4.4927	F$\bar{4}$3m (216)
Si	8	5.3995	5.3995	5.3995	90	90	90	5.3995	Fd$\bar{3}$m (216)
d-C	8	3.5332	3.5332	3.5332	90	90	90	3.5332	Fd$\bar{3}$m (216)

Note: $\langle a_0 \rangle_{\text{calc}} = (8\Omega)^{1/3}$. Where Ω is the atomic volume for the given system, calculated by taking the volume of the conventional unit cell and dividing by the number of atoms.

REFERENCES

(1) Bloch, F. *Z. Phys.* **1928**, *52*, 555.

(2) Busch, G. *Eur. J. Phys* **1989**, *10*, 254.

(3) Haller, E. E. *Mater. Sci. Semicond. Process.* **2006**, *9*, 408.

(4) Bardeen, J.; Brattain, W. H. *Phys. Rev.* **1948**, *74*, 230.

(5) Siffert, P., Krimmel, E. F., Eds. *Silicon Evolution and Future of a Technology*; Springer-Verlag, 2004.

(6) Kilby, J. *ChemPhysChem* **2001**, *2*, 482.

(7) Noyce, R. N. Semiconductor Device-and-Lead Structure. U.S. Patent 2,981,877, Sep 11, 1959.

(8) Holonyak Jr., N.; Bevacqua, S. F. *Appl. Phys. Lett.* **1962**, *1*, 82.

(9) Becke, H.; Hall, R.; White, J. *Solid-State Electron.* **1965**, *8*, 813.

(10) Pengelly, R. S.; Turner, J. A. *Electron. Lett.* **1976**, *12*, 251.

(11) Nagarajan, R. et al. *IEEE J. Sel. Top. Quantum Electron.* **2005**, *11*, 50.

(12) Newman, K. E.; Dow, J. D. *Phys. Rev. B* **1983**, *27*, 7495.

(13) Newman, K. E.; Lastras-Martinez, A.; Kramer, B.; Barnett, S. A.; Ray, M. A.; Dow, J. D.; Greene, J. E.; Raccah, P. M. *Phys. Rev. Lett.* **1982**, *50*, 1466.

(14) Davis, L. C.; Holloway, H. *Phys. Rev. B* **1987**, *35*, 2767.

(15) Holloway, H.; Davis, L. C. *Phys. Rev. Lett.* **1984**, *53*, 830.

(16) Osório, R.; Froyenand, S.; Zunger, A. *Phys. Rev. B* **1991**, *43*, 14055.

(17) Giorgi, G.; Van Schilfgaarde, M.; Korkin, A.; Yamashita, K. *Nanoscale Res. Lett.* **2010**, *5*, 469.

(18) Noreika, A. J.; Francombe, M. H. *J. Appl. Phys.* **1974**, *45*, 3690.

(19) Cadien, K. C.; Eltoukhy, A. H.; Greene, J. E. *Appl. Phys. Lett.* **1982**, *38*, 253.

(20) Cadien, K. C.; Eltoukhy, A. H.; Greene, J. E. *Vacuum* **1982**, *31*, 773.

(21) Cadien, K. C.; Greene, J. E. *Appl. Phys. Lett.* **1982**, *40*, 329.

(22) Barnett, S. A.; Ray, M. A.; Lastras, A.; Kramer, B.; Greene, J. E.; Raccah, P. M.; Abels, L. L. *Electron. Lett.* **1982**, *18*, 891.

(23) Norman, A. G.; Olson, J. M.; Geisz, J. F.; Moutinho, H. R.; Mason, A.; Al-Jassim, M. M.; Vernon, S. M. *Appl. Phys. Lett.* **1999**, *74*, 1382.

(24) Solozhenko, V. L.; Andrault, D.; Guillame, F.; Mezouar, M.; Rubie, D. C. *Appl. Phys. Lett.* **2001**, *78*, 1385.

(25) Watkins, T.; Chizmeshya, A. V. G.; Jiang, L.; Smith, D. J.; Beeler, R. T.; Grzybowski, G.; Poweleit, C. D.; Menéndez, J.; Kouvetakis, J. *J. Am. Chem. Soc.* **2011**, *133*, 16212.

(26) Watkins, T.; Jiang, L.; Xu, C.; Chizmeshya, A. V. G.; Smith, D. J.; Menéndez, J.; Kouvetakis, J. *Appl. Phys. Lett.* **2012**, *100*, 022101.

(27) Grzybowski, G.; Watkins, T.; Beeler, R. T.; Jiang, L.; Smith, D. J.; Chizmeshya, A. V. G.; Kouvetakis, J.; Menéndez, J. *Chem. Matter.* **2012**, *24*, 2347.

(28) Kouvetakis, J.; Chizmeshya, A. V. G.; Jiang, L.; Watkins, T.; Grzybowski, G.; Beeler, R. T.; Poweleit, C.; Menéndez, J. *Chem. Matter.* **2012**, *24*, 3219.

(29) Jiang, L.; Sims, P. E.; Grzybowski, G.; Beeler, R. T.; Chizmeshya, A. V. G.; Smith, D. J.; Kouvetakis, J.; Menéndez, J. *Phys. Rev. B* **2013**, *88*, 045208.

(30) Sims, P. E.; Chizmeshya, A. V. G.; Jiang, L.; Beeler, R. T.; Poweleit, C. D.; Gallagher, J.; Smith, D. J.; Menéndez, J.; Kouvetakis, J. *J. Am. Chem. Soc.* **2013**, *135*, 12388.

(31) Banerjee, I.; Chung, D. W.; Kroemer, H. *Appl. Phys. Lett.* **1985**, *46*, 494.

(32) Kehoe, A. B.; Temple, D. J.; Watson, G. W.; Scanlon, D. O. *Phys. Chem. Chem. Phys.* **2013**, *15*, 15477.

(33) Carenco, S.; Portehault, D.; Boissière, C.; Mézailles, N.; Sanchez, C. *Chem. Rev.* **2013**, *113*, 7981.

(34) Kouvetakis, J.; Mathews, J.; Roucka, R.; Chizmeshya, A. V. G.; Tolle, J.; Menéndez, J. *IEEE Photonics J.* **2010**, *2*, 924.

(35) Sohn, H.; Webber, E. R.; Nozaki, S.; Takahashi, K. *Appl. Phys. Lett.* **1995**, *67*, 1104.

(36) Lautenschlager, P.; Garriga, M.; Cardona, M. *Phys. Rev. B* **1987**, *36*, 4813.

(37) Kim, J.; Fischetti, M. V. J. *J. Appl. Phys.* **2010**, *108*, 013710.

(38) D'Costa, V. R.; Cook, C. S.; Birdwell, A. G.; Littler, C. L.; Canonico, M.; Zollner, S.; Kouvetakis, J.; Menéndez, J. *Phys. Rev. B* **2006**, *73*, 125207.

(39) D'Costa, V. R.; Tolle, J.; Poweleit, C. D.; Kouvetakis, J.; Menéndez, J. *Phys. Rev. B* **2007**, *76*, 035211.

(40) Yang, J.-H.; Zhai, Y.; Liu, H.; Xiang, H.; Gong, X.; Wei, S.-H. *J. Am. Chem. Soc.* **2012**, *134*, 12653.

(41) Kolyubakin, A. I.; Osp'yan, Y. A.; Shevchenko, S. A.; Shteinman, E. A. *Sov. Phys. - Solid State* **1984**, *26*, 407.

(42) Vurgaftman, I.; Meyer, J. R.; Ram-Mohan, L. R. *J. Appl. Phys.* **2001**, *89*, 5815.

(43) Fujii, M.; Hayashi, S.; Yamamoto, K. *Appl. Phys. Lett.* **1990**, *57*, 2697.

(44) Mooradian, A.; Wright, G. B. *Solid State Commun.* **1966**, *4*, 431.

(45) Fritsch, J.; Pavone, P.; Schröder, U. *Phys. Rev. B* **1995**, *52*, 11326.

(46) Weinstein, B. A.; Cardona, M. *Phys. Rev. B* **1973**, *7*, 2545.

(47) Renucci, M. A.; Renucci, J. B.; Zeyher, R.; Cardona, M. *Phys. Rev. B* **1974**, *10*, 4309.

(48) Cai, Y.; Thorpe, M. F. *Phys. Rev. B* **1992**, *46*, 15872.

(49) Singh, R.; Poweleit, C. D.; Dailey, E.; Drucker, J.; J., M. *Semicond. Sci. Technol.* **2012**, *27*, 085008.

(50) Frisch, M. J. et al. Gaussian 03, Revision C.02. Gaussian, Inc., Wallingford, CT, 2004.

(51) Kresse, G.; Hafner, J. *Phys. Rev. B* **1993**, *47*, 558.

(52) Kresse, G.; Furthmüller, J. *Comput. Mater. Sci.* **1999**, *6*, 15.

(53) Kresse, G.; Furthmüller, J. *Phys. Rev. B* **1996**, *54*, 11169.

(54) Rankin, D. W. H.; Robiette, A. G.; Sheldrick, G. M.; Beagley, B.; Hewitt, T. G. *J. Inorg. Nucl. Chem.* **1969**, *31*, 2351.

(55) Sims, P.; Aoki, T.; Favaro, R.; Wallace, P.; White, A.; Xu, C.; Menéndez, J.; Kouvetakis, J. *Chem. Matter.* **2015**, *27*, 3030.

(56) Sims, P.; Aoki, T.; Menéndez, J.; Kouvetakis, J. *Microsc. Microanal.* **2015**, *S3*, 1923.

(57) Momma, K.; Izumi, F. *J. Appl. Crystallogr.* **2011**, *44*, 1272.

(58) Jiang, L.; Aoki, T.; Smith, D. J.; Chizmeshya, A. V. G.; Menéndez, J.; Kouvetakis, J. *Chem. Matter.* **2014**, *26*, 4092.

(59) Turley, J. W.; Rinn, H. W. *Inorg. Chem.* **1969**, *8*, 18.

(60) Wang, X.; Andrews, L.; Tam, S.; DeRose, M. E.; Fajardo, M. E. *J. Am. Chem. Soc.* **2003**, *125*, 9218.

(61) Schlesinger, H. I.; Brown, H. C.; K., H. E. *J. Am. Chem. Soc.* **1953**, *75*, 209.

(62) Geisz, J. F.; Friedman, D. J. *Semicond. Sci. Technol.* **2002**, *17*, 769.

(63) Lindsay, L.; Broido, D. A.; Reinecke, T. L. *Phys. Rev. Lett.* **2013**, *111*, 025901.

(64) Greenwood, N. N.; Earnshaw, A. *Chemistry of the Elements*, 2nd ed.; Elsevier Butterworth-Heinemann, 1997.

(65) Tice, J. B.; Chizmeshya, A. V. G.; Tolle, J.; D'Costa, V. R. D.; Menéndez, J.; Kouvetakis, J. *Dalton Trans.* **2010**, *39*, 4551.

(66) Roucka, R. Epitaxial Growth of Novel Wide Bandgap Semiconductors and Metallic Diborides on Silicon. Ph.D. thesis, Arizona State University, 2004.

(67) Temple, P.; Hathaway, C. *Phys. Rev. B* **1973**, *7*, 3685.

(68) Windl, W.; Pavone, P.; Karch, K.; Schütt, O.; Strauch, D.; Gianozzi, P.; Baroni, S. *Phys. Rev. B* **1993**, *48*, 3164.

(69) Tsvetov, V.; Allred, W.; Spitzer, W. G. *Appl. Phys. Lett.* **1967**, *10*, 326.

(70) Jouanne, M.; Morhange, J. F.; Balkanski, M. *Phys. Status Solidi B* **1979**, *92*, 255.

(71) Fujii, M.; Sugimoto, H.; Hasegawa, M.; Imakita, K. *J. Appl. Phys.* **2014**, *115*, 084301.

(72) Sanjurjo, J. A.; López-Cruz, E.; Vogl, P.; Cardona, M. *Phys. Rev. B* **1983**, *28*, 4579.

(73) Meléndez-Lira, M.; Menéndez, J.; Kramer, K. M.; Thompson, M. O.; Cave, N.; Liu, R.; W., C. J.; Theodore, N. D.; Candelaria, J. J. *J. Appl. Phys.* **1997**, *82*, 4246.

(74) Engstrom, H.; Bates, J. B. *J. Appl. Phys.* **1979**, *50*, 2921.

(75) Aspnes, D. E.; Studna, A. A.; Kinsbron, E. *Phys. Rev. B* **1984**, *29*, 768.

(76) Sims, P. E.; Xu, C.; Poweleit, C. D.; Menéndez, J.; Kouvetakis, J. *Chem. Mater.* **Just Accepted Manuscript** DOI:10.1021/acs.chemmater.7b00347.

(77) Lazzouni, M. E.; Sham, L. J. *Appl. Phys. Lett.* **1993**, *63*, 3253.

(78) Tang, C. Y.; Downs, A. J.; Greene, T. M.; Kettle, L.; Rankin, D. W. H.; Robertson, H. E.; Turner, A. R. *Dalton Trans.* **2006**, 1204.

(79) Baxter, P. L.; Downs, A. J. *J. Chem. Soc. Dalton. Trans.* **1985**, 807–814.

(80) Frisch, M. J. et al. Gaussian 09 Revision E.01. Gaussian Inc. Wallingford CT 2009.

(81) Perdew, J. P.; Burke, K.; Ernzerhof, M. *Phys. Rev. Lett.* **1996**, *77*, 3865.

(82) Yamauchi, Y.; Kobayashi, N. *Jpn. J. Appl. Phys., Part 2* **1993**, *32*, L160.

(83) Dorn, R.; Mueller, M.; Loberth, J.; Zimmermann, G.; Protzmann, H.; Stolz, W.; Goebel, E. O. *Mater. Sci. Eng., B* **1993**, *17*, 25.

(84) Ihikura, K.; Hayashi, K.; Ogawa, T.; Hasegawa, F. *Jpn. J. Appl. Phys., Part 2* **1993**, *32*, L1014.

(85) Malocsay, E.; Sundaram, V.; Fraas, L.; Melas, A. *J. Cryst. Growth* **1992**, *124*, 76.

(86) Beagley, B.; Robiette, A. G.; Sheldrick, G. M. *J. Chem. Soc. A* **1968**, 3002.

(87) Giannozzi, P. et al. *Journal of Physics: Condensed Matter* **2009**, *21*, 395502.

(88) Eckl, C.; Pavone, P.; Fritsch, J.; Schröder, U. In *The Physics of Semiconductors*; Scheffler, M., Zimmermann, R., Eds.; World Scientific, 1996; Vol. 3.

(89) Greene, J. E. *J. Vac. Sci. Technol., B: Microelectron. Nanometer Struct.–Process., Meas., Phenom.* **1983**, *1*, 229.

(90) Kawai, H.; Giorgi, G.; Yamashita, K. *Phys. Status Solidi B* **2012**, *249*, 29.

(91) Romano, L. T.; Robertson, I. M.; E., G. J.; E., S. J. *Phys. Rev. B* **1987**, *36*, 7523.

(92) Vernon, S. M.; Sanfacon, M. M.; Ahrenkiel, R. K. *J. Electron. Mater.* **1994**, *23*, 147.

(93) Rodríguez, H.; Navarro-Contreras, H.; Vidal, M. A. *Appl. Phys. Lett.* **2000**, *77*, 2497.

(94) Sandhu, A.; Fujii, T.; Ando, H.; Takahashi, T.; Ishikawa, H.; Yokoyama, N. *J. Cryst. Growth* **1991**, *111*, 559.

(95) Ota, T.; Otake, S.; Iwasa, I. *J. Cryst. Growth* **1993**, *133*, 207.

(96) Xuliang, Z.; P., J.; Renrong, L.; Jing, W.; Wei, W. *J. Semicond.* **2014**, *35*, 073002.

(97) Xu, C.; Gallagher, J. D.; Wallace, P. M.; Senaratne, C. L.; Sims, P.; Menéndez, J.; Kouvetakis, J. *Semicond. Sci. Technol.* **2015**, *30*, 105028.

(98) Perdew, J. P.; Ruzsinszky, A.; Csonka, G. I.; Vydrov, O. A.; Scuseria, G. E.; Constantin, L. A.; Zhou, X.; Burke, K. *Phys. Rev. Lett.* **2008**, *100*, 136406.

(99) Chizmeshya, A. V. G.; Kouvetakis, J.; Grzybowski, G.; Beeler, R.; Menéndez, J. *ECS Trans.* **2012**, *50*, 623.

(100) Trzeciakowski, W.; Martínez-Pastor, J.; Cantarero, A. *J. Appl. Phys* **1997**, *82*, 3976.

(101) Menéndez, J. In *Raman Scattering in Materials Science*; Weber, W. H., Merlin, R., Eds.; Springer, 2000.

(102) Giannozzi, P.; de Gironcoli, S.; Pavone, P.; Baroni, S. *Phys. Rev. B* **1991**, *43*, 7231.

(103) Salazar-Hernández, B.; Vidal, M. A.; Constantino, M. E.; Navarro-Contreras, H. *Solid State Commun.* **1999**, *109*, 295.

(104) Johs, B.; Herzinger, C. M.; Dinan, J. H.; Cornfeld, A.; Benson, J. D. *Thin Solid Films* **1998**, *313-314*, 137.

(105) Hu, Y. Z.; Zettler, J.-T.; Chongsawangviron, S.; Wang, Y. Q.; Irene, E. A. *Appl. Phys. Lett.* **1992**, *61*, 1098.

(106) Perdew, J. P.; Zunger, A. *Phys. Rev. B* **1981**, *23*, 5048.

(107) Zhang, P.; Crespi, V. H.; Chang, E.; Louie, S. G.; Cohen, M. L. *Phys. Rev. B* **2001**, *64*, 235201.

(108) Wirth, K.; Dreiding, A. S. *J. Math. Chem.* **2014**, *52*, 1624.

(109) Sung, C.-M.; Sung, M. *Mater. Chem. Phys.* **1996**, *43*, 1.

(110) Zhao, Z.; Xu, B.; Tian, Y. *Annu. Rev. Mater. Res.* **2016**, *46*, 383.

(111) Paul, E.; Evans, C. J.; Mangamelli, A.; McGlauflin, M. L.; Polvani, R. S. *Precis. Eng.* **1996**, *18*, 4.

(112) Tanaka, H.; Shimada, S.; Ikawa, N.; Yoshinaga, M. *Key Eng. Mater.* **2001**, *196*, 69.

(113) Chung, H.-Y.; Weinberger, M. B.; Yang, J.-M.; Tolbert, S. H.; Kaner, R. B. *Appl. Phys. Lett.* **2008**, *92*, 261904.

(114) Huber, K. P.; Herzberg, G. *Molecular Spectra and Molecular Structure: IV Constants of Diatomic Molecules*; Van Nostrand Reinhold Ltd., 1979; Vol. 4.

(115) Nagakubo, A.; Ogi, H.; Sumiya, H.; Kusakabe, K.; Hirao, M.

(116) Solozhenko, V. L.; Kurakevych, O. O.; Godec, Y. L.; Kurnosov, A. V.; Organov, A. R. *J. Appl. Phys.* **2014**, *116*, 033501.

(117) Yin, M. T.; Cohen, M. L. *Phys. Rev. B* **1982**, *26*, 5668.

(118) Gillet, P.; Fiquet, G.; Daniel, I.; Reynard, B.; Hanfland, M. *Phys. Rev. B* **1999**, *60*, 14660.

(119) Lam, P. K.; Cohen, M. L.; Martinez, G. *Phys. Rev. B* **1987**, *35*, 9190.

(120) Occelli, F.; Loubeyre, P.; R., L. *Nat. Mater.* **2003**, *2*, 151.

(121) Wyckoff, R. W. G. *Cyrstal Structures – Volume 1*, 2nd ed.; Interscience Publishers, 1963.

APPENDIX A

STRUCTURAL PROPERTIES OF (III-V)-IV$_3$ ALLOYS FROM QUANTUM CHEMICAL SIMULATIONS: SUPPLEMENTAL INFORMATION

Table A1: Crystallographic data for $AlPSi_3$

$AlPSi_3$			
Lattice Parameters			
a (Å)	8.5759	α (°)	90.00
b (Å)	8.5453	β (°)	90.00
c (Å)	5.4601	γ (°)	90.33
Atomic Positions			
Al	(4a)	-0.57751, 0.02545, 0.38504	
P	(4a)	0.27886, 0.42375, 0.14197	
Si1	(4a)	-0.87550,-0.36704, 0.14802	
Si2	(4a)	-0.68279,-0.77312, 0.12134	
Si3	(4a)	-0.47337,-0.17090, 0.10158	

Table A2: Crystallographic data for $GaPSi_3$

$GaPSi_3$			
Lattice Parameters			
a (Å)	8.5220	α (°)	90.00
b (Å)	8.4879	β (°)	90.00
c (Å)	5.4090	γ (°)	90.00
Atomic Positions			
Ga	(4a)	0.07528, 0.27704, 0.11843	
P	(4a)	-0.22184, 0.67486, 0.36454	
Si1	(4a)	-0.62314,-0.11971, 0.35685	
Si2	(4a)	-0.81800,-0.52373, 0.37482	
Si3	(4a)	-0.02426, 0.07957, 0.39347	

Table A3: Crystallographic data for $GaAsGe_3$

$GaAsGe_3$	
Lattice Parameters	
a (Å) 8.9045	α (°) 90.00
b (Å) 8.9045	β (°) 90.00
c (Å) 5.6511	γ (°) 90.04
Atomic Positions	
Ga (4a)	-0.82411, 0.02817, 0.37854
As (4a)	-0.52581,-0.57341, 0.13006
Ge1 (4a)	-0.13054, 0.63157, 0.13097
Ge2 (4a)	0.07266, 0.22114, 0.12434
Ge3 (4a)	-0.73036,-0.16929, 0.11947

Table A4: Crystallographic data for BNC_3

BNC_3	
Lattice Parameters	
a (Å) 5.6476	α (°) 90.00
b (Å) 5.6476	β (°) 90.00
c (Å) 3.5823	γ (°) 90.24
Atomic Positions	
B (4a)	0.02763, 0.42197, 0.37052
N (4a)	-0.07568, 0.22010, 0.11318
C1 (4a)	-0.86786,-0.37535, 0.11018
C2 (4a)	-0.27030,-0.18052, 0.13071
C3 (4a)	-0.67569, 0.02592, 0.13940

Table A5: Crystallographic data for $BNSi_3$

$BNSi_3$			
Lattice Parameters			
a (Å)	7.3731	α (°)	90.00
b (Å)	7.1663	β (°)	90.00
c (Å)	4.6875	γ (°)	91.81
Atomic Positions			
B	(4a)	-0.51425,-0.34713, 0.18222	
N	(4a)	-0.43398,-0.51859, 0.34707	
Si1	(4a)	-0.60097,-0.12741, 0.39519	
Si2	(4a)	-0.23223, 0.07581, 0.45073	
Si3	(4a)	-0.85667,-0.72085, 0.36384	

Table A6: Crystallographic data for BPC_3

BPC_3			
Lattice Parameters			
a (Å)	6.1881	α (°)	90.00
b (Å)	6.1578	β (°)	90.00
c (Å)	3.9103	γ (°)	90.52
Atomic Positions			
B	(4a)	-0.71272, 0.06436, 0.09438	
P	(4a)	-0.82606,-0.72022, 0.38222	
C1	(4a)	-0.60822,-0.11698, 0.36006	
C2	(4a)	-0.03030, 0.67390, 0.33275	
C3	(4a)	-0.43454,-0.51295, 0.39174	

Table A7: Crystallographic data for $BPSi_3$

$BPSi_3$			
Lattice Parameters			
a (Å)	7.9400	α (°)	90.00
b (Å)	7.9220	β (°)	90.00
c (Å)	5.0243	γ (°)	90.27
Atomic Positions			
B	(4a)	-0.72518, 0.07974, 0.13849	
P	(4a)	-0.81357,-0.73472, 0.34945	
Si1	(4a)	-0.63127,-0.11094, 0.35395	
Si2	(4a)	-0.03599, 0.66697, 0.41038	
Si3	(4a)	-0.40592, 0.48702, 0.39539	

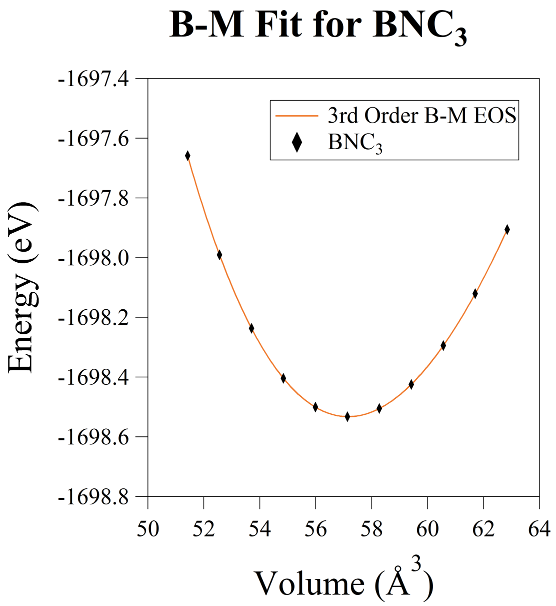

Figure A1: BNC$_3$ BM-EOS

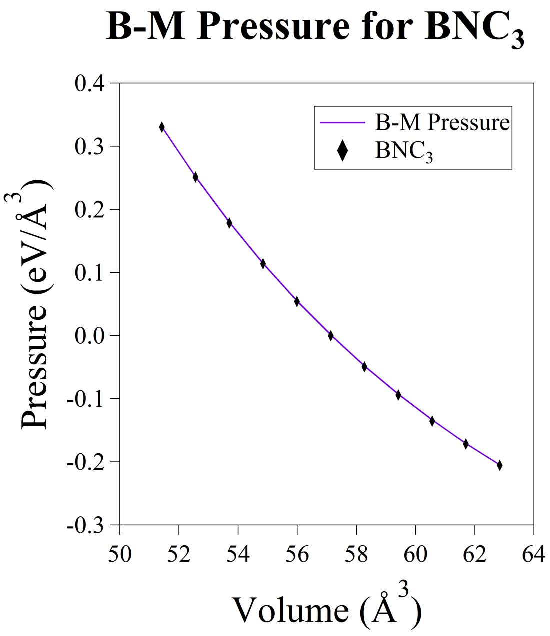

Figure A2: BNC$_3$ BM-Pressure

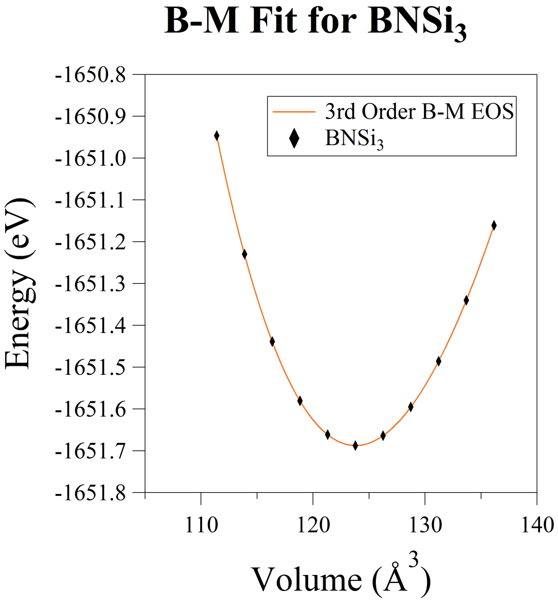

Figure A3: BNSi$_3$ BM-EOS

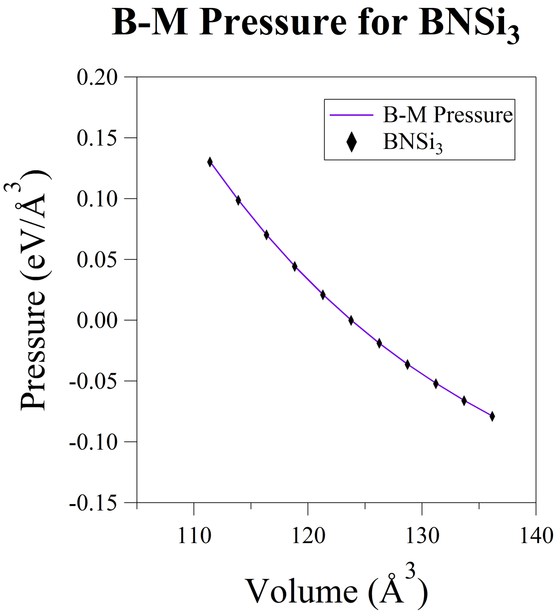

Figure A4: BNSi$_3$ BM-Pressure

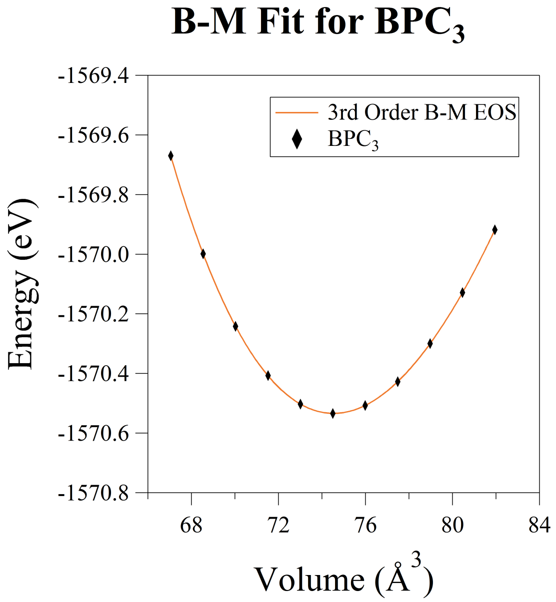

Figure A5: BPC$_3$ BM-EOS

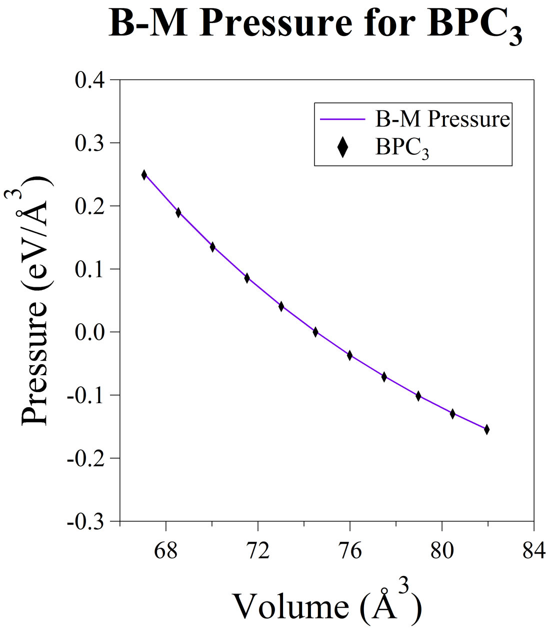

Figure A6: BPC$_3$ BM-Pressure

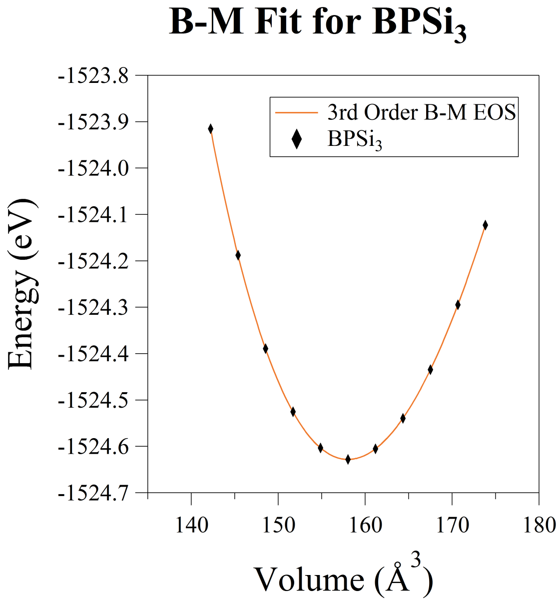

Figure A7: $BPSi_3$ BM-EOS

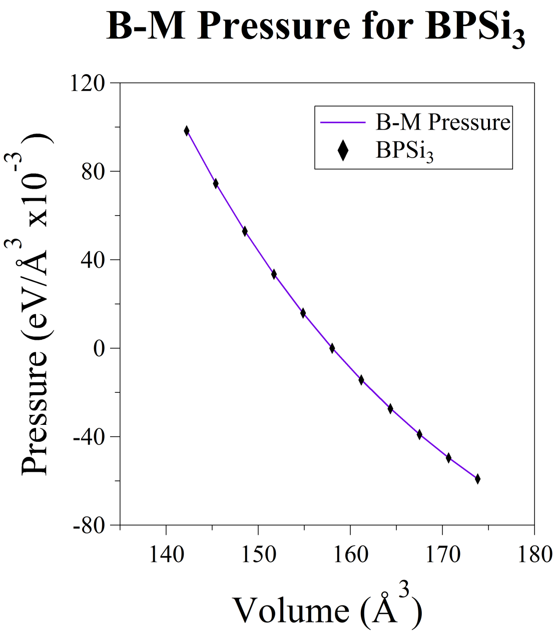

Figure A8: $BPSi_3$ BM-Pressure

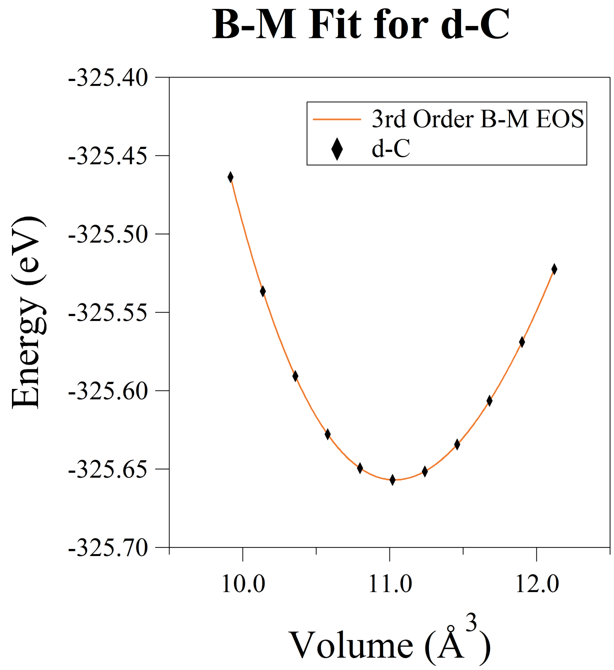

Figure A9: Diamond BM-EOS

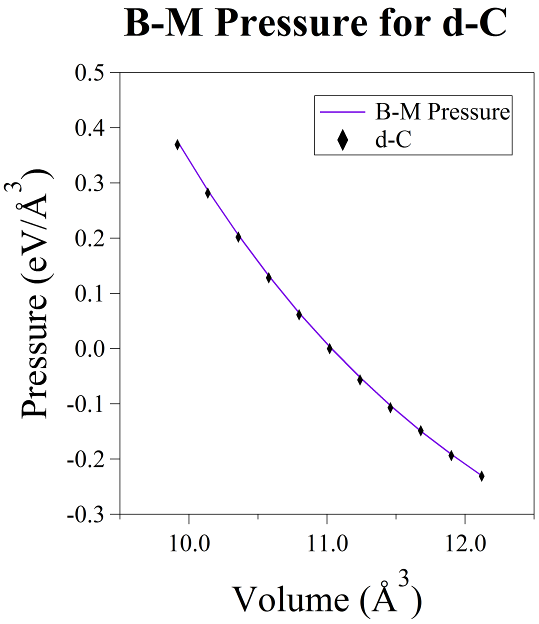

Figure A10: Diamond BM-Pressure

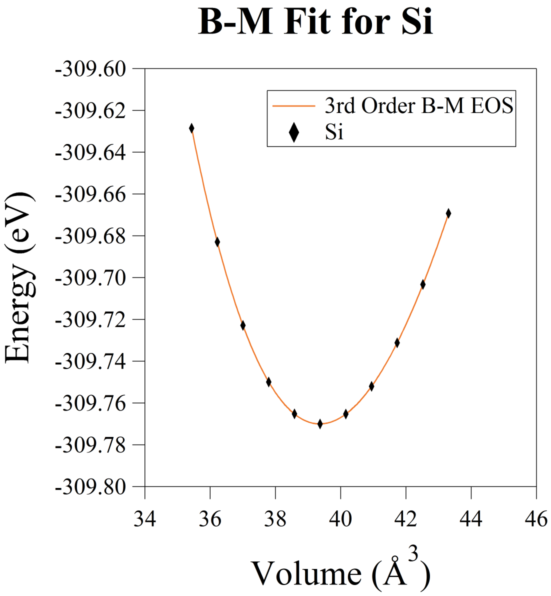

Figure A11: Si BM-EOS

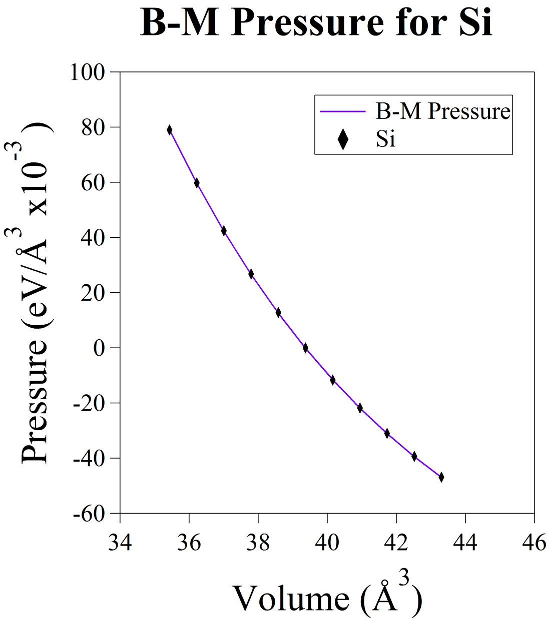

Figure A12: Si BM-Pressure

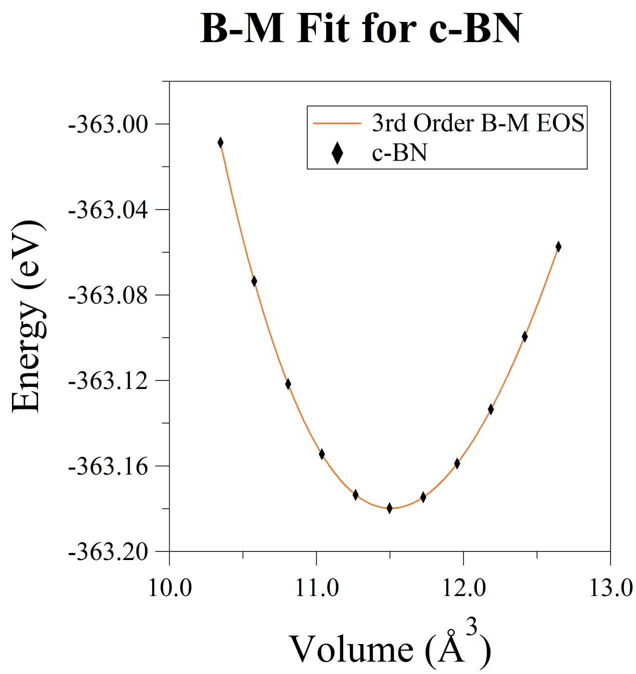

Figure A13: c-BN BM-EOS

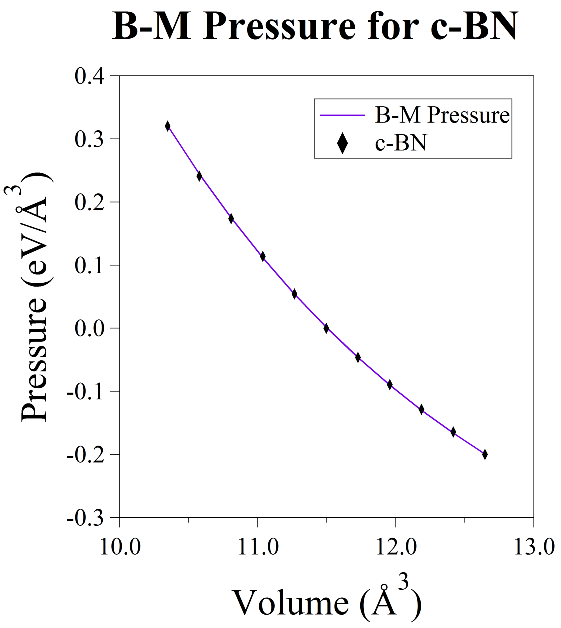

Figure A14: c-BN BM-Pressure

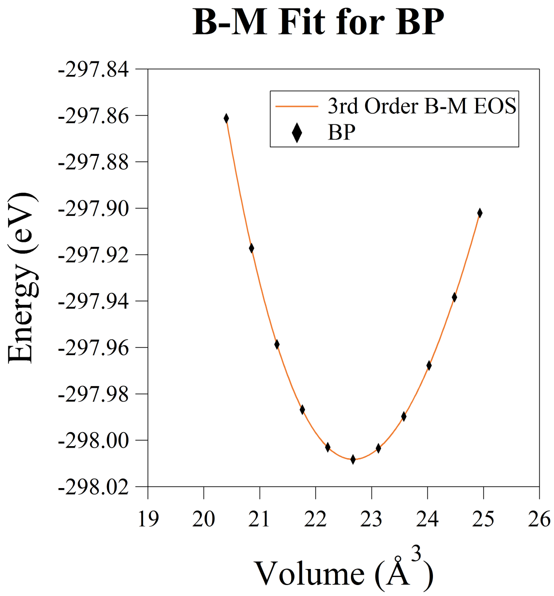

Figure A15: BP BM-EOS

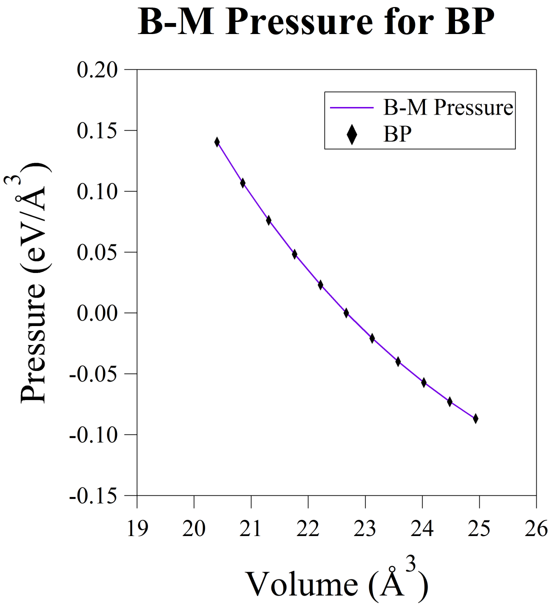

Figure A16: BP BM-Pressure

APPENDIX B

PERMISSIONS FOR REPRINTED MATERIALS

Copyright Clearance Center RightsLink®

Home | Account Info | Help | Chat

ACS Publications
Most Trusted. Most Cited. Most Read.

Title:	Rational Design of Monocrystalline (InP)yGe5−2y/Ge/Si(100) Semiconductors: Synthesis and Optical Properties
Author:	Patrick E. Sims, Andrew V.G. Chizmeshya, Liying Jiang, et al
Publication:	Journal of the American Chemical Society
Publisher:	American Chemical Society
Date:	Aug 1, 2013

Logged in as:
Patrick Sims
Account #:
3001119955

LOGOUT

PERMISSION/LICENSE IS GRANTED FOR YOUR ORDER AT NO CHARGE

This type of permission/license, instead of the standard Terms & Conditions, is sent to you because no fee is being charged for your order. Please note the following:

- Permission is granted for your request in both print and electronic formats, and translations.
- If figures and/or tables were requested, they may be adapted or used in part.
- Please print this page for your records and send a copy of it to your publisher/graduate school.
- Appropriate credit for the requested material should be given as follows: "Reprinted (adapted) with permission from (COMPLETE REFERENCE CITATION). Copyright (YEAR) American Chemical Society." Insert appropriate information in place of the capitalized words.
- One-time permission is granted only for the use specified in your request. No additional uses are granted (such as derivative works or other editions). For any other uses, please submit a new request.

BACK | CLOSE WINDOW

Copyright Clearance Center RightsLink®

Home Account Info Help

ACS Publications
Most Trusted. Most Cited. Most Read.

Title:	Crystalline (Al1−xBx)PSi3 and (Al1−xBx)AsSi3 Tetrahedral Phases via Reactions of Al(BH4)3 and M(SiH3)3 (M = P, As)
Author:	Patrick Sims, Toshihiro Aoki, Ruben Favaro, et al
Publication:	Chemistry of Materials
Publisher:	American Chemical Society
Date:	Apr 1, 2015

Logged in as:
Patrick Sims
Account #:
3001119955

LOGOUT

PERMISSION/LICENSE IS GRANTED FOR YOUR ORDER AT NO CHARGE

This type of permission/license, instead of the standard Terms & Conditions, is sent to you because no fee is being charged for your order. Please note the following:

- Permission is granted for your request in both print and electronic formats, and translations.
- If figures and/or tables were requested, they may be adapted or used in part.
- Please print this page for your records and send a copy of it to your publisher/graduate school.
- Appropriate credit for the requested material should be given as follows: "Reprinted (adapted) with permission from (COMPLETE REFERENCE CITATION). Copyright (YEAR) American Chemical Society." Insert appropriate information in place of the capitalized words.
- One-time permission is granted only for the use specified in your request. No additional uses are granted (such as derivative works or other editions). For any other uses, please submit a new request.

BACK CLOSE WINDOW

Copyright Clearance Center RightsLink®

Home Account Info Help

CAMBRIDGE JOURNALS

Title:	Atomic Scale Structure and Bonding Configurations in Monocrystalline Ah-xBxPSb Alloys Grown Lattice Matched on Si(001) Platforms
Author:	P. Sims, T. Aoki, J. Menendez, J. Kouvetakis
Publication:	Microscopy and Microanalysis
Publisher:	Cambridge University Press
Date:	Sep 23, 2015

Logged in as:
Patrick Sims
Account #:
3001119955
LOGOUT

Order Completed

Thank you for your order.

This Agreement between Patrick E Sims ("You") and Cambridge University Press ("Cambridge University Press") consists of your license details and the terms and conditions provided by Cambridge University Press and Copyright Clearance Center.

Your confirmation email will contain your order number for future reference.

Printable details.

License Number	4077901441196
License date	Mar 28, 2017
Licensed Content Publisher	Cambridge University Press
Licensed Content Publication	Microscopy and Microanalysis
Licensed Content Title	Atomic Scale Structure and Bonding Configurations in Monocrystalline Ah-xBxPSb Alloys Grown Lattice Matched on Si(001) Platforms
Licensed Content Author	P. Sims, T. Aoki, J. Menendez, J. Kouvetakis
Licensed Content Date	Sep 23, 2015
Licensed Content Volume	21
Licensed Content Issue	S3
Start page	1923
End page	1924
Type of Use	Dissertation/Thesis
Requestor type	Author
Portion	Full article
Author of this Cambridge University Press article	Yes
Author / editor of the new work	Yes
Order reference number	
Territory for reuse	World
Title of your thesis / dissertation	Synthesis of Hybrid (III-V)y(IV)5-2y Semiconductors: A New Approach to Extending the Optoelectronic Capabilities of Si and Ge Technologies
Expected completion date	May 2017
Estimated size(pages)	200
Requestor Location	Patrick E Sims School of Molecular Sciences Box 871604 Arizona State University

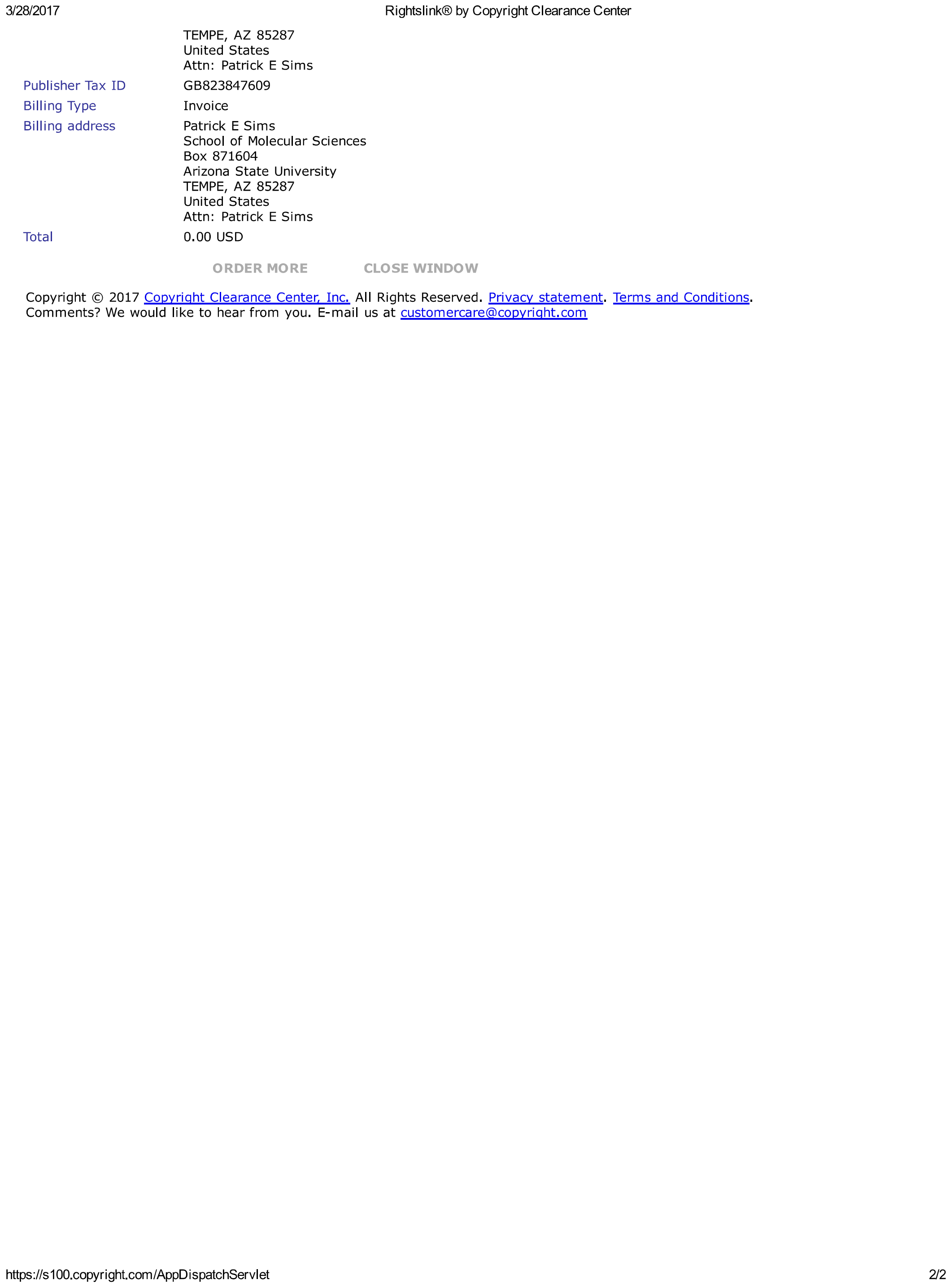

	TEMPE, AZ 85287 United States Attn: Patrick E Sims
Publisher Tax ID	GB823847609
Billing Type	Invoice
Billing address	Patrick E Sims School of Molecular Sciences Box 871604 Arizona State University TEMPE, AZ 85287 United States Attn: Patrick E Sims
Total	0.00 USD

Copyright Clearance Center RightsLink®

Home Account Info Help

ACS Publications
Most Trusted. Most Cited. Most Read.

Title:	Synthesis and characterization of monocrystalline GaPSi3 and (GaP)y(Si)5-2y phases with diamond-like structures via epitaxy driven reactions of molecular hydrides
Author:	Patrick E Sims, Chi Xu, Christian D. Poweleit, et al
Publication:	Chemistry of Materials
Publisher:	American Chemical Society
Date:	Mar 1, 2017

Logged in as:
Patrick Sims
Account #:
3001119955

LOGOUT

PERMISSION/LICENSE IS GRANTED FOR YOUR ORDER AT NO CHARGE

This type of permission/license, instead of the standard Terms & Conditions, is sent to you because no fee is being charged for your order. Please note the following:

- Permission is granted for your request in both print and electronic formats, and translations.
- If figures and/or tables were requested, they may be adapted or used in part.
- Please print this page for your records and send a copy of it to your publisher/graduate school.
- Appropriate credit for the requested material should be given as follows: "Reprinted (adapted) with permission from (COMPLETE REFERENCE CITATION). Copyright (YEAR) American Chemical Society." Insert appropriate information in place of the capitalized words.
- One-time permission is granted only for the use specified in your request. No additional uses are granted (such as derivative works or other editions). For any other uses, please submit a new request.

BACK CLOSE WINDOW